Christoph Franzen

Aeronomy of Hydroxyl Airglow Variability by Means of High-Resolution Telescope Observations and Gravity Wave Simulations

(Image copyright: The Nordic Optical Telescope; Photograph by Jens Jessen-Hansen)

Thesis for the degree of Philosophiae Doctor

Trondheim, March 2019

Norwegian University of Science and Technology
Faculty of Natural Sciences
Department of Physics

Abstract

Measurements of the OH airglow have been used as a way to remotely sense temperatures and chemical species in the Mesosphere and Lower Thermosphere (MLT) region. At the same time, the OH contaminates standard astronomical observations. It is considered a background in astronomical data, which has to be removed. This thesis, however, takes data from the Nordic Optical Telescope and extracts the spectrum of the OH airglow, masking out the astronomical target. With such spectra from an unusually high-quality instrument, the OH airglow can be measured on very different spatial scales, from the tens of kilometres scale down to the quantum scale.

On the kilometre scale, this thesis investigates the influence of large gravity waves and atmospheric tides in the MLT region on the apparent population of the rotational levels of the OH. Due to the approximately 7 km thickness of the OH layer, these waves perturb the OH differently at different altitudes. A ground-based observer who sees the integrated spectrum of the whole layer will then observe apparent excess populations at high rotational levels. The distribution of the apparent excess population looks very similar to excess populations due to non-local thermodynamic equilibrium (NLTE) effects, even though the simulations this thesis presents only include calculations under LTE conditions.

The same long-scale waves grow in amplitude as they ascend higher into the atmosphere in order to conserve their energy. When their amplitude grows too large to be supported by the surrounding atmosphere, they break into smaller and smaller waves and quasi-periodic structures (QPS) on metre scales. This thesis employed the telescope's high spatial resolution to detect horizontal QPS from 60 metres down to 4.5 metres. On these scales, the QPS still followed a Kolmogorov type cascade and did not break into the dissipative region. This behaviour is different from that previously observed for vertical turbulent structures in the MLT, which broke into the dissipative region at wavelengths between 10 and 40 metres.

On quantum scales, this thesis reports new measurements of the relative Q-branch transition probabilities for spontaneous emission (also called Einstein coefficients)

between vibrational and rotational levels. These measurements include seven Meinel rotational-vibrational bands with a change in the vibrational quantum number $\Delta v = 2$ or 3. These seven Meinel bands lie within the bandpass of commonly used telescope filters. Many of these measured Einstein coefficients for the Q-branch are lower than previously calculated, consistent with an uncoupling of the electronic angular momentum from the inter-nuclear axis (Pendleton et al., 2002).

Samandrag

Målingar av natthimmellyset frå OH er ein ofte bruka metode for å fjernanalysere temperaturen og den kjemiske komposisjonen i atmosfæreregionen kring Mesosfæren og den Lågare Termosfæren (MLT). Samstundes er strålinga frå OH-laget ei forureining av vanlege astronomiske observasjonar. Ho er vanlegvis ein del av bakgrunnen i astronomiske målingar og blir fjerna. Denne avhandlinga brukar data frå det Nordiske Optiske Teleskopet (NOT) og ekstraherer spektrumet av OH natthimmellyset, ved å trekkje frå det astronomiske objektet, som vanlegvis er fokuset i observasjonen. Dette er eit instrument av uvanleg høg kvalitet, og med eit spektrum frå dette instrumentet kan OH natthimmellyset verte måla på svært forskjellige romlege skalaar. Desse skalaane strekkjer seg ifrå nokre titals kilometer og heilt ned til kvanteskalaen.

På kilometerskalaen greier denne avhandlinga ut om korleis lange tyngdebølgjer og atmosfærisk tidvatn i MLT regionen påverkar ein tilsynelatande populasjon i rotasjonstilstandar til OH-laget. Fordi OH-laget er om lag sju kilometer tjukt kan desse bølgjene forstyrre OHet på ulike måtar på ulike høgder. Ein observatør på jordas overflate kan berre sjå ein sum av alle spektruma frå alle høgdene av OH-laget og vil difor måle ein tilsynelatande overpopulasjon av dei høge rotasjonstilstandane. Fordelinga av denne tilsynelatande overpopulasjon er veldig lik ein overpopulasjon som oppstår grunna fråvær av eit lokal termodynamisk likevekt (NLTE). Denne likskapen kan oppstå sjølv om alle simulasjonar som er presentert i denne avhandlinga føreset lokal termodynamisk likevekt (LTE).

Amplituden til dei lange tyngdebølgjene veks medan dei reiser oppover i atmosfæren, for å bevara energien til bølgja. Når amplituden blir for stor til at atmosfæren kan støtte bølgjene, kvitnar dei og dannar stadig mindre bølgjer og kvasiperiodiske strukturar (QPS), heilt ned til meterskalaen. Denne avhandlinga brukar den høge oppløysinga til teleskopet for å måle QPS med horisontale bølgjelengd mellom 60 og 4,5 meter. På denne skalaen følgjer bølgjene framleis ein type kolmogorovkaskade og går ikkje over i ein dissipativ region. Denne åtferda er ulik det som tidlegare er målt for vertikale turbulente strukturar i MLT regionen. Desse som gjekk over i ein dissipativ region når den vertikale bølgjelengda var mellom 10 og 40 meter.

På kvanteskalaen presenterer denne avhandlinga målingar av sannsynet for spontane overgangar (òg kalla einsteinkoeffisientar) mellom vibrasjons- og rotasjonsnivå i Q-greina. Desse målingane inneheld sju ulike meinelovergangar der forandringa i vibrasjonsnivået er $\Delta v' = 2$ eller 3. Desse sju meinelovergangane ligg innanfor dei mest bruka optiske filtera til teleskopet. Mange av dei målte einsteinkoeffisientane er mindre enn det som tidlegare er rapportert.

List of Papers

The papers below are the publications included in this thesis. The contribution of all co-authors is described afterwards.

Paper I

Franzen, C., Hibbins, R. E., Espy, P. J., & Djupvik, A. A. (2017). Optimizing hydroxyl airglow retrievals from long-slit astronomical spectroscopic observations. *Atmospheric Measurement Techniques, 10*(8), 3093-3101. doi:10.5194/amt-10-3093-2017

CF developed the data processing tools to extract OH airglow spectra from astronomical data, conducted the data interpretation and paper writing. REH and PJE provided the idea for the project and gave input to the data analysis and guidance in finalising the paper. AAD provided the data from the NOTCam, explained its format and helped with the astronomical data reduction tools.

Paper II

Franzen, C., Espy, P. J., Hibbins, R. E., & Djupvik, A. A. (2018). Observation of Quasiperiodic Structures in the Hydroxyl Airglow on Scales Below 100 m. *Journal of Geophysical Research: Atmospheres, 123*(19), 10,935-910,942. doi:10.1029/2018JD028732

CF was responsible for the data collection, data reduction and interpretation and the writing of the paper. PJE gave guidance for the reduction process, and PJE and REH helped to finalise the paper. AAD operated the NOT and helped plan the observation schedule.

Paper III

Franzen, C., Espy, P. J., & Hibbins, R. E. (2019). Modelled Effects of Temperature Gradients and Waves on the Hydroxyl Rotational Distribution in Ground-Based Airglow Measurements. *Submitted to Atmospheric Chemistry and Physics.*

CF modified the chemical model with dynamic inputs, ran the model and interpreted the model output. CF also wrote the paper. PJE supported the analysis process and paper writing. REH gave input on interpretation and paper writing.

Paper IV

Franzen, C., Espy, P. J., Hofmann, N., Hibbins, R. E., & Djupvik, A. A. (2019). Measurement of Q-branch transition probabilities for several hydroxyl Meinel bands. *To be submitted to the Journal of Quantitative Spectroscopy & Radiative Transfer.*

CF programmed the primary analysis tools, finalised the analysis code and conducted the verification of the results. CF also wrote the final paper. PJE gave guidance on the analysis and the written paper. REH also helped in writing the paper. NH extended the primary analysis tools for six out of the seven presented transitions.

Acknowledgements

Dear Patrick, thank you for your great supervision. Thank you for all the good ideas you had over the years, everything you taught me about the atmosphere and spectroscopy, and for correcting all of my English. Thank you for all the coffee break and stories as well. They made the work environment so friendly and enjoyable.

Dear Rob, thank you as well for all your helpful comments, both on science and on writing. Thank you for the at times long-distance supervision, and for answering my e-mails, regardless of the time of day, you received them.

Dear Amanda, thank you for giving me insight into the world of astronomers. Thank you for welcoming me so kindly during my visits to La Palma and for patiently answering all my questions about the telescope and the NOTCam. Thank you for making this whole thesis possible.

Dear Stefan, thank you for the time we worked together, and for all the strategy planning. Thank you for your scientific input; you were often helpful in providing a different point of view.

Dear Wim, thank you for being my office mate and thank you for all the pleasant conversations. Thank you for your enthusiasm for the research and for life in general.

Dear Sven, Niklas, Felix and Var, thank you for the time we worked together, even if it was short. I enjoyed your contribution to the social environment of the group and the new ideas and expertise you brought along with you.

Dear Halvor and Birk, thank you for sharing my enthusiasm for the research project in your Master theses. It was fun working with you and getting to see how your results developed.

Dear colleagues in the Department of Physics, both previous and contemporary, thank you for the friendly work environment, for the great coffee room, and for providing enough sugar to keep me going.

Dear members of the BCSS, thank you for making my research possible. Thank you for the discussions and the feedback during our meetings every semester.

Dear Anne and Pieter, thank you for keeping me sane with our coffee meetings and all the good stuff. Thanks for listening to my rants when necessary and thanks for making biotechnology sound so awesome.

Dear friends from Norway and in Aks, takk for at de har fylt helgene og kveldane mine med noko anna enn fysikk. Takk for song og leik, kos og glede, omsorg og gode minne. Takk for at de gjorde Trondheim til ein heim for meg.

Dear friends from Germany, thank you for the mutually assured distraction, the political updates and the awesome holidays we had.

Dear Frauke, thank you for believing in me from the beginning. Thank you for getting me started in my scientific career and all the support along the way.

My dear family; Danke, dass ihr mich immer unterstützt habt, auch wenn mich meine Wege in ferne Norwegen geführt haben. Dank euch konnte ich mich schon als Kind für die Naturwissenschaften begeistern. Ihr habt mir so den Weg zu dieser Arbeit eröffnet. Danke, dass ich in euch immer einen festen Punkt in meinem Leben habe, zu dem ich mich wenden kann, egal wo ich bin, oder wo ihr seid.

Kjæraste Anna, takk for at du gjer at eg smiler heile dagen. Takk for at du passar på meg.

Og takk til Deg, som alltid er med meg!

List of Abbreviations

AEP	Apparent Excess Population
HITRAN	HIgh-resolution TRANsmission molecular absorption database
LIDAR	LIght Detection And Ranging
LTE	Local Thermodynamic Equilibrium
MLT	Mesosphere and Lower Thermosphere
NIR	Near Infra Red
NLTE	Non Local Thermodynamic Equilibrium
NOT	Nordic Optical Telescope
NOTCam	Nordic Optical Telescope near-infrared camera and spectrograph
NRLMSISE-00	US Naval Research Laboratory Mass Spectrometer and Incoherent Scatter radar, from the ground through exosphere, the version from the year 2000
SABER	Sounding of the Atmosphere using Broadband Emission Radiometry (on TIMED)
TIMED	Thermosphere Ionosphere Mesosphere Energetics and Dynamics satellite
OH	Hydroxyl (chemical formula)
QPS	Quasi-Periodic Structure

Contents

1. Introduction

The atmosphere is often divided into four parts based on the temperature gradient; the troposphere, stratosphere, mesosphere, and thermosphere. Even though these four regions have different characteristics, they are not independent. The troposphere is mostly governed by convection. On the other hand, the Stratosphere and the Mesosphere and Lower Thermosphere (MLT) region are driven mostly by radiation, but the action of wave breaking can drive the dynamic atmosphere out of radiative equilibrium (Holton, 1983). These waves originate mostly in the troposphere and travel upwards. As they travel into regions with lower pressure, they increase in amplitude to conserve energy (Lindzen, 1981; Holton, 1982). Once their amplitude grows too large to be sustained, the waves start to break and dissipate their energy and deposit their momentum into the surrounding atmosphere. The waves, therefore, connect very distant layers of the atmosphere. Figure 1 shows a simplified diagram of the atmosphere. The temperature profile (black), decreasing in the troposphere due to surface heating, increases in the stratosphere due to ozone heating, decreases again in the mesosphere due to CO_2 cooling and finally increases in the thermosphere due to atmospheric absorption of short wavelength radiation.

One method often used to sense the state of the MLT region remotely is hydroxyl (OH) spectroscopy. Many studies have used the bright airglow in the near infrared that is emitted from the OH^* radical to infer rotational temperatures, densities, winds, and wave activity. Meinel was one of the first to see the potential of this minor species (Meinel, 1950a, 1950b). Even today, almost 70 years after these first publications, it is frequently used in day-to-day research.

Even though measurements of the OH airglow have been used extensively, there are still open questions to be answered on very different scales. These open questions start on quantum scales. For example, French et al. (2000) reported discrepancies between the rotational line intensity ratios of the Meinel (6,2) vibrational band, which Pendleton et al. (2002) explained with an angular momentum uncoupling effect on quantum scales. This thesis presents work extending this to seven other Meinel vibrational transitions in order to understand the extent of this uncoupling with vibrational level.

On the size scales of several metres, open questions remain on the nature of wave breaking in the MLT region. As mentioned above, wave breaking determines the dynamic state of this

region. Previous measurements of waves, quasi-periodic structures (QPS) and turbulent features only went down to scales of 550 m (Sedlak et al., 2016). This thesis presents measurements of QPS down to the size of 4.5 m, showing that the horizontal structures behave in a Kolmogorov type cascade even down to these scales.

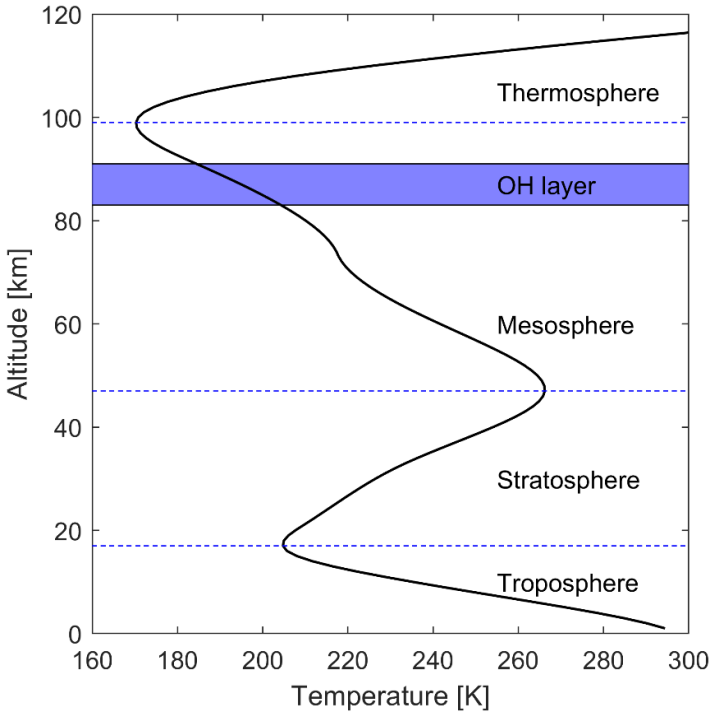

Figure 1: Schematic of the atmosphere: The black line shows a typical temperature profile for summer in the subtropics. Data from the NRLMSISE-00 model (Picone et al., 2002). The OH layer is shown in blue.

The larger scales also pose open questions. Gravity and tidal waves have an impact on the mean state of the OH airglow spectrum. This thesis includes numerical simulations of such large scale waves perturbing the OH layer and shows how they can affect temperature measurements and the apparent populations of different quantum levels.

2. Hydroxyl

The main observational focus of this thesis lies in the hydroxyl molecule, which is formed in the MLT region. This chapter will provide an in-depth explanation of its formation and behaviour in the excited states.

2.1 Chemistry

OH^* production

Under normal conditions, the atmosphere is well mixed below an altitude around 100 km (Andrews, 2010). This well-mixed state means that all the major species in the atmosphere remain at constant mixing ratios at any altitude. As the pressure decreases with altitude, the species density decreases as well. As an example, the density of O_2 from the Sounding of the Atmosphere using Broadband Emission Radiometry (SABER) instrument on the Thermosphere Ionosphere Mesosphere Energetics and Dynamics (TIMED) satellite (Mlynczak, 1997; Russell et al., 1999) is plotted in Figure 2 a) as a solid blue line. The measurements are a monthly mean and zonal average for December 2016 for mid-latitudes but can serve as an example for any time. The density of the O_2 decreases approximately exponentially. Solar UV radiation with a wavelength below 240 nm can photodissociate the O_2 bond and create atomic oxygen O (Andrews, 2010), and most of the O produced this way is found in the middle and upper atmosphere. Below the stratosphere, all the UV radiation with a wavelength below 240 nm has been absorbed, and no more atomic oxygen is produced this way. Figure 2 a) also shows the O density from TIMED/SABER. The O density is highest in the upper atmosphere and decreases rapidly below 90 km altitude.

These two species can react in the following way:

$$O + O_2 + M \rightarrow O_3 + M. \quad (1)$$

Here, M can be any mediator that carries away excess energy. In the well-mixed part of the MLT, the major species N_2, O_2 and O are the most likely species to mediate this reaction. The resulting density of ozone, O_3, from the SABER/TIMED observations is also shown in Figure 2 a) as a black dashed line. It shows a maximum in the MLT as O increases, a minimum where the O density decreases rapidly, and then an increase again as O_2 density becomes large at lower altitudes.

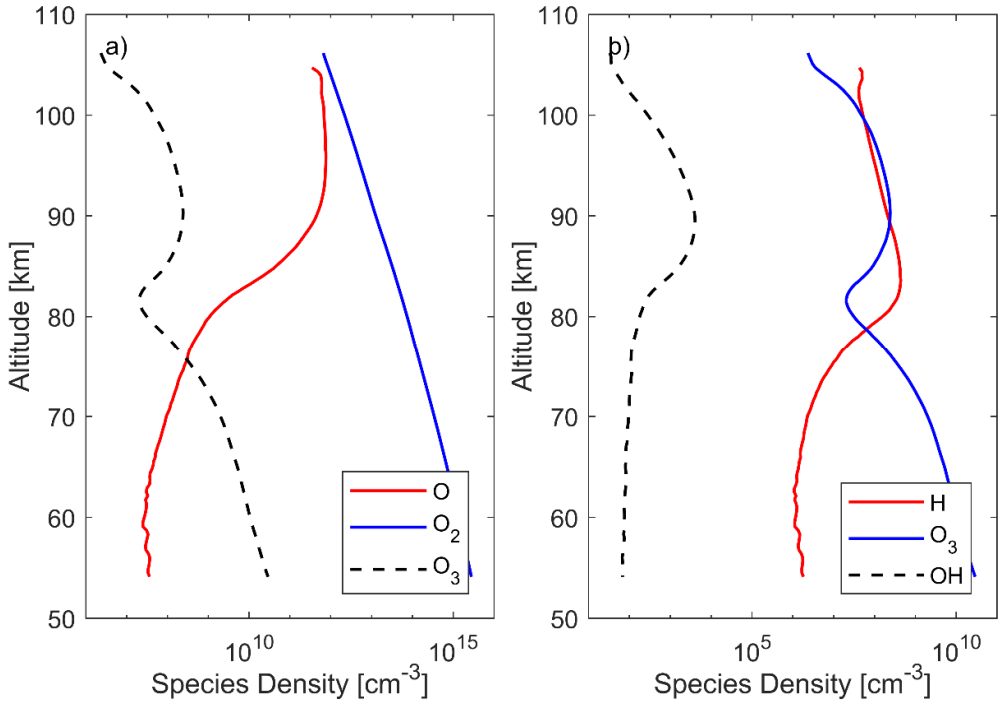

Figure 2: a) Species densities of the O (red), O_2 (blue) and the O_3 (black dashed). b) Species densities of H (red), O_3 (blue), and OH (black dashed), where the OH is created according to Equation (2) in the MLT region. All densities are measurements from TIMED/SABER and are a monthly mean and zonal average of December 2016 for mid-latitudes.

Another free atomic species in the MLT region is hydrogen. It is primarily formed via photodissociation of water vapour in the MLT region (Mlynczak et al., 2014). Therefore, its distribution is similar to the atomic oxygen in this region, decreasing rapidly below 80 km. The species density of H from TIMED/SABER is shown in Figure 2 b) in red. The atomic H can react with the O_3 via Equation (1):

$$O_3 + H \rightarrow OH(v') + O_2. \quad (2)$$

Figure 2 b) also shows the ozone species density (here in blue). The low density of the atomic hydrogen at lower altitudes makes the OH production very inefficient at these altitudes. The OH density (here in black and dashed) generally has only one maximum around 90 km altitude. This maximum has a half width of 7 ± 3 km and is usually centred around an altitude of 87 ± 3 km (Baker et al., 1988).

Equation (2) is highly exothermic by about 3.3 eV. The OH(v') created via the reaction in Equation (2) is therefore rotationally and vibrationally excited into vibrational levels with the quantum number, v', between 5 and 9. The branching ratio into the different vibrational levels has been measured by Charters et al. (1971), Ohoyama et al. (1985) and Klenerman et al. (1987). Adler-Golden (1997) extrapolated the branching ratios of Charters et al. (1971) to lower v', and these are shown in Table 1. Other measurements show a slightly different distribution. For comparison, Klenerman et al. (1987) reported the distribution for only $v' = 9$ to $v' = 6$ with the percentages shown in Table 1.

Table 1: Distribution of the OH(v') from Equation (2) into the different vibrational levels according to Charters et al. (1971) & Adler-Golden (1997) and according to Klenerman et al. (1987).

Vibrational level	Charters et al. (1971), Adler-Golden (1997)	Klenerman et al. (1987)
$v' = 9$	47 %	44 %
$v' = 8$	34 %	28 %
$v' = 7$	15 %	19 %
$v' = 6$	3 %	9 %
$v' = 5$	1 %	0 %

OH^* destruction and relaxation

The excited hydroxyl can relax through different mechanisms to reach lower vibrational levels v'', including the $v'' = 0$ level. One of these relaxation mechanisms is collisional quenching, where the OH collides with a mediator M and gives some or all of its vibrational energy to the mediator. The reaction for this is:

$$\mathrm{OH}(v') + \mathrm{M} \rightarrow \mathrm{OH}(v'') + \mathrm{M} \tag{3}$$

Here, M can here be any mediator dependent on their abundance in the MLT. The most common ones are therefore the major species N_2, O_2, CO_2 and O (Adler-Golden, 1997). This quenching can be single-quantum, where $\Delta v = v' - v'' = 1$, or multi-quantum, where $\Delta v > 1$. In the case of "sudden death" quenching, the final vibrational state is the ground state $v'' = 0$ (McDade et al., 1987). Adler-Golden (1997) showed in a simulation that the single-quantum

case is always the dominant one. However, for higher *v'*, multi-quantum quenching becomes important. OH(*v'*) can also be destroyed chemically via:

$$\mathrm{OH}(v') + \mathrm{O} \rightarrow \mathrm{H} + \mathrm{O}_2. \quad (4)$$

This reaction increases with vibrational level (Caridade et al., 2013) and is a constant sink of the OH(*v'*) population. Besides chemical destruction of the OH(*v'*), the OH(*v'*) can also change its vibrational excitation by spontaneous emission of radiation via:

$$\mathrm{OH}(v') \rightarrow \mathrm{OH}(v'') + h\nu. \quad (5)$$

Here, $h\nu$ is a photon with the wavenumber ν. Spontaneous vibrational-rotational relaxation via radiation can happen between any upper *v'* and lower *v''* level, but $\Delta v = 2$ is the dominant transition (Langhoff et al., 1986). Radiative relaxation via Equation (5) can lead to a cascade down the vibrational energy levels and produce OH(*v'*) in many different vibrational levels.

Taking Equations (1) to (5) together, a simple model can be generated to calculate the OH(*v'*) density over the different *v'*, assuming a steady state between production and loss. The background atmosphere of N_2, O_2, O and H densities; temperature; total number density and total mass density can be taken from an empirical model such as NRLMSISE-00 (Picone et al., 2002).

Figure 3, which shows the OH(*v'*) density for *v'* between 1 and 9, was produced with such a steady-state model used in paper 3 of this thesis (Franzen et al., 2019a). The different species density profiles are shown in different colours, with the *v'* = 1 case being the darkest shade of blue, and the *v'* = 9 case the darkest shade of red. All of the profiles have a similar shape, with the lower *v'* profiles maximizing at both lower altitudes and higher density. On average the altitude of the maximum of this profile changes by approximately 0.5 km per vibrational level (von Savigny et al., 2012). Therefore, the layer thickness is far larger than the separation between the different layers.

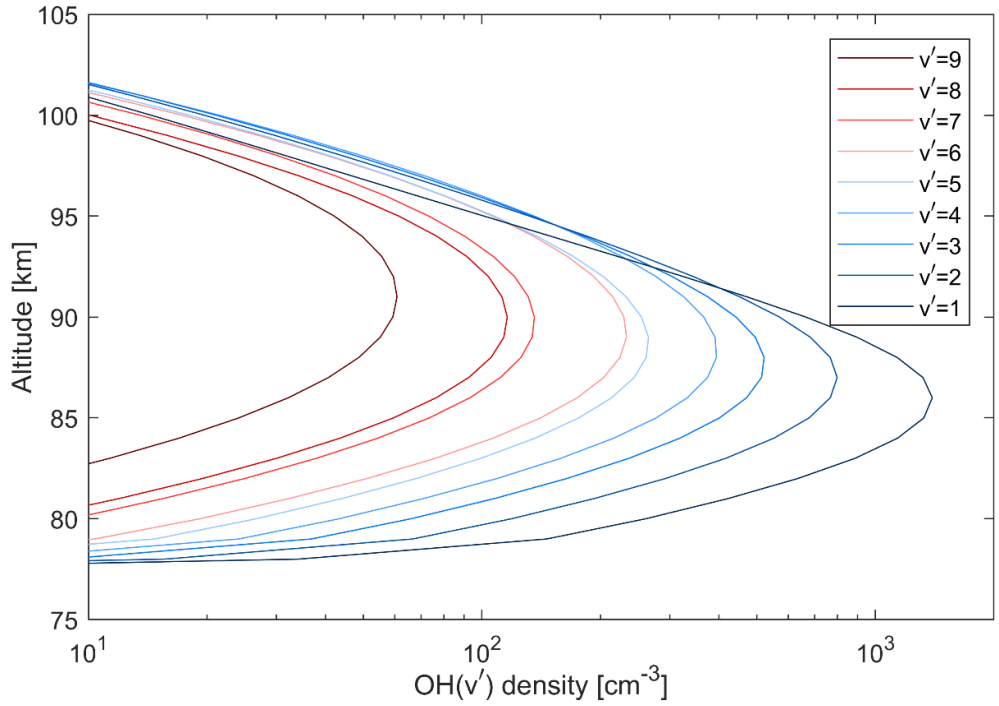

Figure 3: density distributions of the OH(*v'*) at different *v'*. The lowest vibrational level *v'* = 1 (darkest blue) has the highest density, and its maximum is at the lowest altitude. The highest vibrational level *v'* = 9 (darkest red) has the lowest density, and its maximum is at the highest altitude.

2.2 Quantum Mechanics

A detailed explanation of the quantum mechanics of diatomic molecules can, for example, be found in Herzberg (1950). The aspects relating to the OH molecule of relevance to this thesis are discussed in this section.

Energy levels

The separated O and H atoms, each in their ground states, are brought together and decrease their inter-nuclear distance to form the OH molecule. The energy of the OH molecule formed, called the *X* state, is less than that of the two separated atoms by the binding energy (the molecule is a lower energy configuration than the two separated atoms). This binding energy sets the depth of the well. The charged nuclei, sharing their valence electrons in an orbital, vibrate back and forth like a harmonic oscillator with inner and outer turning points. These vibrations are quantized, giving rise to the vibrational levels separated by approximately 0.35 eV. In addition to vibration, the nuclei undergo quantized rotations. Since the molecule

vibrates on the order of 1000 times for a single rotation, the energy separation of the lowest rotational levels is on the order of 5 meV (although this is non-linear and increases between states as n*2B, where B is the rotational constant, about 20 cm^{-1} = 2.5 meV). All transitions considered in this thesis are between different vibrational and rotational levels within the electronic ground state *X*.

Selection rules and transitions

Transitions from an upper quantum state *S'* to a lower quantum state *S''* are subject to selection rules. To a first approximation, the possibility of a transition between any state *S'* to state *S''* is given by the overlap integral between the wave functions of the two states.

The vibrational state can change from any upper state *v'* to any lower state *v''*. However, the near-infrared (NIR) measurements in this thesis cover only the transitions with a change in vibrational states of $\Delta v = 2$ and $\Delta v = 3$.

The selection rules for the rotational levels *J'* are stricter than the ones for the vibrational levels. In the cases observed in this thesis the rotational quantum number can only change by one unit, or not at all; that is, $\Delta J = J'' - J' = -1, 0, +1$. These three different cases give three different branches, separated in energy and therefore wavenumber and wavelength. Figure 4 a) shows an energy diagram as an example of the (9,7) transition. The vibrational energy gap is not to scale. Twelve different transitions between the energy levels are shown, with the cases $\Delta J = -1, 0, +1$ represented. Figure 4 b) below shows the resulting spectra of the transitions in Figure 4 a).

On the left, transitions with $\Delta J = -1$ are shown. Together, these transitions form the R-branch. Transitions from higher rotational upper states *J'* have slightly more energy than transitions from lower rotational upper states *J''* due to the quadratic nature of the rotational states. Transitions from higher R-branch levels, therefore, are more energetic and appear at shorter wavelengths. The case $\Delta J = 0$ is called the Q-branch. Since the rotational upper and lower states have the same quantum number, the Q-branch lines are close to each other. The last case $\Delta J = +1$ forms the P-branch. Since the energy gap between the upper and lower rotational levels for the P-branch is smaller than for the other branches, the P-branch lines lie at the longer wavelength end of the spectrum. The first line of the P-branch is close enough to the Q-branch that high Q-branch lines may lie close to, or even overlap with the low P-branch lines.

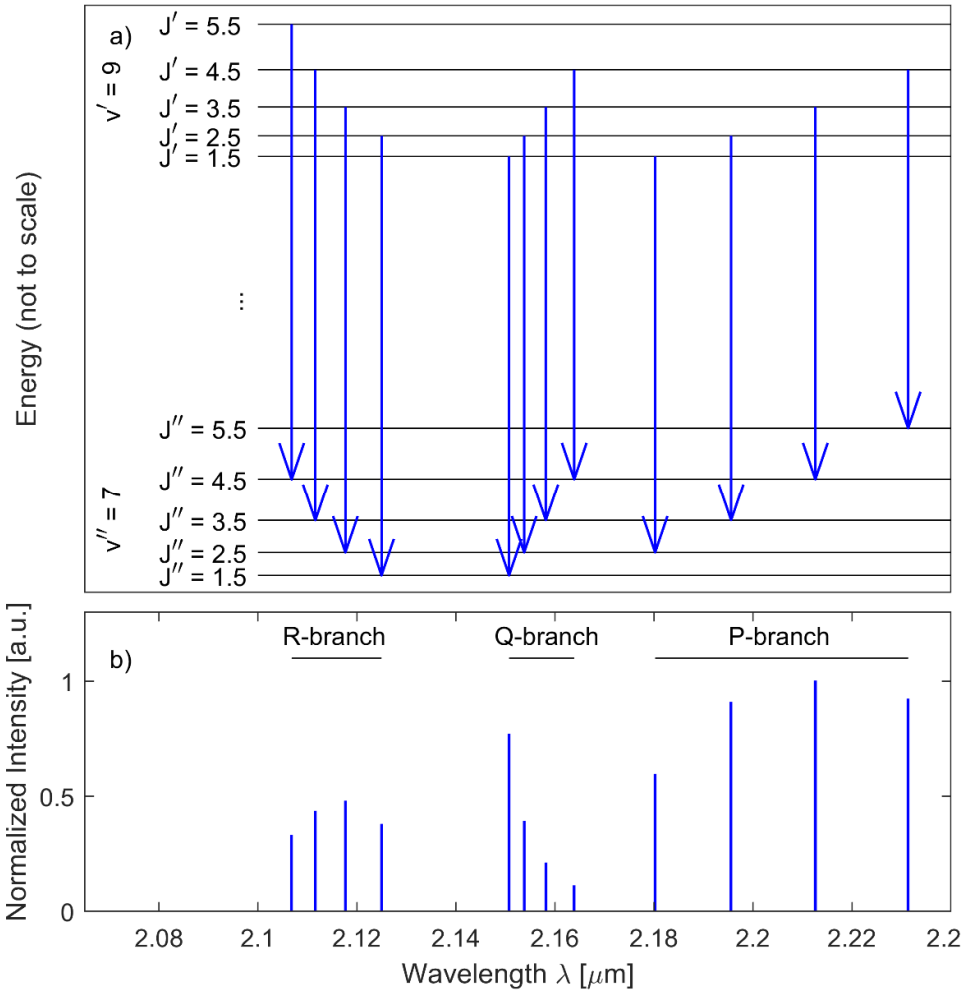

Figure 4: a) Simplified energy diagram of the OH molecule. The upper vibrational level $v' = 9$ and the lower level $v'' = 7$ are shown. For each vibrational level, the lowest five rotational levels are shown. Arrows indicate the five lowest possible transitions with $\Delta J = -1$ for the R-branch, $\Delta J = 0$ for the Q-branch and $\Delta J = +1$ for the P-branch. The energy axis is not to scale, and Λ-doubling and the $X^2\Pi_{1/2}$ substates are not shown. b) The resulting spectrum of the twelve transitions shown in a).

The example shown in Figure 4 of the (9,7) transition is typical for the Meinel vibrational-rotational transitions presented in this thesis. However, details such as the distances between the single branches can differ for different vibrational transitions. Paper 1 (Franzen et al., 2017) gives an overview of the eight observed Meinel transitions for this thesis.

OH doublet states, Λ-doubling and forbidden transitions

Figure 4 above shows twelve lines in the (9,7) Meinel transition, but other lines are possible. The HIgh-resolution TRANsmission molecular absorption database (HITRAN) (Rothman et al., 2013) lists a total of 434 lines for the (9,7) transition. While Figure 4 only shows lines up to $J' = 5.5$, the HITRAN database lists lines up to $J' = 18.5$. Even though all these lines can still be categorised as R-, Q- and P-branches as described above, there are some differences.

Figure 4 shows only those transitions that take place within one of the two different spin sublevels of the OH. While the orbital momentum is $L = 1$ (i.e. a Π-electronic-state), the spin of the unpaired electron is $\Sigma = \pm\frac{1}{2}$. The total angular momentum Ω can, therefore, be either $\frac{1}{2}$ or $\frac{3}{2}$. The spectrum shown in Figure 4 shows the state $X^2\Pi_{3/2}$, which is the electronic doublet ground state with a total angular momentum of $\frac{3}{2}$. The $X^2\Pi_{1/2}$ state, the other doublet state, has slightly higher energy. Figure 5 shows the complete spectrum of the (9,7) transition. The solid red lines are the lines from the $X^2\Pi_{3/2}$ state, while the blue dashed lines are from the $X^2\Pi_{1/2}$ state. Every line therefore appears twice in the spectrum, once for each doublet state.

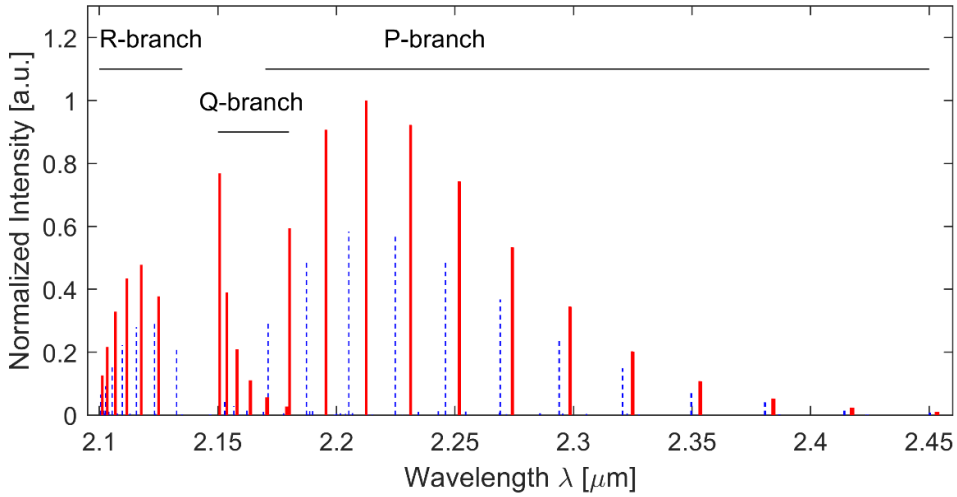

Figure 5: The full spectrum of the (9,7) Meinel transition with values from the HITRAN database. Lines from the $X^2\Pi_{1/2}$ doublet state are shown in blue dashed, lines from the $X^2\Pi_{3/2}$ doublet state are shown in red solid.

As the result of perturbations from the higher lying *A* electronic state, the normally energy-degenerate projections of the angular momentum Λ split slightly, resulting in each rotational line being a closely spaced doublet. However, the energy gap of this splitting is so small, that the two resulting lines are not visible in Figure 5, nor are they separable in any data analysed in this thesis. Henceforth, the Λ-splitting is treated as just a simple degeneracy at the exact same energy.

Lastly, there are also forbidden lines. Forbidden transitions cannot take place through emission or absorption of electric dipole radiation, and thus the transition probability from one state to another, discussed in the next section, is zero. However, transitions can take place though magnetic dipole, electric quadruple, or higher moment transitions. Although their intensity is much lower than the dipole-allowed transitions, these lines can be observed. Even though these lines are not directly discussed in the papers of this thesis, they are part of all the spectral fits, whenever the full spectrum is fitted, throughout this thesis.

Line intensities and transition probabilities

The spectra shown in Figures 4 and 5 show the lines of the (9,7) transition with different normalised intensities. These intensities can be calculated as:

$$I_{v',v'',J',J''} = N_{v',J'} \cdot A_{v',v'',J',J''}, \tag{6}$$

where *I* is the intensity of one line, *N* is the population of the upper vibrational and rotational state, and *A* is the transition probability between the upper state *S'* and the lower state *S''*.

The transition probability is also called the Einstein coefficient and describes how many transitions would happen per second per unit population. To calculate these Einstein coefficients, one has to know the dipole moment function between the upper and the lower states as a function of inter-nuclear distance. This function can be estimated over a limited range of inter-nuclear distance through measurements of relative band intensities. Since the OH molecule has a relatively large spacing of rotational energy levels, the extrapolation of the dipole moment function to zero from the measured region is very important for the precise determination of the Einstein coefficients. Different extrapolations of the dipole function toward zero have led to different sets of transition probabilities from, for example, Mies (1974), Turnbull et al. (1989), Langhoff et al. (1986), as well as the Pickett et al. (1998) transition probabilities that are tabulated in the HITRAN database (Rothman et al., 2013).

Einstein coefficients for Q-branch transitions have been measured relative to the P- and R-transitions from the same upper state, but different lower states, by French et al. (2000) for the (6,2) Meinel transition. Paper 4 of this thesis (Franzen et al., 2019b) extends this work for seven different Meinel vibrational transitions. Comparisons of these relative values with the values tabulated in HITRAN indicate that the Q-branch Einstein coefficients have been overestimated for all vibrational levels, although the extent of that overestimation depends upon the vibrational transition being measured. (Pendleton et al., 2002) could explain the difference observed by French et al. (2000) with the effect of electronic angular momentum uncoupling from the inter-nuclear axis for the (6,2) transition.

Figure 6 shows the Einstein coefficients of the (9,7) Meinel transition for the HITRAN database. The Einstein coefficients for the P-branch (black circles) are, after a small increase for the first rotational levels, rather constant around 70 to 80 s^{-1}. The Einstein coefficients for the R-branch (red crosses) show similar behaviour, but with a small peak at $J' = 4.5$. However, the Q-branch (blue stars) shows a rapid decrease of the Einstein coefficients with J'. This decrease is dominant in giving the Q-branch in Figure 5 its falling shape since the line intensity is the product of the level population and the Einstein coefficient (see Equation (6)).

The second variable in Equation (6) is the population of the upper state $N_{v',J'}$. If one assumes that OH is in thermodynamic equilibrium, the v' and J' components of the population can be separated into a general population of the upper vibrational state $N_{v'}$ and a thermal distribution of these into the closely spaced rotational states belonging to this vibrational state. If that thermal distribution is assumed to be collision dominated, then it can be described by a Maxwell-Boltzmann distribution as:

$$N_{v',J'} \propto N_{v'} \cdot g_{J'} \cdot \exp\left(-\frac{E_{J'}}{k_B T}\right), \tag{7}$$

where $g_{J'}$ is the degeneracy of the rotational level, $2(2J'+1)$ (including the Λ-splitting), and $E_{J'}$ is the energy of this upper state. Since both the degeneracy and the energy of the upper states increase quadratically with J', the population first increases with $g_{J'}$ at low energies before exponentially decreasing at higher energies. This results in a peak in the population distribution. Higher temperatures shift the peak of the population towards higher rotational levels and stretch the distribution, i.e. dividing the population into more levels. Cooler temperatures, on the other hand, shift the peak to lower J' and distribute the population over fewer levels.

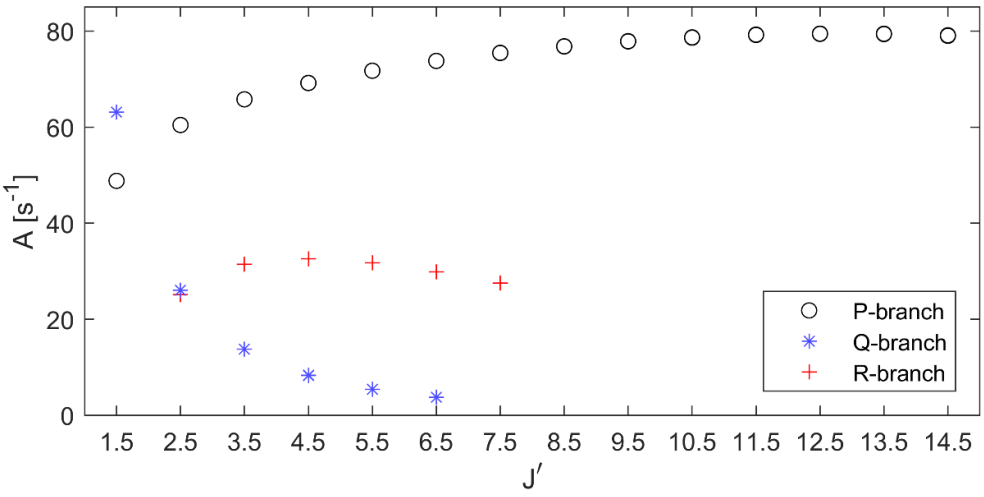

Figure 6: Einstein coefficients (A) of the (9,7) Meinel transition from the HITRAN database. The P-branch (black circles), Q-branch (blue stars) and the R-branch (red crosses) are shown. The Q-branch Einstein coefficients decrease fast with the rotational quantum number, while the Einstein coefficients for the other two branches stay comparatively more constant.

However, whether OH is actually in local thermodynamic equilibrium (LTE) is still an open debate. Many measurements show that at least the levels below N = 5, i.e. $J'<5.5$ are thermalized, and in LTE (Harrison et al., 1970; Harrison et al., 1971; Sivjee et al., 1972; Sivjee et al., 1987; Pendleton et al., 1993; Perminov et al., 2007). For these levels, the energy separation is less than the thermal kinetic energy of the atmosphere, kT. This small separation facilitates an efficient collisional energy transfer between levels, and thus thermalises them into a Boltzmann distribution (Maylotte et al., 1972; J. C. Polanyi et al., 1972; J. C. Polanyi et al., 1975). However, other observations indicate that all of the OH rotational levels are incompletely thermalised and in non-local thermodynamic equilibrium (NLTE) (Cosby et al., 2007; Noll et al., 2015).

To achieve absolute population, one has to divide Equation (7) by the partition function Q. This is the sum of the populations of all rotational levels and is sometimes called the state sum. It can be approximated as:

$$Q = \frac{k_B T}{hcB}. \tag{8}$$

Here, B is the rotational constant that is proportional to the width of the potential energy well, which is relatively broad for the OH molecule. B varies for the OH with vibrational level but is approximately 20 cm^{-1}. The total intensity of any OH line therefore becomes:

$$I_{v',v'',J',J''} = 2(2J' + 1) \cdot N_{v'} \cdot \frac{A_{v',v'',J',J''}}{Q} \exp\left(-\frac{E_{J'}}{k_B T}\right). \tag{9}$$

3. Hydroxyl Spectroscopy with the NOT

All the primary data that were analysed in this thesis were obtained using the Nordic Optical Telescope (NOT). The NOT is located at the Observatorio del Roque de los Muchachos, on La Palma, Canary Islands, Spain (17°53' W, 28°45' N). It is a collaboration between the five Nordic countries, Denmark, Finland, Iceland, Norway and Sweden. The map in Figure 7 shows the location of the NOT in La Palma and the five member states in blue. The location on La Palma was chosen, despite its geographic distance to the member states, because of the local astronomical conditions. The whole area of the observatory is a national park, which by law protects the astronomical conditions, such as the light pollution, radio-electronic pollution, atmospheric pollution, and air traffic above the area (Carlos et al., 1988). The position on the edge of the caldera at approximately 2400 metres above sea level yield good weather conditions throughout the year. The low latitude of 28°45' north gives only a small variation in the length of the night throughout the year.

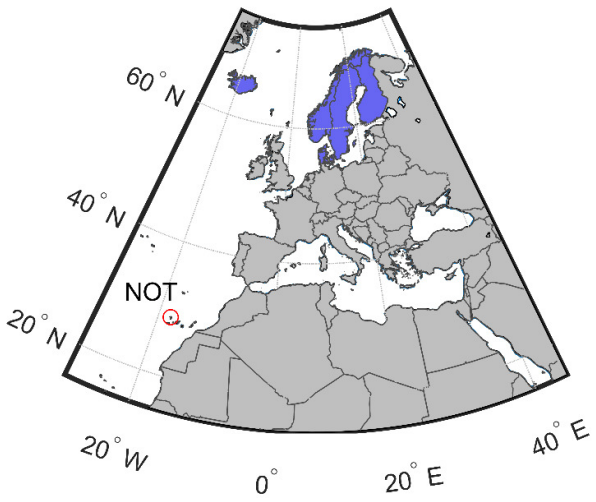

Figure 7: Map of Europe and North Africa. The NOT is marked on La Palma, Canary Islands. The member countries of the NOT (Denmark, Finland, Iceland, Norway and Sweden) are marked in blue.

Near-infrared (NIR) astronomical observations are contaminated by emission from the OH airglow. Standard astronomical procedures aim to remove as much of the OH airglow as possible from the target spectrum. To that end, the spectrum of the OH airglow from a starless part of the slit is often recorded and used to subtract the OH airglow "contamination" from the

target's spectrum. A side effect of this procedure is that for each spectrum measured towards an astronomical target, a spectrum of the OH airglow is measured and archived.

The main NIR spectroscopy instrument of the NOT is the Nordic Optical Telescope near-infrared camera and spectrograph (NOTCam) (Abbott et al., 2000). It has been used for spectroscopic measurements since August 2003. Typical "low-resolution" ($R = \lambda/\Delta\lambda \sim 2100$) observations utilise a 1024 x 1024 pixel detector and a slit length of 4 arcmin. The slit projects onto approximately 100 metres on the night sky at OH layer altitudes. Simultaneously the width of the slit is only 0.6 arcseconds, which projects to less than 25 cm on the airglow layer. The OH airglow observations with this telescope provide much higher spatial resolution than standard OH remote sensing instruments. The drawback of using data from a telescope is the restricted availability for experiments directed towards atmospheric research. Paper 2 in this thesis (Franzen et al., 2018) had access to measurements taken with the NOT specifically for atmospheric research. Paper 1 (Franzen et al., 2017) and Paper 4 (Franzen et al., 2019 b) worked with data from the NOTCam astronomical archive instead.

The majority of the standard NOTCam spectroscopic observations utilize one of three filters: J, H or K. Each filter is centred on a minimum in the water vapour absorption (atmospheric windows) and spans different OH airglow Meinel transitions. Additionally, the NOTCam can be used with the K' filter, which is similar to the K filter, but with the wavelength range shifted slightly towards the blue. Table 2 gives an overview of the transitions that lie in each filter and the branches that are visible. The (8,6) transition is heavily absorbed by H_2O in the atmosphere and was therefore only used in paper 1 (Franzen et al., 2017) and not in the subsequent papers. Additionally, Figure 8 shows the filters (black, right axis) and the eight Meinel vibrational transitions (alternating red and blue for distinction, referenced to the left axis) on a wavelength scale. The areas between the filters feature strong atmospheric absorptions and are therefore not normally used for observations, either for the MLT region or for astronomical targets.

The papers presented in this thesis make use of the high signal to noise and very high spatial resolution spectroscopic data afforded by this instrument. Paper 1 (Franzen et al., 2017) shows how to extract the OH airglow spectrum from a standard astronomical observation. The paper discusses in detail how the data from the astronomical observation can be reduced to yield a clean OH spectrum. These high signal-to-noise ratio spectra facilitate new research on the OH and the MLT layer on very different scales. Paper 1 (Franzen et al., 2017) discussed how the high spatial and temporal resolution OH spectra can be used to measure waves and quasi-

periodic structures (QPS) in the MLT layer down to the metre scales. This research is published in Paper 2 (Franzen et al., 2018).

Table 2: Overview of the eight observable Meinel transitions in the OH airglow in the four standard NOTCam filters J, H, K and K'. The (8,6) transition is heavily influenced by atmospheric absorption and was only used in Franzen et al. (2017).

Transition	Filter	Visible branches	Comments
(3,1)	H	Q, P	R-branch outside of filter range
(4,2)	H	R, Q, P	
(5,3)	H	R, Q, P	
(6,4)	H	R, Q	P-branch outside of filter range
(7,4)	J	R, Q, P	Low intensity due to $\Delta v = 3$
(8,5)	J	R, Q, P	Low intensity due to $\Delta v = 3$
(8,6)	K	P	Heavy H_2O absorption, R- and Q-branch outside of filter range
(8,6)	K'	R, Q, P	Heavy H_2O absorption
(9,7)	K, K'	R, Q, P	

Furthermore, paper 1 (Franzen et al., 2017) was able to show a snap-shot measurement of the temperature gradient in the MLT. This temperature gradient can be heavily influenced by large, kilometre-scale, waves and tides in the atmosphere. Paper 3 (Franzen et al., 2019a) describes and models this large scale wave interaction with the observed OH airglow in detail and discusses how wave perturbations can generate an apparent excess population of the higher rotational lines, even under pure LTE conditions. Lastly, the availability of the high-quality data in the archive described in Table 2 allows a precise measurement of the Q-branch Einstein coefficients, which influence the OH airglow even on quantum scales. This research is presented in paper 4 (Franzen et al., 2019b). These papers are introduced in the next section.

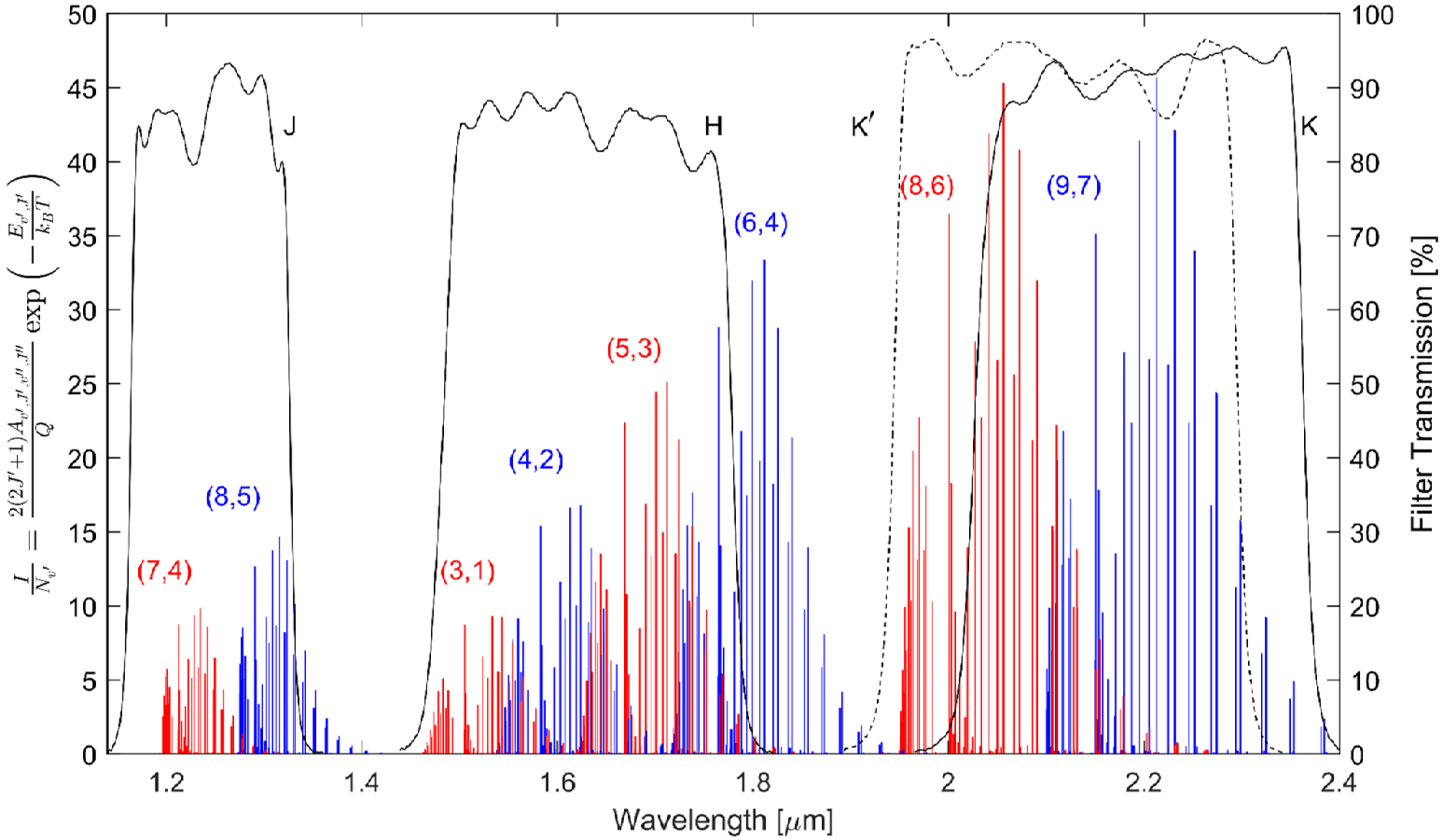

Figure 8: Overview of the four NOTCam filters, J, H, K', and K (black, right axis). Synthetic spectra of the eight observable Meinel transitions at a rotational temperature of 200 K are shown alternating in red and blue (left axis).

4. OH Spectroscopy on Different Scales

4.1 Paper 1

To unlock the potential of the data in the astronomical archive of the NOTCam for atmospheric use, the OH spectrum had to be extracted. However, standard astronomical procedures are optimised to remove the airglow spectrum and extract the (usually much brighter) spectrum of the astronomical target. Figure 9 (a) shows typical astronomical data as it comes from the archive. The vertical axis is the spectral direction, while the horizontal axis is the spatial direction. The bright vertical line a little to the left of the centre is the spectrum of a star. Large step-like background effects can be seen in the spectral direction. Both these background effects and the star are much brighter than the OH lines, which can be seen as slightly upward curving lines in the background. The positions of the Q(1) lines of the four visible transitions are marked on the side to help guide the eye.

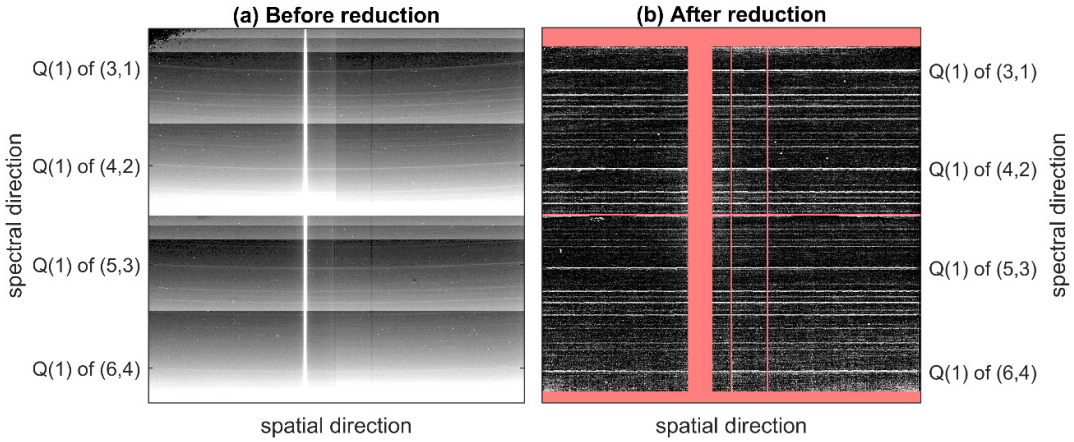

Figure 9: Image of the OH spectrum in the H band on the detector. The positions of the Q(1) lines of the four visible transitions are marked on the side. The y-axis is the spectral direction; the x-axis is the spatial direction along the slit. (a) (left) Before the data reduction. The bright vertical line a little left of the centre is a spectrum of a star. Steep background effects dominate the rest of the picture. (b) (right) After the data reduction. The OH spectral lines are now visible without background structure. Not used parts of the detector (e.g. the position of the star spectrum) are marked in red. Figure reproduced from (Franzen et al., 2017).

Dead pixels (i.e. pixels with no response) and hot pixels (i.e. pixels with too strong and unreliable response) were masked out first. The dark current was removed by subtracting dark images taken with a shut shutter. Wavelength-dependent variations (e.g. from the optical filter) were corrected by using the spectrum of the light of a halogen lamp with a 3,200 K colour temperature. The spectrum of the star was removed, together with the surrounding pixels the star bleeds into. In total, a 60-pixel wide column was removed. Cosmic ray hits were masked out at the same time. These can create very intense, but isolated hits, usually only affecting a single pixel. They could therefore be detected easily as pixels that are much brighter than their neighbours. After that, the curvature of the OH lines due to the telescope optics was corrected. All these steps produce the detector image shown in Figure 9 (b), where masked out pixels are shown in red. The only features left in the data after these image reduction steps are the OH airglow lines, now clearly visible as straight horizontal lines.

The spectrum of the OH airglow was then retrieved by summing all the pixels in the horizontal direction. Lastly, the wavelength calibration was performed using the spectral positions of the OH lines themselves listed in the HITRAN database. For this wavelength calibration, only the brightest lines of the Q- and P-branches visible in a given filter, were used.

All these steps transformed a standard astronomical observation from the NOTCam archive to a clean and high signal-to-noise spectrum of the OH airglow. The details of each step are described in paper 1 of this thesis (Franzen et al., 2017) together with the quality assurance of the process. This data reduction tool opened up the research on the OH airglow with astronomical data from the NOTCam archive. It thereby directly enabled the work presented in paper 2 (Franzen et al., 2018) and paper 4 (Franzen et al., 2019b) of this thesis.

4.2 Paper 2

The smallest horizontal scale OH wave observations before the publication of paper 2 (Franzen et al., 2018) was a wave structure of approximately 500 metres wavelength (Sedlak et al., 2016). On these scales and larger, the waves and quasi-periodic structures have been shown to follow a Kolmogorov type power law, characterised by a wave power that decreases with the wavenumber of the structure raised to the exponent of -5/3 (Dewan et al., 1992; Hecht et al., 2005).

Vertical structures of smaller scales are more easily observed with LIDARS (Diettrich et al., 2005; Li et al., 2005; Fritts et al., 2017) or rocket measurements (Lübken, 1992; Hillert et al., 1994). These show that at vertical wavelength scales between 10 and 40 metres, the power

cascade breaks off from the Kolmogorov cascade and into a dissipative region, where the power of the wave or QPS falls off as the wavenumber to the power of -7 (Lübken et al., 1994; Thrane et al., 1994; Lübken et al., 2002; Müllemann et al., 2002).

As mentioned in section 3 and in paper 1 (Franzen et al., 2017), the NOTCam has a field of view of only 100 x 0.25 metres when projected onto the OH layer. The slit is so narrow that any effects across the width of the observed patch of sky can be ignored. Along the slit, the NOTCam detector has 1024 pixels. It, therefore, reaches a theoretical resolution of 10 cm per pixel. This resolution is of course not obtained in reality due to turbulent refraction in the troposphere, lens effects, pixel bleeding, and signal to noise considerations. Considering these limitations, the pixels along the slit could be summed to give a spatial resolution of approximately 1 metre on the night sky while increasing the signal to noise of the observations. Using dedicated telescope time of approximately 140 minutes, where the telescope was staring only at one spot of the sky, waves below 100 m wavelengths in the Q-branch of the (9,7) transition of the OH airglow could be observed along the slit. These waves could be traced from one integration to the next, which lasted either 10 s or 20 s, depending on the day of the observation. Figure 10 illustrates this with a simple sine-wave.

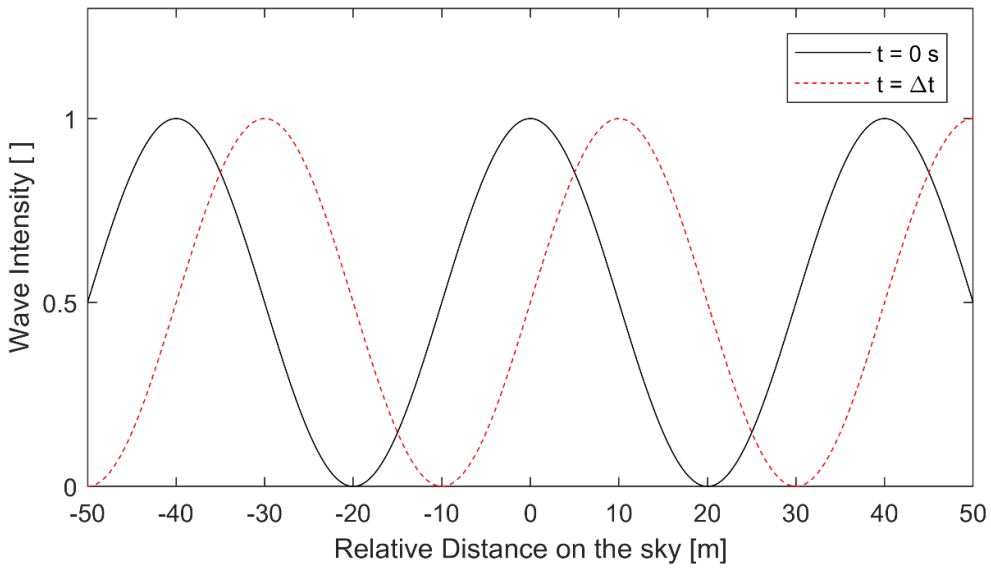

Figure 10: Sketch of a wave observation. At a start point, t = 0 s (black) the wave can be observed along the slit, with three maxima. After a time Δt, the wave has moved to the right and is now observed at a new location along the slit.

The wave at a given start time $t = 0$ s is shown in black. The red dashed line is the same wave along the slit after a time Δt, this time moved to the right. The vertical axis in this figure is the wave intensity. This means that in the NOTCam measurements, one can see bright spots at the maxima of the waves and dark spots at the minima of the waves moving along the slit length.

Figure 11 shows a spatial location versus time plot, sometimes called a keogram (Eather et al., 1976), that shows the progression of wavefronts across the slit. The y-axis is the spatial axis along the slit. Each column is, therefore, one picture along the slit. The x-axis is a time axis, and later observations are shown to the right. As in Figure 10, the wave seen in the first column has moved down (to the South) in the second figure. Three wave crests are highlighted in yellow to guide the eye. This example has a wavelength of approximately 33 metres and persists over a time period of nearly 600 seconds. Paper 2 (Franzen et al., 2018) reported 42 QPS events between 60 m and 4.5 m wavelength. Each event is coherent over at least one Brunt period, which is about 300 seconds in the MLT region (Andrews, 2010). Details on the extraction of the waves are presented in paper 2 (Franzen et al., 2018).

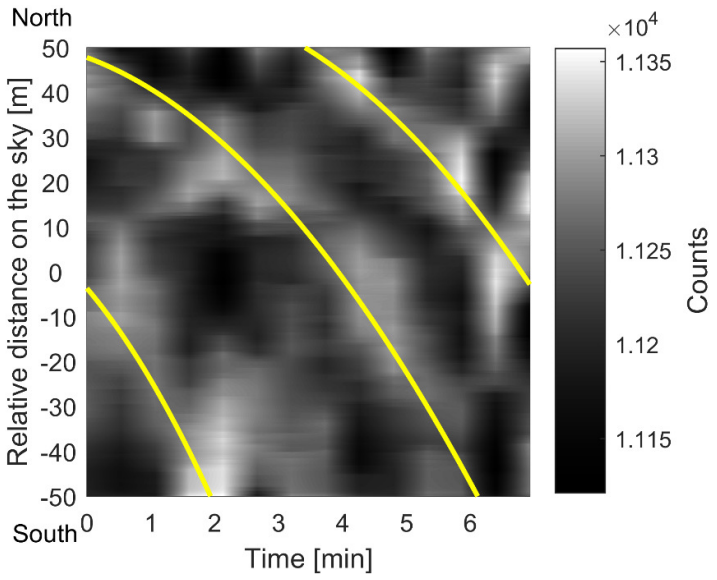

Figure 11: Keogram of an observed QPS. The horizontal axis is time, while the vertical axis is the spatial direction along the slit. Three crests are highlighted in yellow. Figure from Franzen et al. (2018).

The 42 QPS events reported in Paper 2 (Franzen et al., 2018) followed a Kolmogorov type cascade with an exponent of -5/3, even down to scales of 4.5-m wavelengths. The previously observed transition into the dissipative region at 10 to 40 metres for the vertical waves and QPSs seems not to hold for horizontal waves and QPSs. A parametrisation according to a Kolmogorov cascade can, therefore, be used in atmospheric models instead of other, more complex and time-consuming methods to account for wave breaking in the MLT region.

4.3 Paper 3

The OH airglow layer has a thickness of about 7 km, as shown in Figure 3. The temperature of the surrounding atmosphere and therefore the temperature through the OH layer is generally not constant. A ground-based observer can only observe the spectrum integrated through the whole OH layer. The assumption before was that this will show a density weighted average Boltzmann distribution from which an average temperature can be derived assuming LTE applies.

Usually, only lines with $N \leq 4$ are considered to be in LTE (Harrison et al., 1970; Harrison et al., 1971; Sivjee et al., 1972; Sivjee et al., 1987; Pendleton et al., 1993; Perminov et al., 2007). It is therefore common practice to fit a temperature distribution only to these lines. For the P-branch these lines correspond to the lowest three rotational lines. Different temperatures at different altitudes of the OH layer, combined with a fit to only the first three rotational lines, can influence the apparent population of the higher rotational levels.

To illustrate this, Figure 12 shows two different spectra of the (7,4) transition P_1-branch. Figure 12 a) shows the spectrum at a temperature of 150 K in blue. Note that most of the intensity comes from the lower rotational lines at shorter wavelengths. Figure 12 b) shows the same spectra in red, but at 300 K. The peak of the distribution increases to higher rotational lines at longer wavelengths. The highest vibrational lines are notably more populated than in Figure 12 a). These two temperatures are extreme for the MLT region and are used for illustrative purpose only. If these two spectra represent the OH airglow layer at two different altitudes, then a ground-based observer would only see the density weighted sum of each rotational line from below. Assuming the two levels contribute equally, this sum is shown as black crosses in Figure 12 c). A simple fit to the first three rotational lines yields a Boltzmann temperature of approximately 185 K. The magenta spectrum in Figure 12 c) has this temperature. For the lowest three lines, the magenta spectrum and the integrated spectrum in black fit very well. For higher vibrational lines, the integrated spectrum in black has far higher intensities than the fit

in magenta. It appears as if the integrated, observed spectrum has an apparent excess population (AEP) in the higher rotational levels, just as it would have if the spectrum were created under NLTE conditions. It was, however, created under strict LTE conditions. This AEP can therefore not be ascribed to any NLTE effects but comes from the influence of different temperatures in the OH airglow layer. The extent of this AEP is dependent on the different temperatures present in the OH layer.

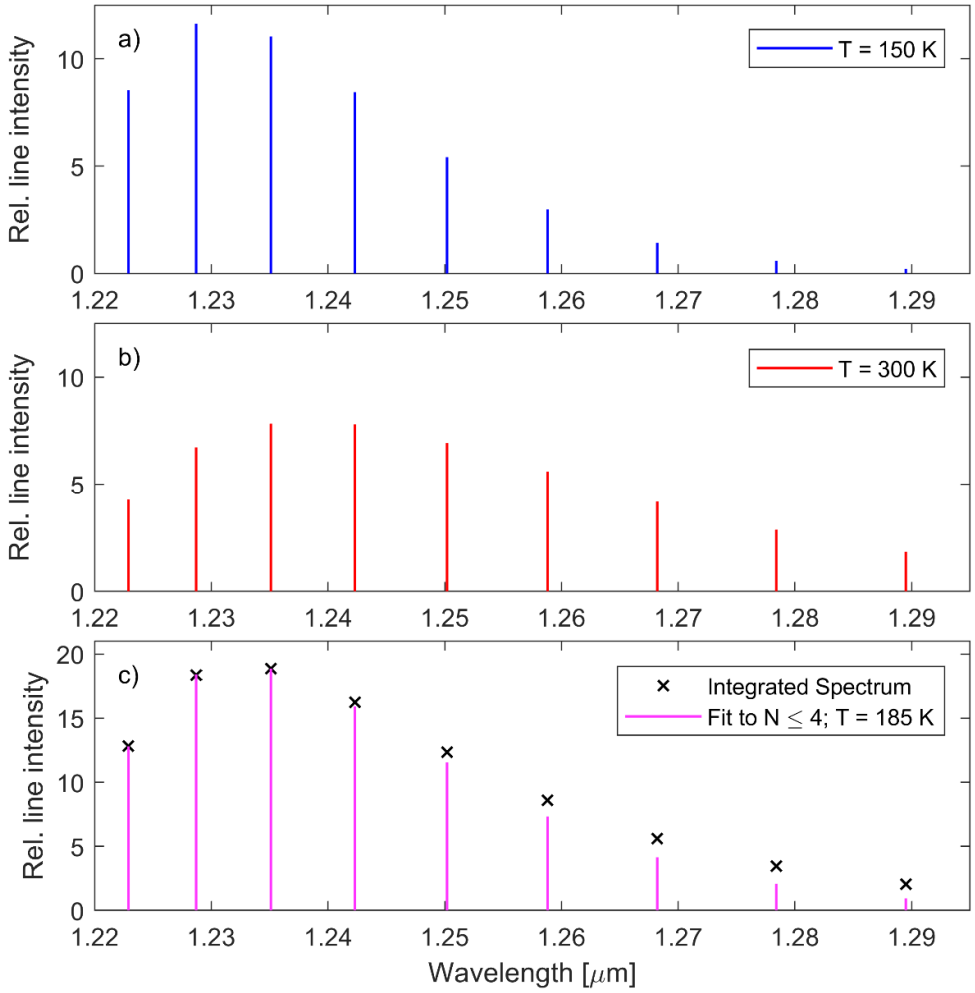

Figure 12: a) Calculated spectra of the (7,4) transition P_1-branch at 150 K. b) The same spectrum as in a), but at 300 K. c) In black crosses: the sum of the spectra in a) and b) as a ground-based observer would see, if a) and b) were at different altitudes of the same OH layer. In magenta: the fitted spectra to the first three lines (with $N \leq 4$). The fit temperature is 185 K. At higher rotational lines, the integrated spectrum seems to have an apparent excess population compared to the fit.

Paper 3 (Franzen et al., 2019a) simulated this effect. The paper looks at how much AEP can be expected from different climatological conditions and when waves with different amplitudes and wavelengths perturb the background temperature profile. The paper concludes that large waves in the atmosphere with an amplitude of 40 K and a wavelength of at least double the layer thickness can create an AEP of 40 % for the J' = 6.5 (N = 7) level. This effect will be most dominant for OH observations over periods commensurate with the wave period, where a wave will substantially modify the temperature slope through the layer. Paper 3 (Franzen et al., 2019a) therefore showed that large scale waves with vertical wavelengths over ten kilometres could change the OH airglow and the atmospheric parameters inferred by remote observations. These integration effects must be removed from spectroscopic data before the true, NLTE population can be observed and kinetic thermalisation models developed.

4.4 Paper 4

As stated in Equation (6), the intensity of any given line is only dependent on the degeneracy and population of the upper state and the Einstein coefficient of the transition. Given different lines originating from the same upper-level v', J', the difference in the line intensity is only due to the different Einstein coefficients A. If any two lines from the same upper levels are measured, the ratio between their intensities is therefore:

$$\frac{I_1}{I_2} = \frac{g_{v',J'}\, N_{v',J'}\, A_1}{g_{v',J'}\, N_{v',J'}\, A_2} = \frac{A_1}{A_2}. \tag{10}$$

There are always three different lines originating from a given upper state, ending in states that are separated by -1, 0 or +1 rotational quantum numbers. These three lines belong to the R-, Q- and P-branches respectively. Figure 13 illustrates a simple energy diagram for these three lines from an upper state v', J'. If one of the Einstein coefficients is known and the line intensities can be measured, the other two Einstein coefficients can be determined relative to the known transition probability.

French et al. (2000) measured these line ratios for the Q-branches of the (6,2) Meinel transition relative to the P-branch and found that the intensities of the Q-branch lines were consistently lower than tabulated values. Pendleton et al. (2002) explained these discrepancies as a result of a possible uncoupling of the electronic angular momentum from the inter-nuclear axis and coupling directly to the nuclear rotational angular momentum for the OH molecule in the (6,2) vibrational band. Following this explanation, it would appear that the Q-branch Einstein coefficients listed in HITRAN are generally too large relative to the P-branch coefficients.

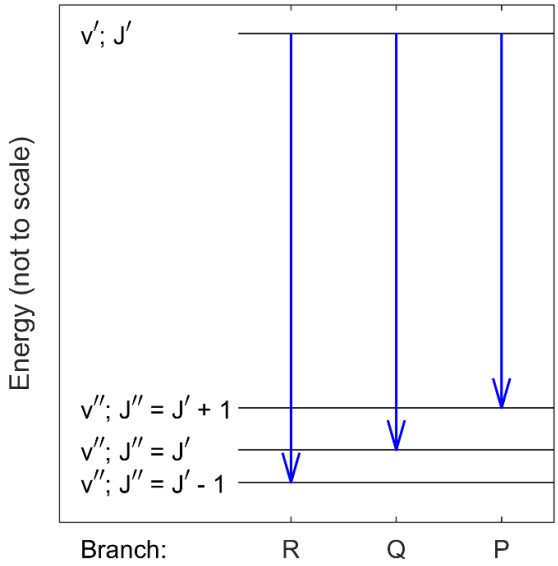

Figure 13: The transition from a given *v', J'* upper level to a different lower level *v'', J''* has three possible destinations, only varying in *J''*. The R-branch will end at *J''* = *J'* – 1, the Q-branch at *J''* = *J'* and the P-branch at *J''* = *J'* + 1. All three originate from the same upper level.

Paper 4 (Franzen et al., 2019b) measured these line ratios for seven other Meinel vibrational transitions. Of the eight transitions shown in Table 2, the intensities of the (8,6) rotational transitions were too heavily affected by atmospheric absorption and could not be used. However, consistent with the French et al. (2000) results, the other vibrational transitions generally showed Q-branch transition probabilities smaller than those listed in HITRAN. Figure 14 shows the (6,4) transitions as an example (red in the figure). The solid line with crosses are the line ratios derived from the NOTCam measurements; the dashed line with the circles are the HITRAN values. As a comparison, the findings from French et al. (2000) are shown in the same manner (black in the figure). While the absolute numbers are expected to be different for the different vibrational transitions, the shape of the deviation between measurements and the HITRAN values is comparable. The extent of the deviation depends on the vibrational transition in question. The mechanics of the OH airglow could, therefore, be observed on quantum scales.

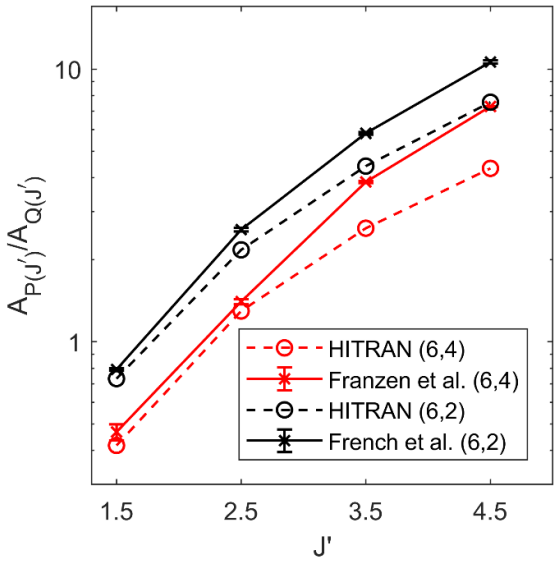

Figure 14: Line ratios of the (6,4) transition from paper 4 (Franzen et al., 2019b) in red and the (6,2) transition from French et al. (2000) in black. The dashed lines with circles are the corresponding values from the HITRAN database. Both publications show similar results, i.e. smaller Q-branch Einstein coefficients and intensities in the measurements compared to the calculations.

5. Conclusion

The starting point of this thesis was to employ astronomical spectroscopic data to remote sense the atmosphere. Since the OH airglow contaminates standard astronomical observations in the near infrared, the archive of telescope background spectra provides an extensive source of information for atmospheric research. Paper 1 (Franzen et al., 2017) showed how astronomical observations could be prepared for OH airglow measurements by masking out the star, removing the dark current and adjusting for the telescope optics.

The extracted spectra of the OH Meinel airglow have a very high signal-to-noise ratio and a high temporal and spatial resolution, compared to other observations. With observation of the (9,7) Meinel transition at zenith over about two hours of observations, I was able to detect wave-like intensity fluctuations or QPS on very small scales between 60 and 4.5 m. Paper 2 (Franzen et al., 2018) shows these QPS followed a Kolmogorov-type cascade for the whole wavelength region observed, suggesting that these QPS are breaking waves in the MLT. Other horizontal waves or QPS have been observed at the scales between one to hundreds of kilometres. These larger scale QPS also showed a Kolmogorov-type cascade with slope of - 5/3. My results are therefore an extension of the breaking QPS power spectrum to previously unobserved wavelength ranges. This extension makes it possible to use a Kolmogorov cascade parametrisation of the waves down to the metre scales, instead of using more time consuming and involved simulation methods.

With these high quality and long-exposure spectra, I was able to measure the Einstein coefficients of the Q-branches of seven different Meinel vibrational bands. These measurements extended the work of French et al. (2000), who found that the (6,2) Meinel transition had significantly smaller Einstein coefficients for the Q-branch than previously described. These unexpected results were explained by Pendleton et al. (2002) by an uncoupling of the electronic angular momentum from the inter-nuclear axis and directly with the nuclear rotational angular momentum. With the data from the NOT, I was able to show that several more transitions appear to have smaller Einstein coefficients than theoretically predicted and give precise numbers for the relative coefficients in paper 4 (Franzen et al., 2019b). I was also able to show that this effect varies with vibrational level, with levels $v' < 4$, where vibration-rotation effects are also smallest, least affected.

In paper 3 (Franzen et al., 2019a), I conducted a simulation of large scale waves in the atmosphere. Waves with wavelengths of several tens of kilometres and amplitudes of 20 and

more K can change the fitted temperatures to an OH airglow spectrum. This behaviour is possible due to different temperatures in different parts of the OH layer. A ground-based observation is only able to observe the integral through the whole layer and will not observe a single temperature profile, but a spectrum characterised by all temperatures in the layer. This integration can show apparent excess populations in high rotational levels of the OH. At the same time, these high apparent populations in the high *J'* levels resemble populations measured in conditions where the OH was in NLTE, even though my simulation was performed in strict LTE conditions. The effects of temperature variations across the OH airglow layer can contribute up to half of the excess emission intensity at high rotational levels, leading to overestimations of the NLTE populations that must be corrected in order to formulate thermalisation models.

To conclude, in this thesis, I have shown how useful astronomical spectral measurements can be to atmospheric OH airglow research on several scales. On quantum scales, they can be used to measure Einstein coefficients, on small scales of a few metres to observe small-scale QPS contributing to the wave-breaking process, and on large scales, waves can change the apparent behaviour of the rotational levels of the excited OH.

Bibliography

Abbott, T. M., Aspin, C., Sorensen, A. N., Norregaard, P., Andersen, J., Andersen, M. I., . . . Schwarz, H. E. (2000). Swir at the Nordic Optical Telescope: Notcam. In M. Iye & A. F. Moorwood (Eds.), *Optical and Ir Telescope Instrumentation and Detectors* (Vol. 4008, pp. 714-719). SPIE Proc. Vol. 4008, Munich.

Adler-Golden, S. (1997). Kinetic Parameters for OH Nightglow Modeling Consistent with Recent Laboratory Measurements. *Journal of Geophysical Research: Space Physics, 102*(A9), 19969-19976. doi:10.1029/97JA01622

Andrews, D. G. (2010). *An Introduction to Atmospheric Physics* (2 ed.). Cambridge: Cambridge University Press.

Baker, D. J., & Stair, J. A. T. (1988). Rocket Measurements of the Altitude Distributions of the Hydroxyl Airglow. *Phys Scripta, 37*(4), 611-622.

Caridade, P. J. S. B., Horta, J. Z. J., & Varandas, A. J. C. (2013). Implications of the O + OH Reaction in Hydroxyl Nightglow Modeling. *Atmos. Chem. Phys., 13*(1), 1-13. doi:10.5194/acp-13-1-2013

Carlos, J. I., & Marquez, F. G. (1988). Jefatura Del Estado *25332 LEY 31/1988 de 31 de octubre, sobre Protección de la Calidad Astronómica de los Observatorios del Instituto de Astrofísica de Canarias.* Madrid: Spanish Law.

Charters, P. E., Macdonald, R. G., & Polanyi, J. C. (1971). Formation of Vibrationally Excited OH by the Reaction H + O3. *Applied Optics, 10*(8), 1747-1754. doi:10.1364/AO.10.001747

Cosby, P. C., & Slanger, T. G. (2007). OH Spectroscopy and Chemistry Investigated with Astronomical Sky Spectra. *Canadian Journal of Physics, 85*(2), 77-99. doi:10.1139/p06-088

Dewan, E. M., Pendleton, W., Grossbard, N., & Espy, P. (1992). Mesospheric OH Airglow Temperature Fluctuations: A Spectral Analysis. *Geophysical Research Letters, 19*(6), 597-600. doi:10.1029/92GL00391

Diettrich, J. C., Nott, G. J., Espy, P. J., Swenson, G. R., Chu, X., Taylor, M. J., . . . Fritts, D. C. (2005). High Frequency Atmospheric Gravity-Wave Properties Using Fe-Lidar and OH-Imager Observations. *Geophysical Research Letters, 32*(9), 1-4. doi:10.1029/2004GL021944

Eather, R. H., Mende, S. B., & Judge, R. J. R. (1976). Plasma Injection at Synchronous Orbit and Spatial and Temporal Auroral Morphology. *Journal of Geophysical Research, 81*(16), 2805-2824. doi:10.1029/JA081i016p02805

Franzen, C., Espy, P. J., & Hibbins, R. E. (2019a). Effects of Temperature Gradients and Waves on the Temperature Derived from Hydroxyl Airglow. *Submitted in Atmospheric Chemistry and Physics*.

Franzen, C., Espy, P. J., Hibbins, R. E., & Djupvik, A. A. (2018). Observation of Quasiperiodic Structures in the Hydroxyl Airglow on Scales Below 100 M. *Journal of Geophysical Research: Atmospheres, 123*(19), 10,935-910,942. doi:10.1029/2018JD028732

Franzen, C., Espy, P. J., Hofmann, N., Hibbins, R. E., & Djupvik, A. A. (2019b). Measurements of Q-Branch Transition Probabilities for Several Hydroxyl Meinel Bands. *To be submitted in Journal of Quantitative Spectroscopy & Radiative Transfer*.

Franzen, C., Hibbins, R. E., Espy, P. J., & Djupvik, A. A. (2017). Optimizing Hydroxyl Airglow Retrievals from Long-Slit Astronomical Spectroscopic Observations. *Atmospheric Measurement Techniques, 10*(8), 3093-3101. doi:10.5194/amt-10-3093-2017

French, W. J. R., Burns, G. B., Finlayson, K., Greet, P. A., Lowe, R. P., & Williams, P. F. B. (2000). Hydroxyl (6/2) Airglow Emission Intensity Ratios for Rotational Temperature Determination. *Annales Geophysicae, 18*(10), 1293-1303. doi:10.1007/s00585-000-1293-2

Fritts, D. C., Wang, L., Baumgarten, G., Miller, A. D., Geller, M. A., Jones, G., . . . Vinokurov, J. (2017). High-Resolution Observations and Modeling of Turbulence Sources, Structures, and Intensities in the Upper Mesosphere. *Journal of Atmospheric and Solar-Terrestrial Physics, 162*(Supplement C), 57-78. doi:https://doi.org/10.1016/j.jastp.2016.11.006

Harrison, A. W., Evans, W. F. J., & Llewellyn, E. J. (1971). Study of the (4–1) and (5–2) Hydroxyl Bands in the Night Airglow. *Canadian Journal of Physics, 49*(19), 2509-2517. doi:10.1139/p71-297

Harrison, A. W., Llewellyn, E. J., & Nicholls, D. C. (1970). Night Airglow Hydroxyl Rotational Temperatures. *Canadian Journal of Physics, 48*(15), 1766-1768. doi:10.1139/p70-224

Hecht, J. H., Liu, A. Z., Walterscheid, R. L., & Rudy, R. J. (2005). Maui Mesosphere and Lower Thermosphere (Maui Malt) Observations of the Evolution of Kelvin-Helmholtz

Billows Formed near 86 Km Altitude. *Journal of Geophysical Research: Atmospheres, 110*(D9), 1-19. doi:10.1029/2003JD003908

Herzberg, G. (1950). *Molecular Spectra and Molecular Strucutre. I. Spectra of the Diatomic Molecule*. New York: D. Van Nostrand Company, Inc.

Hillert, W., Lübken, F. J., & Lehmacher, G. (1994). Total: A Rocket-Borne Instrument for High Resolution Measurements of Neutral Air Turbulence During Dyana. *Journal of Atmospheric and Terrestrial Physics, 56*(13), 1835-1852. doi:https://doi.org/10.1016/0021-9169(94)90013-2

Holton, J. R. (1982). The Role of Gravity Wave Induced Drag and Diffusion in the Momentum Budget of the Mesosphere. *Journal of the Atmospheric Sciences, 39*(4), 791-799. doi:10.1175/1520-0469(1982)039<0791:trogwi>2.0.co;2

Holton, J. R. (1983). The Influence of Gravity Wave Breaking on the General Circulation of the Middle Atmosphere. *Journal of the Atmospheric Sciences, 40*(10), 2497-2507. doi:10.1175/1520-0469(1983)040<2497:tiogwb>2.0.co;2

Klenerman, D., & Smith, I. W. M. (1987). Infrared Chemiluminescence Studies Using a Sisam Spectrometer. Reactions Producing Vibrationally Excited OH. *Journal of the Chemical Society, Faraday Transactions 2: Molecular and Chemical Physics, 83*(1), 229-241. doi:10.1039/F29878300229

Langhoff, S. R., Werner, H. J., & Rosmus, P. (1986). Theoretical Transition Probabilities for the OH Meinel System. *Journal of Molecular Spectroscopy, 118*(2), 507-529. doi:https://doi.org/10.1016/0022-2852(86)90186-4

Li, F., Liu, A. Z., Swenson, G. R., Hecht, J. H., & Robinson, W. A. (2005). Observations of Gravity Wave Breakdown into Ripples Associated with Dynamical Instabilities. *Journal of Geophysical Research: Atmospheres, 110*(D9), 1-12. doi:10.1029/2004JD004849

Lindzen, R. S. (1981). Turbulence and Stress Owing to Gravity Wave and Tidal Breakdown. *Journal of Geophysical Research: Oceans, 86*(C10), 9707-9714. doi:10.1029/JC086iC10p09707

Lübken, F. J. (1992). On the Extraction of Turbulent Parameters from Atmospheric Density Fluctuations. *Journal of Geophysical Research: Atmospheres, 97*(D18), 20385-20395. doi:doi:10.1029/92JD01916

Lübken, F. J., Hillert, W., Lehmacher, G., von Zahn, U., Blix, T. A., Thrane, E. V., . . . Knyazev, A. K. (1994). Morphology and Sources of Turbulence in the Mesosphere

During Dyana. *Journal of Atmospheric and Terrestrial Physics, 56*(13), 1809-1833. doi:https://doi.org/10.1016/0021-9169(94)90012-4

Lübken, F. J., Rapp, M., & Hoffmann, P. (2002). Neutral Air Turbulence and Temperatures in the Vicinity of Polar Mesosphere Summer Echoes. *Journal of Geophysical Research: Atmospheres, 107*(D15), ACL 9-1-ACL 9-10. doi:10.1029/2001JD000915

Maylotte, D. H., Polanyi, J. C., & Woodall, K. B. (1972). Energy Distribution among Reaction Products. Iv. X+Hy (X ≡ Cl, Br; Y ≡ Br, I), Cl+Di. *The Journal of Chemical Physics, 57*(4), 1547-1560. doi:10.1063/1.1678436

McDade, I. C., & Llewellyn, E. J. (1987). Kinetic Parameters Related to Sources and Sinks of Vibrationally Excited OH in the Nightglow. *Journal of Geophysical Research: Space Physics, 92*(A7), 7643-7650. doi:10.1029/JA092iA07p07643

Meinel, A. B. (1950a). OH Emission Bands in the Spectrum of the Night Sky. I. *Astrophys J, 111*, 555-564.

Meinel, A. B. (1950b). OH Emission Bands in the Spectrum of the Night Sky. Ii. *Astrophys J, 112*, 120-130.

Mies, F. H. (1974). Calculated Vibrational Transition Probabilities of OH(X2π). *Journal of Molecular Spectroscopy, 53*(2), 150-188. doi:https://doi.org/10.1016/0022-2852(74)90125-8

Mlynczak, M. G. (1997). Energetics of the Mesosphere and Lower Thermosphere and the Saber Experiment. *Advances in Space Research, 20*(6), 1177-1183. doi:https://doi.org/10.1016/S0273-1177(97)00769-2

Mlynczak, M. G., Hunt, L. A., Marshall, B. T., Mertens, C. J., Marsh, D. R., Smith, A. K., . . . Gordley, L. L. (2014). Atomic Hydrogen in the Mesopause Region Derived from Saber: Algorithm Theoretical Basis, Measurement Uncertainty, and Results. *Journal of Geophysical Research: Atmospheres, 119*(6), 3516-3526. doi:doi:10.1002/2013JD021263

Müllemann, A., Rapp, M., Lübken, F. J., & Hoffmann, P. (2002). In Situ Measurements of Mesospheric Turbulence During Spring Transition of the Arctic Mesosphere. *Geophysical Research Letters, 29*(10), 115-111-115-114. doi:10.1029/2002GL014841

Noll, S., Kausch, W., Kimeswenger, S., Unterguggenberger, S., & Jones, A. M. (2015). OH Populations and Temperatures from Simultaneous Spectroscopic Observations of 25 Bands. *Atmos. Chem. Phys., 15*(7), 3647-3669.

Ohoyama, H., Kasai, T., Yoshimura, Y., Kimura, H., & Kuwata, K. (1985). Initial Distribution of Vibration of the OH Radicals Produced in the H + O3 → OH(X2π1/2,3/2) + O2

Reaction. Chemiluminescence by a Crossed Beam Technique. *Chemical Physics Letters, 118*(3), 263-266. doi:https://doi.org/10.1016/0009-2614(85)85312-4

Pendleton, W. R., Espy, P. J., & Hammond, M. R. (1993). Evidence for Non-Local-Thermodynamic-Equilibrium Rotation in the OH Nightglow. *Journal of Geophysical Research: Space Physics, 98*(A7), 11567-11579. doi:10.1029/93JA00740

Pendleton, W. R., & Taylor, M. J. (2002). The Impact of L-Uncoupling on Einstein Coefficients for the OH Meinel (6,2) Band: Implications for Q-Branch Rotational Temperatures. *Journal of Atmospheric and Solar-Terrestrial Physics, 64*(8), 971-983. doi:https://doi.org/10.1016/S1364-6826(02)00051-2

Perminov, V. I., Semenov, A. I., & Shefov, N. N. (2007). On Rotational Temperature of the Hydroxyl Emission. *Geomagn Aeron+, 47*(6), 756-763. doi:10.1134/s0016793207060084

Pickett, H. M., Poynter, R. L., Cohen, E. A., Delitsky, M. L., Pearson, J. C., & Müller, H. S. P. (1998). Submillimeter, Millimeter, and Microwave Spectral Line Catalog. *Journal of Quantitative Spectroscopy and Radiative Transfer, 60*(5), 883-890. doi:https://doi.org/10.1016/S0022-4073(98)00091-0

Picone, J. M., Hedin, A. E., Drob, D. P., & Aikin, A. C. (2002). Nrlmsise-00 Empirical Model of the Atmosphere: Statistical Comparisons and Scientific Issues. *J Geophys Res-Space, 107(A12)*, 1468. doi:10.1029/2002JA009430

Polanyi, J. C., & Sloan, J. J. (1975, 1975-01-01). *Detailed Rate Constants for the Reactions H + O3 --> OH(Nu',J') + O2 and H + No2 --> OH(Nu'',J') + No.* Paper presented at the Symposium on chemical kinetics data for the upper and lower atmosphere, United States.

Polanyi, J. C., & Woodall, K. B. (1972). Energy Distribution among Reaction Products. Vi. F+H2, D2. *The Journal of Chemical Physics, 57*(4), 1574-1586. doi:10.1063/1.1678438

Rothman, L. S., Gordon, I. E., Babikov, Y., Barbe, A., Chris Benner, D., Bernath, P. F., . . . Wagner, G. (2013). The Hitran2012 Molecular Spectroscopic Database. *J Quant Spectrosc Ra, 130*, 4-50.

Russell, J. M., Mlynczak, M. G., Gordley, L. L., Tansock, J., & Esplin, R. (1999). An Overview of the Saber Experiment and Preliminary Calibration Results. In A. M. Larar (Ed.), *Optical Spectroscopic Techniques and Instrumentation for Atmospheric and Space Research Iii* (Vol. 3756, pp. 277-288). Bellingham: Spie-Int Soc Optical Engineering.

Sedlak, R., Hannawald, P., Schmidt, C., Wust, S., & Bittner, M. (2016). High-Resolution Observations of Small-Scale Gravity Waves and Turbulence Features in the OH Airglow Layer. *Atmospheric Measurement Techniques, 9*(12), 5955-5963. doi:10.5194/amt-9-5955-2016

Sivjee, G. G., Dick, K. A., & Feldman, P. D. (1972). Temporal Variations in Night-Time Hydroxyl Rotational Temperature. *Planetary and Space Science, 20*(2), 261-269. doi:https://doi.org/10.1016/0032-0633(72)90107-9

Sivjee, G. G., & Hamwey, R. M. (1987). Temperature and Chemistry of the Polar Mesopause OH. *J Geophys Res-Space, 92*(A5), 4663-4672. doi:10.1029/JA092iA05p04663

Thrane, E. V., Blix, T. A., Hoppe, U. P., Lübken, F. J., Hillert, W., Lehmacher, G., & Fritts, D. C. (1994). A Study of Small-Scale Waves and Turbulence in the Mesosphere Using Simultaneous in Situ Observations of Neutral Gas and Plasma Fluctuations. *Journal of Atmospheric and Terrestrial Physics, 56*(13), 1797-1808. doi:https://doi.org/10.1016/0021-9169(94)90011-6

Turnbull, D. N., & Lowe, R. P. (1989). New Hydroxyl Transition Probabilities and Their Importance in Airglow Studies. *Planetary and Space Science, 37*(6), 723-738. doi:https://doi.org/10.1016/0032-0633(89)90042-1

von Savigny, C., McDade, I. C., Eichmann, K. U., & Burrows, J. P. (2012). On the Dependence of the OH* Meinel Emission Altitude on Vibrational Level: Sciamachy Observations and Model Simulations. *Atmospheric Chemistry and Physics, 12*(18), 8813-8828.

6. Publications

Paper 1

Franzen, C., Hibbins, R. E., Espy, P. J., & Djupvik, A. A. (2017). Optimizing hydroxyl airglow retrievals from long-slit astronomical spectroscopic observations. Atmospheric Measurement Techniques, 10(8), 3093-3101. doi:10.5194/amt-10-3093-2017

Atmos. Meas. Tech., 10, 3093–3101, 2017
https://doi.org/10.5194/amt-10-3093-2017

Atmospheric Measurement Techniques
Open Access
EGU

Optimizing hydroxyl airglow retrievals from long-slit astronomical spectroscopic observations

Christoph Franzen[1,2,*], **Robert Edward Hibbins**[1,2], **Patrick Joseph Espy**[1,2], **and Anlaug Amanda Djupvik**[3]

[1]Norwegian University of Science and Technology (NTNU), 7491 Trondheim, Norway
[2]Birkeland Centre for Space Science (BCSS), Birkeland, Norway
[3]Nordic Optical Telescope, 38700 Santa Cruz De La Palma, Spain
[*] *Invited contribution by Christoph Franzen, recipient of the EGU Atmospheric Sciences Outstanding Student Poster and PICO Award 2016.*

Correspondence to: Christoph Franzen (christoph.franzen@ntnu.no)

Received: 3 February 2017 – Discussion started: 22 March 2017
Revised: 27 June 2017 – Accepted: 11 July 2017 – Published: 25 August 2017

Abstract. Astronomical spectroscopic observations from ground-based telescopes contain background emission lines from the terrestrial atmosphere's airglow. In the near infrared, this background is composed mainly of emission from Meinel bands of hydroxyl (OH), which is produced in highly excited vibrational states by reduction of ozone near 90 km. This emission contains a wealth of information on the chemical and dynamical state of the Earth's atmosphere. However, observation strategies and data reduction processes are usually optimized to minimize the influence of these features on the astronomical spectrum. Here we discuss a measurement technique to optimize the extraction of the OH airglow signal itself from routine J-, H-, and K-band long-slit astronomical spectroscopic observations. As an example, we use data recorded from a point-source observation by the Nordic Optical Telescope's intermediate-resolution spectrograph, which has a spatial resolution of approximately 100 m at the airglow layer. Emission spectra from the OH vibrational manifold from $v' = 9$ down to $v' = 3$, with signal-to-noise ratios up to 280, have been extracted from 10.8 s integrations. Rotational temperatures representative of the background atmospheric temperature near 90 km, the mesosphere and lower thermosphere region, can be fitted to the OH rotational lines with an accuracy of around 0.7 K. Using this measurement and analysis technique, we derive a rotational temperature distribution with v' that agrees with atmospheric model conditions and the preponderance of previous work. We discuss the derived rotational temperatures from the different vibrational bands and highlight the potential for both the archived and future observations, which are at unprecedented spatial and temporal resolutions, to contribute toward the resolution of long-standing problems in atmospheric physics.

1 Introduction

1.1 OH airglow

The atmospheric region between 85 and 90 km represents a transition zone that lies between the thermosphere, where collisions are rare, and the collision-dominated, well-mixed mesosphere. This mesosphere and lower thermosphere (MLT) region is highly variable both chemically and dynamically (Smith, 2004, 2012). It is driven from above by diurnal, seasonal, and long-term changes in solar insolation and from below by tides, planetary waves, and upward-propagating gravity waves.

Photochemical reactions in the MLT play a key role in the vertical distribution of energy. The major loss for mesopause ozone is its reduction to molecular oxygen via

$$\mathrm{H} + \mathrm{O_3} \rightarrow \mathrm{OH^*} + \mathrm{O_2}. \quad \text{(R1)}$$

This loss is balanced by the major source of the ozone, the combination of molecular and atomic oxygen via a mediator M:

$$\mathrm{O} + \mathrm{O_2} + \mathrm{M} \rightarrow \mathrm{O_3} + \mathrm{M}, \quad \text{(R2)}$$

where the atomic oxygen is formed by the dissociation of molecular oxygen by solar radiation (Espy and Stegman,

2002; Sigernes et al., 2003). Reaction (R1) is highly exothermic (> 3 eV), leading to production of vibrational levels from $v' = 7$ to $v' = 9$ of the OH product. Deactivation of these high vibrational states primarily occurs through photo-emission in the Meinel bands (Meinel, 1950), resulting in the bright OH airglow, localized in a thick (∼ 8 km thick) layer near 90 km, that can be observed in the visible and infrared. Collisions of each long-lived vibrational excited state (v') with the surrounding gas effectively thermalize the lower, closely spaced rotational states into a Boltzmann distribution (Pendleton et al., 1993). Hence, moderate-resolution spectroscopic measurements of the relative population of the rotational levels of individual OH vibrational bands can be used to remotely sense the temperature of the mesopause region. Furthermore, the relative intensity of the individual vibrational bands can be used to estimate the relative populations of the v' states. Comprehensive reviews on ground-based observations of OH and their applications to mesopause chemistry can be found in von Zahn et al. (1987), Yee et al. (1997), and Smith et al. (2010).

However, achieving high temporal resolution has often only been possible at low spatial resolution (and vice versa). In this paper we use J-, H-, and K-band long-slit observations of an astronomical point source made by the Nordic Optical Telescope near-infrared camera and spectrograph (NOTCam). This intermediate-resolution spectrometer was used to obtain high-quality, very high spatial (< 100 m) resolution observations with short integration times (∼ 10 s). We demonstrate how to extract and optimize OH atmospheric spectral data from these astronomical observations and discuss the quality and validity of the derived data over the range of vibrational bands. Finally, we consider some problems of atmospheric physics that can be addressed with these new data.

1.2 Instrumentation

Founded in 1984 and located in La Palma, Spain (17°53′ W, 28°45′ N), the Nordic Optical Telescope (NOT) has a primary mirror with a diameter of 2560 mm (Djupvik and Andersen, 2010). Its near-infrared camera and spectrograph, NOTCam (Abbott et al., 2000), has been used for imaging since June 2001 and spectroscopy since August 2003. The detector is a 1024×1024 pixel Rockwell Science Center HgCdTe Astronomical Wide Area Infrared Imaging (HAWAII) array. The low-resolution mode ($R = \lambda/\Delta\lambda \sim 2100$) is sufficient to resolve the individual rotational lines of an OH vibrational level. The dispersing element is an echelle grism used together with broadband filters to sort the orders. In low-resolution spectroscopic mode the slit employed has a width of 128 µm, corresponding to approximately 0.6 arcsec on the sky, and a slit length of 4 arcmin. At an approximate OH layer altitude of 87 km (Baker and Stair Jr., 1988), 4 arcmin corresponds to around 100 m on the sky. The detector has a dead time of about 10 s due to reading out processes after each integration. Further details on NOTCam spectroscopy can be found in Telting (2016), and a description of the NOTCam in Djupvik (2016).

During point-source astronomical observations, measurements in the J, H, and K bands (1.165–1.328, 1.484–1.780, and 2.038–2.363 nm, respectively) are typically taken. Although each of these wavelength bands is observed individually, atmospheric OH vibrational band transitions (7, 4) and (8, 5) are simultaneously observed in the J band; the (3, 1), (4, 2), (5, 3), and a part of the (6 ,4) in the H band; and the (8, 6) and (9, 7) in the K band (Meinel, 1950). The (9, 7) band is of particular interest as it represents the highest vibrational level populated by Reaction (R1).

2 Data reduction

To demonstrate the data reduction procedures required to optimize the OH signal from routine astronomical observations, a single H-band spectroscopic exposure toward the star 21 Vir (spectral type B9V, $H = 5.64$ mag) with an exposure time of 10.8 s was used. This exposure time was chosen as an example as it is the shortest exposure time available in the archive, although the methods presented here were developed and optimized for a variety of conditions with integration times up to 600 s, which is the longest integration time available in the archive.

The H-band image presented here was taken in good astronomical observing conditions at an air mass of 1.516 at 05:50 UT on 19 February 2013, together with dark frames and flat fields recorded with a halogen lamp on the same night. The J- and K-band images presented in Sect. 3.2 were recorded toward the same object with the same integration time within 5 min of the H-band observation. The raw image frame is reproduced in Fig. 1a. The vertical bright band in Fig. 1a, located slightly to the left on the detector, is the H-band spectrum of the star. The weaker, nearly horizontal lines that curve upward are the atmospheric OH lines from the (3, 1), (4, 2), (5, 3), and (part of the) (6, 4) vibrational bands, listed from top to bottom in the image frame.

For the initial data reduction steps standard Image Reduction and Analysis Facility (IRAF; Tody, 1993) astronomical procedures were followed. This entailed removing bad pixels (zero valued or cold) that are known and stable, and dark frames were used to create a pixel mask to remove hot pixels on the detector. The intensity of the OH lines is well within the linear range of the array, so non-linearity effects could be ignored. The dark current was removed using dark images taken toward the closed dome before observations began. Wavelength-dependent variations in transmission and detector response were corrected by flat fielding using short integrations of a halogen lamp with a known colour temperature situated at the upper end of the optical path.

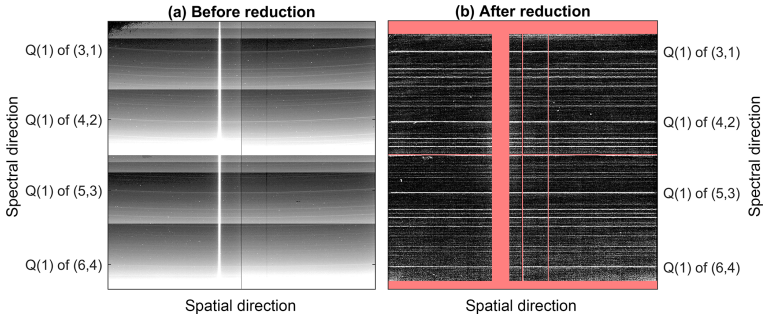

Figure 1. (a) The array in its raw form. The bright star is visible as a vertical band slightly to the left of centre. The curved OH lines are visible in the background. **(b)** The array after cleaning and flat fielding, with the star removed and the OH lines straightened. The unusable parts of the array are blanked out in red, and the OH lines can be seen clearly.

The stellar spectrum is much brighter than the OH lines and has to be removed. A linear mask, 60 pixels wide in the spatial direction and centred on the star's horizontal position, was applied to the detector frame. Sixty pixels removed the stellar influence while maintaining as much OH data as possible. The remaining OH lines do not appear as straight lines on the array due to the intersection of the array detector with the telescope's diffraction optics. Instead they are parabolic, with a curvature that varies linearly with spectral position. To straighten them for integration, a line's spatial and spectral pixels (x, y') were mapped to a coordinate system where the line appears at the same spectral location, y, along the entire spatial extent, x, using the function $y = y' + (x - p_1)^2 \cdot p_2$. The detector is aligned such that the central position of the parabola, p_1, is constant at column number 465, and the curvature, p_2, is given by $p_2 = 3 \times 10^{-5} + 5.3 \times 10^{-8} \cdot y'$. The result after processing is shown in Fig. 1b.

Given this transformation, the OH lines could then be integrated in the spatial dimension, x, for a given value of wavelength, y, with the standard deviation used to estimate each line's uncertainty, to form a high signal-to-noise spectrum (after accounting for the pixels masked out as described above). Gaussian functions with a full width at half maximum of 0.42, 0.73, and 0.87 nm were found to fit the line shape of the resulting OH lines in the centres of the J, H, and K bands, respectively, to within the noise present in the data. The fitting however is performed in units of pixels rather than nanometres. The line width is constant in pixel units for each band separately at 2.27 pixels.

Since the wavelengths of the OH lines are known (Rothman et al., 2013), and the lines are easy to identify, the abundant lines themselves were used for wavelength calibration. The brightest lines of the Q branch and the six brightest P-branch lines of each transition were used for the calibration of each filter band. For the H-band example presented here, this led to a calibration based on 22 pixel–wavelength pairs (only the main Q-branch lines were used for the (6, 4) transition). The wavelength calibration has only small non-linear contributions.

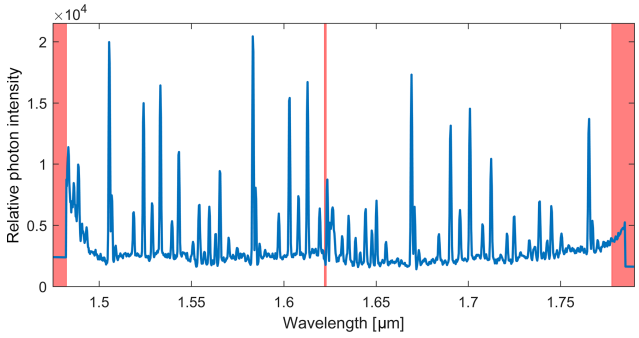

Figure 2. H-band spectrum of atmospheric OH extracted from the data frame presented in Fig. 1. Red shading highlights parts of the spectrum not used in the subsequent rotational temperature fitting.

3 Results

3.1 H-band data

In Fig. 2 the resulting H-band spectrum is shown based on the total integration time of 10.8 s. The spectrum has been corrected using a relative spectral radiance calibration derived from the flat-field source. However, an absolute calibration could be achieved using observations of a standard star of known intensity. The absolute calibration is however not needed for this work as we are only interested in the hydroxyl temperatures. The flat fielding distorts the edges of the spectrum slightly as the filter transmission nears zero in the red highlighted regions in the figure. At the long-wavelength end, the Q and R branches from the (6, 4) transition can be seen. The other three resolved bands belong to the (3, 1), (4, 2), and (5, 3) transitions. The signal-to-noise ratio is 280 for the Q-branch lines and around 200 for the P-branch lines for this 10.8 s exposure. Longer integration times increase these ratios further.

As can be seen in Fig. 2, the background is not completely flat but has low-frequency variations that span wavelength ranges greater than the OH line widths. Since these background variations will influence the relative intensities of the

individual rotational lines, they impact the fitted OH rotational temperature since it is strongly dependent on the relative heights of the lines. For this reason a seventh-order Butterworth infinite-impulse-response (IIR) filter with a cut-off (-3 dB point) at $\frac{1}{3.3\,\mathrm{nm}}$ was applied to the extracted 2-D spectra to remove the low-frequency variability. This filter was optimized through repeated tests on synthetic OH spectra to have minimal impact on the temperatures derived from the OH rotational lines. Figure 3a and b show the (5, 3) vibrational band before and after application of this filter. After filtering, the spectrum was normalized such that the sum over the absolute values of the spectrum was equal to 1.

A model spectrum was created using the OH line strengths, $S_{j'j''}$, for a given vibrational transition, tabulated in the HIgh-resolution TRANsmission (HITRAN) molecular absorption database (Rothman et al., 2013). The number of photons emitted in each rotational transition, assuming a Boltzmann distribution of population in the upper-state rotational levels, is given by

$$I = N_{v'} \cdot S_{j'j''} \cdot \left(\nu_{j'j''}\right)^3 \cdot \exp\left(-\frac{E_{j'}}{kT_{\mathrm{rot}}}\right).$$

Here $N_{v'}$ is the relative population of the upper vibrational level, v', and $\nu_{j'j''}$ is the wavenumber of the transition from the upper state level at potential energy $E_{j'}$ to the final rotational state at energy $E_{j''}$. To form the model spectrum, these relative line intensities were convolved with the instrumental line shape and then filtered and normalized in the same manner as the data. A χ^2 minimization using the rotational temperature and a total intensity scaling factor as the variable parameters was then performed between the model and the data to determine the rotational temperature best fitting the data. A Brent algorithm (Brent, 1973) from the GNU Scientific Library (Galassi and Gough, 2009) was used for the minimization. Following Pendleton et al. (1989), only rotational lines originating from levels $N \leq 4$ were used in the fitting, since higher levels may not be thermalized. The temperature fitting routine was tested against model data with added Gaussian white noise where temperatures were varied between 150 and 400 K. The resulting fit was found to reproduce the input rotational temperatures to within the fitting errors of the temperature parameter.

Figure 3c shows the data from Fig. 3b along with the fitted model spectrum shown as the red line. The fitted temperature in this case is found to be 186.5 ± 0.7 K, representing a 0.4 % relative uncertainty. The residual spectrum (data fit) is shown in Fig. 3d, where it may be seen that, although small differences in the wavelength calibration or line shape may occur, the fitted spectrum accurately represents the observation. This and similar tests for the other Meinel bands and different integration times demonstrate that the model used is robust, that fitting the high-pass-filtered data works well, and that the fit to the data converges to a temperature with a small error.

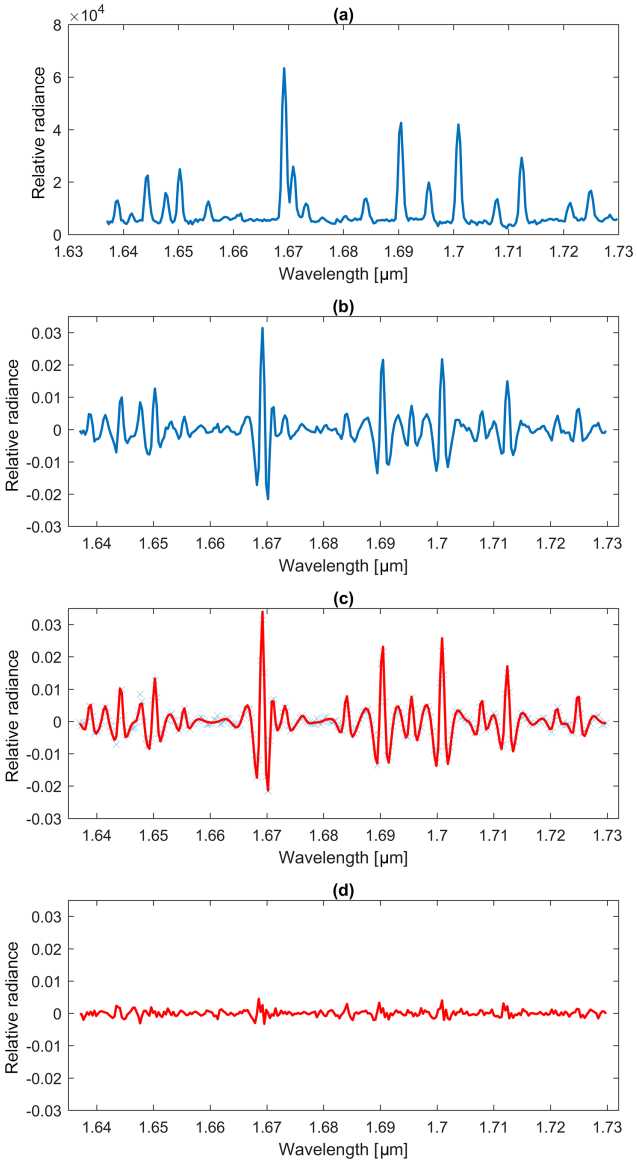

Figure 3. **(a)** Unfiltered spectrum of the (5, 3) transition. **(b)** Filtered spectrum of the (5, 3) transition. **(c)** Normalized spectrum from **(b)** (blue crosses) with the fitted, filtered model spectrum shown in red. The fitted rotational temperature is 186.5 ± 0.7 K. **(d)** Residuals of the fit from **(c)**.

3.2 Other vibrational bands

Figure 4 shows an overview of all the measured OH vibrational transitions recorded in the H-, J-, and K-band spectra taken toward the same star, extracted in the manner outlined above. The measurements in the J and K band were executed at 05:53 and 05:47 UT, respectively, meaning that the total time between all observations was about 6 min. All spectra were taken with the same 10.8 s integration time and are normalized to the same Q-branch intensity for comparison. For the majority of vibrational transitions, the signal is

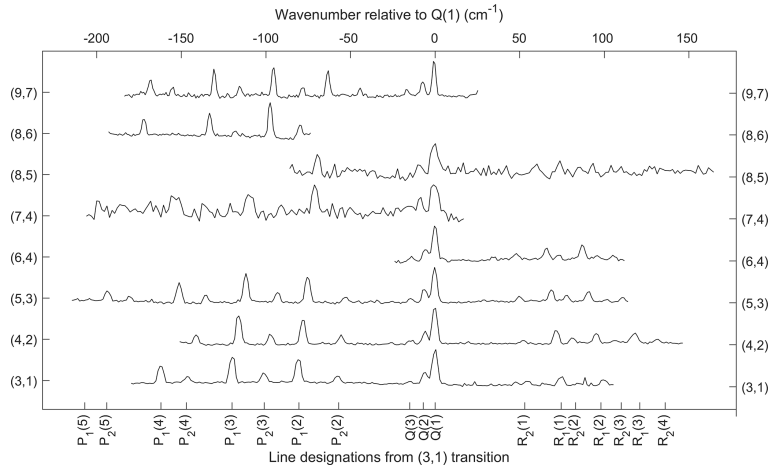

Figure 4. Spectra from the H, J, and K bands in wavenumbers relative to the Q(1) line in each band. The Q(1) lines of each spectrum are aligned. Line positions for the (3, 1) transition are shown.

very much greater than the noise, providing excellent data for temperature fitting, especially for the transitions in the H and K bands.

Since the (7, 4) and (8, 5) transitions in the J band have a $\Delta v = 3$, the lines are not as intense as in the other $\Delta v = 2$ bands. Due to the lower intensities of these $\Delta v = 3$ bands, the signal-to-noise ratio is substantially reduced for this short integration, which is typical of the NOTCam data. As a result, the fitting error for these bands was very large. While longer exposures, or the co-addition of sequential short exposures, would improve the fitting error of the OH (7, 4) band, the R and Q branches of the (8, 5) band are overlapped by the optically thick O_2 infrared atmospheric band at 1270 nm, and the filter cut-off reduces its $P_1(4)$ line to near the noise level. Thus, the temperatures for the (8, 5) bands would remain compromised even for longer integrations.

3.3 Temperature gradient

The peak concentrations of the neighbouring vibrational levels are, on average, separated in altitude by 0.5 km (von Savigny et al., 2012). Even though the absolute peak altitudes are known to vary with season (Gao et al., 2010), they can be taken as constant on the timescales of a few minutes over which this experiment was executed. With a steady-state OH model driven using a neutral atmosphere from the Naval Research Laboratory Mass Spectrometer and Incoherent Scatter Radar Empirical model (NRLMSISE) (Picone et al., 2002), the altitude of the (9,7) transition was fixed. The relative altitudes of the other vibrational transitions were then assigned using an altitude separation of 0.5 km, the average separation found by von Savigny et al. (2012). The rotational temperatures derived from each of the individual vibrational bands then provide an estimate of temperature gradients present similar to what has been done by Perminov et al. (2007) and Schubert et al. (1990).

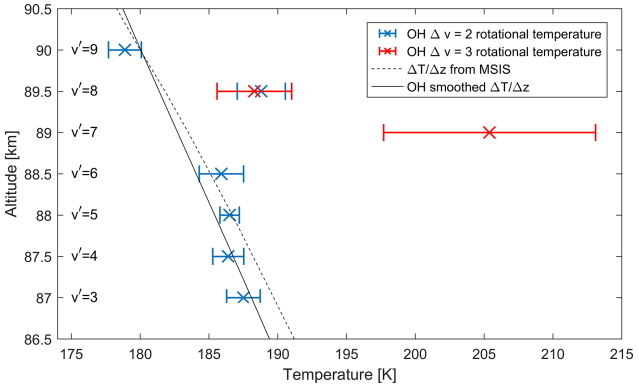

Figure 5. The temperatures from the data presented in Fig. 4 with $\Delta v = 2$ in blue and $\Delta v = 3$ in red. Both are presented with their 1σ error bar. The altitude of the (9, 7) transition was fixed with a steady-state model using a neutral atmosphere. The altitudes of the other transitions are fixed with a relative distance between neighbouring transitions of 0.5 km, following von Savigny et al. (2012). The NRLMSISE temperature gradient for 19 February 2013 at La Palma (17°53′ W, 28°45′ N) at 05:50 UT is shown as a dashed black line. The same gradient but smoothed with a modelled OH distribution in altitude is shown as a solid black line.

Figure 5 shows the distribution in altitude for the data presented here together with the NRLMSISE model kinetic temperature for the corresponding location and time. In addition, the NRLMSISE profile has been smoothed with the volume emission rate profile of an OH band derived from the steady-state OH model to reflect the effect of the OH layer width on the rotational temperatures. The temperature profile from this model is consistent with the gradients estimated from our data for the (3, 1), (4, 2), (5, 3), (6, 4), and (9, 7) transitions. It is important to note that the J-, H-, and K-band data shown in Fig. 5 were acquired using sequential 10.8 s observations, spanning only 6 min. Thus, large deviations from the

climatological gradients can occur due to wave activity (Xu et al., 2000). While the agreement here may be fortuitous, a time sequence of short integrations may give insight into the wave-induced temperature gradients.

While the (8, 6) transition is anomalously high, it was found that the P(2) and P(4) lines are partially absorbed by atmospheric H_2O and CO_2 (Jones et al., 2013; Noll et al., 2012). To model the impact of this atmospheric absorption, synthetic spectra with rotational temperatures between 130 and 300 K were created. When these were fitted with the technique described above, this input temperature could be retrieved. When these synthetic spectra were however first multiplied by a high-resolution (0.002 nm) absorption spectrum for seasonally averaged conditions obtained from the Cerro Paranal sky model (Jones et al., 2013; Noll et al., 2012), the fitted temperature was approximately 8% higher than the original synthesized temperature. This would account for the higher fitted temperature of the observed (8, 6) band shown in Fig. 5. Using this same technique, the temperatures for all other vibrational-rotational transitions presented in Fig. 5 were examined and found not to be significantly affected by atmospheric absorption.

With the intent of demonstrating that the NOTCam provides atmospheric data that can be used to supplement other astronomical data sets used for aeronomic studies (e.g. Osterbrock et al., 1996; Noll et al., 2015; Cosby and Slanger, 2007), a sample short-integration spectrum was analysed, and both the analysis procedure and the results are presented. With the exception of the weak or compromised $v' = 7$ and 8 levels discussed earlier, the temperature variation with vibrational level observed using the NOTCam and analysed here reflects the NRLMSISE kinetic temperature to within 2σ. This is consistent with previous observations using ground-based spectrometers or interferometers (e.g. Innis et al., 2001; Oberheide et al., 2006; French and Mulligan, 2010; Dyrland et al., 2010). However, it must be pointed out that the NOTCam measurements cover a very short time span and may be affected by gravity-wave perturbations of the climatological temperature gradient of the atmosphere represented by NRLMSISE. The temperature distribution with vibrational level observed here shows a small decrease toward higher levels, although this decrease is, apart from the $v' = 9$, not significant at the 2σ level. This is at odds with the measurements of Noll et al. (2015) and Cosby and Slanger (2007), who show strong increases in temperature with vibrational level that they attribute to non-thermodynamic equilibrium effects. However, our results are consistent with the results of Lübken et al. (1990), Espy and Hammond (1995), Wrasse et al. (2004), and Perminov et al. (2007), who show similar or decreasing temperatures with increasing vibrational level. Once again, the short duration of these demonstration data is not able to resolve this apparent discrepancy, but the larger NOTCam data set may prove useful in this regard.

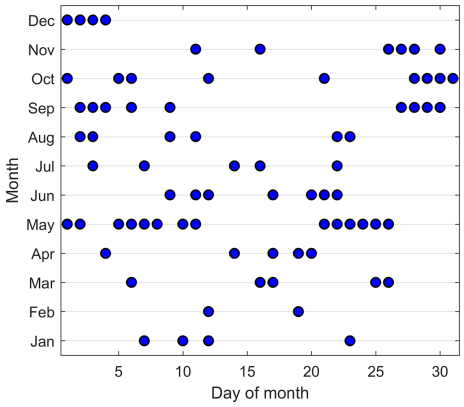

Figure 6. Dates between November 2007 and June 2016 (which is the coverage in the NOTCam archive) when the NOTCam was mounted at the NOT and making spectroscopic astronomical observations.

4 Outlook

Near-IR spectroscopy with NOTCam has been performed over the last 13 years toward point-like sources (stars or marginally extended objects). NOTCam, in both spectroscopic and imaging mode, was mounted and used on the telescope an average of 15 % of the observing time between 2003 and 2016, spread evenly throughout the calendar year. Thus, good seasonal coverage is available as indicated in Fig. 6, which shows the distribution of dates between November 2007 and June 2016 when the NOTCam was used for long-slit spectroscopic observations.

The spectroscopic mode has been continuous and stable with no change of optical elements, except for the addition of the two broadband filters, Z and Y, in 2010. There has been a change of detector, most recently in 2007, but each array is well characterized. All data older than 1 year (the proprietary period at the NOT) are available in the NOT data archive. Figure 7 shows histograms of the total number of spectroscopic observations taken in the J, H, and K bands for each hour, indicating nearly uniform coverage in each wavelength region.

With this data set, a variety of atmospheric problems can be addressed. One example is to simply generate climatological temperature gradients of the mesopause region from the long-term data as in Fig. 5. High-quality long-term observations of the mean state, trends, and inter-annual variability of this region are rare, especially at low latitudes, and can serve as an important standard against which whole atmosphere models can be validated.

Additionally, there is a long-standing discussion as to whether the vibrationally excited OH quenches to the ground state ("sudden death") or relaxes to the next-lowest vibrational level (McDade, 1991). Knowledge of the population and quenching of the individual upper states is essential for the interpretation of the OH airglow emission for remote

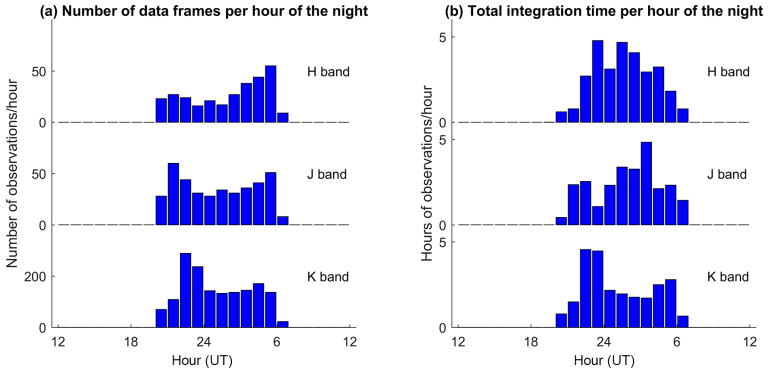

Figure 7. **(a)** Total number of spectroscopic data frames recorded in each hour and each band with NOTCam between November 2007 and June 2016. **(b)** Total hours of on-target integration time for spectroscopic data recorded in each hour and each band with the NOTCam in the same period of time.

sensing of the mesopause region. These high-quality data described above, together with a steady-state model, can be used to estimate the ratio of single to multi-quantum quenching efficiency accurately. Although these quenching rates have been examined by Xu et al. (2012) using broadband SABER measurements that combine multiple high-v' and low-v' levels, the individual bands resolved by astronomical telescopes would allow an unambiguous assessment of these rates.

The data discussed here have very short integration times as a demonstration of the worst-case conditions. This means that a series of measurements of the same spot of the sky can scan the OH layer with a repetition rate of down to 20 s. This lies well below the upper boundary of gravity waves (Kovalam et al., 2011) and stretches into the domain of acoustic and infrasonic waves. Although these waves have been observed in the hydroxyl airglow (Bittner et al., 2010; Pilger et al., 2013), the low spatial resolution of the observations creates ambiguity in their identification. Here the observations have a spatial resolution on the airglow layer of about 100 m (which is 4 arcmin), sampled with approximately 1000 pixels in the spatial direction of the NOT detector. This resolution is achieved with the telescope in "staring mode", which means without star tracking. The resolution with star tracking is dependent on the slit orientation and is in the worst case up to 6.7×2.7 arcmin over a 10.8 s integration. Using staring mode, the high resolution in both the temporal and spatial dimensions allows high-frequency waves to be measured at a commensurate spatial resolution. This opens up new possibilities to study the smallest structures of waves propagating through the OH layer in the MLT. While staring observations would recover the full spatial resolution of the instrument, care should be taken with the slit orientation and choice of direction to ensure that bright astronomical objects do not interfere with the airglow observations.

Finally, in parallel with the atmospheric work, it will be possible to quantify how the intensity of the mesospheric OH background in the astronomical H, J, and K bands varies on different timescales (from minutes to years) over La Palma. This will be useful in the planning and scheduling of observations in order to optimize dithering strategies and observing modes, especially important for instruments observing simultaneously at optical and infrared wavelengths.

Data availability. Archive data from the NOTCam can be accessed via http://www.not.iac.es/observing/forms/fitsarchive/ (Nordic Optical Telescope, 2017).

Competing interests. The authors declare that they have no conflict of interest.

Acknowledgements. This work was based on observations made with the Nordic Optical Telescope, operated by the Nordic Optical Telescope Scientific Association at the Observatorio del Roque de los Muchachos, La Palma, Spain, of the Instituto de Astrofisica de Canarias. We thank the staff from the NOT for their help and support during a visit by Christoph Franzen in November 2014. This work was supported by the Research Council of Norway/Centres of Excellence (CoE) under contract 223252/F50.

Edited by: Lars Hoffmann
Reviewed by: two anonymous referees

References

Abbott, T. M., Aspin, C., Sorensen, A. N., Norregaard, P., Andersen, J., Andersen, M. I., van der Bliek, N. S., Clasen, J. W., Cox, G. C., Klougart, J., Larsen, H. H., Michaelsen, N., Noel, B., Olofsson, G., Perez, C., and Schwarz, H. E.: SWIR at the Nordic Optical Telescope: NOTCam, in: Optical and IR Telescope Instrumentation and Detectors, Vol. 4008, edited by: Iye, M. and Moorwood, A. F., SPIE Proc., Munich, 2000.

Baker, D. J. and Stair Jr., A. T.: Rocket measurements of the altitude distributions of the hydroxyl airglow, Phys. Scripta, 37, 611–622, 1988.

Bittner, M., Höppner, K., Pilger, C., and Schmidt, C.: Mesopause temperature perturbations caused by infrasonic waves as a potential indicator for the detection of tsunamis and other geo-hazards, Nat. Hazards Earth Syst. Sci., 10, 1431–1442, https://doi.org/10.5194/nhess-10-1431-2010, 2010.

Brent, R. P.: Algorithms for Minimization Without Derivatives, Dover Publications, Mineola, NY, 1973.

Cosby, P. C. and Slanger, T. G.: OH spectroscopy and chemistry investigated with astronomical sky spectra, Can. J. Phys., 85, 77–99, 2007.

Djupvik, A. A.: http://www.not.iac.es/instruments/notcam/, last access: 10 August 2016.

Djupvik, A. A. and Andersen, J.: The Nordic Optical Telescope, in: Highlights of Spanish Astrophysics V, edited by: Diego, M. J., Goicoechea, J. L., González-Serrano, I. J., and Gorgas, J., Springer, Berlin, Heidelberg, 2010.

Dyrland, M. E., Mulligan, F. J., Hall, C. M., Sigernes, F., Tsutsumi, M., and Deehr, C. S.: Response of OH airglow temperatures to neutral air dynamics at 78° N, 16° E during the anomalous 2003–2004 winter, J. Geophys. Res.-Atmos., 115, 1–11, 2010.

Espy, P. J. and Hammond, M. R.: Atmospheric transmission coefficients for hydroxyl rotational lines used in rotational temperature determinations, J. Quant. Spectrosc. Ra., 54, 879–889, 1995.

Espy, P. J. and Stegman, J.: Trends and variability of mesospheric temperature at high-latitudes, Phys. Chem. Earth, 27, 543–553, 2002.

French, W. J. R. and Mulligan, F. J.: Stability of temperatures from TIMED/SABER v1.07 (2002–2009) and Aura/MLS v2.2 (2004–2009) compared with OH(6-2) temperatures observed at Davis Station, Antarctica, Atmos. Chem. Phys., 10, 11439–11446, https://doi.org/10.5194/acp-10-11439-2010, 2010.

Galassi, M. and Gough, B.: GNU Scientific Library Reference Manual, 3rd Edn., Network Theory Ltd, Godalming, UK, 2009.

Gao, H., Xu, J., and Wu, Q.: Seasonal and QBO variations in the OH nightglow emission observed by TIMED/SABER, J. Geophys. Res.-Space, 115, 1–13, 2010.

Innis, J. L., Phillips, F. A., Burns, G. B., Greet, P. A., French, W. J. R., and Dyson, P. L.: Mesospheric temperatures from observations of the hydroxyl (6–2) emission above Davis, Antarctica: A comparison of rotational and Doppler measurements, Ann. Geophys., 19, 359–365, https://doi.org/10.5194/angeo-19-359-2001, 2001.

Jones, A., Noll, S., Kausch, W., Szyszka, C., and Kimeswenger, S.: An advanced scattered moonlight model for Cerro Paranal, Astron. Astrophys., 560, 1–11, 2013.

Kovalam, S., Tsuda, T., and Gurubaran, S.: High-frequency gravity waves observed in the low-latitude mesosphere-lower thermosphere (MLT) region and their possible relationship to lower-atmospheric convection, J. Geophys. Res.-Atmos., 116, D15101, https://doi.org/10.1029/2011JD015625, 2011.

Lübken, F. J., von Zahn, U., Manson, A., Meek, C., Hoppe, U. P., Schmidlin, F. J., Stegman, J., Murtagh, D. P., Rüster, R., Schmidt, G., Widdel, H. U., and Espy, P.: Mean state densities, temperatures and winds during the MAC/SINE and MAC/EPSILON campaigns, J. Atmos. Terr. Phys., 52, 955–970, 1990.

McDade, I. C.: The altitude dependence of the OH(X2Π) vibrational distribution in the nightglow: Some model expectations, Planet. Space Sci., 39, 1049–1057, 1991.

Meinel, I. A. B.: OH Emission Bands in the Spectrum of the Night Sky. II, Astrophys. J., 112, 120–130, 1950.

Noll, S., Kausch, W., Barden, M., Jones, A. M., Szyszka, C., Kimeswenger, S., and Vinther, J.: An atmospheric radiation model for Cerro Paranal, Astron. Astrophys., 543, A92, 2012.

Noll, S., Kausch, W., Kimeswenger, S., Unterguggenberger, S., and Jones, A. M.: OH populations and temperatures from simultaneous spectroscopic observations of 25 bands, Atmos. Chem. Phys., 15, 3647–3669, https://doi.org/10.5194/acp-15-3647-2015, 2015.

Nordic Optical Telescope: The NOT FITS Header Archive, available at: http://www.not.iac.es/observing/forms/fitsarchive/, last access: 22 August 2017.

Oberheide, J., Offermann, D., Russell, J. M., and Mlynczak, M. G.: Intercomparison of kinetic temperature from 15 µm CO_2 limb emissions and $OH^*(3, 1)$ rotational temperature in nearly coincident air masses: SABER, GRIPS, Geophys. Res. Lett., 33, 1–5, 2006.

Osterbrock, D. E., Fulbright, J. P., Martel, A. R., Keane, M. J., Trager, S. C., and Basri, G.: Night-Sky High-Resolution Spectral Atlas of OH and O_2 Emission Lines for Echelle Spectrograph Wavelength Calibration, Publ. Astron. Soc. Pacific, 108, 277–308, 1996.

Pendleton, W. R., Espy, P. J., Baker, D. J., Steed, A., Fetrow, M. P., and Henriksen, E. K.: Observation of OH Meinel (7, 4) $P(N'' = 13)$ transitions in the night airglow, J. Geophys. Res.-Space, 94, 505–510, 1989.

Pendleton, W. R., Espy, P. J., and Hammond, M. R.: Evidence for non-local-thermodynamic-equilibrium in the OH nightglow, J. Geophys. Res., 98, 11567–11579, 1993.

Perminov, V. I., Semenov, A. I., and Shefov, N. N.: On rotational temperature of the hydroxyl emission, Geomagn. Aeron., 47, 756–763, 2007.

Picone, J. M., Hedin, A. E., Drob, D. P., and Aikin, A. C.: NRLMSISE-00 empirical model of the atmosphere: Statistical comparisons and scientific issues, J. Geophys. Res.-Space, 107, 1468, https://doi.org/10.1029/2002JA009430, 2002.

Pilger, C., Schmidt, C., Streicher, F., Wüst, S., and Bittner, M.: Airglow observations of orographic, volcanic and meteorological infrasound signatures, J. Atmos. Sol.-Terr. Phy., 104, 55–66, 2013.

Rothman, L. S., Gordon, I. E., Babikov, Y., Barbe, A., Chris Benner, D., Bernath, P. F., Birk, M., Bizzocchi, L., Boudon, V., Brown, L. R., Campargue, A., Chance, K., Cohen, E. A., Coudert, L. H., Devi, V. M., Drouin, B. J., Fayt, A., Flaud, J. M., Gamache, R. R., Harrison, J. J., Hartmann, J. M., Hill, C., Hodges, J. T., Jacquemart, D., Jolly, A., Lamouroux, J., Le Roy, R. J., Li, G., Long, D. A., Lyulin, O. M., Mackie, C. J., Massie, S. T., Mikhailenko, S., Müller, H. S. P., Naumenko, O. V., Nikitin, A. V., Orphal, J., Perevalov, V., Perrin, A., Polovtseva, E. R., Richard, C., Smith, M. A. H., Starikova, E., Sung, K., Tashkun, S., Tennyson, J., Toon, G. C., Tyuterev, V. G., and Wagner, G.: The HITRAN2012 molecular spectroscopic database, J. Quant. Spectrosc. Ra., 130, 4–50, 2013.

Schubert, G., Walterscheid, R. L., Hecht, J. H., and Sivjee, G. G.: Temperature gradients at mesopause heights inferred from OH nightglow data, J. Geophys. Res.-Space, 95, 19061–19067, 1990.

Sigernes, F., Shumilov, N., Deehr, C. S., Nielsen, K. P., Svenøe, T., and Havnes, O.: Hydroxyl rotational temperature record from the auroral station in Adventdalen, Svalbard, J. Geophys. Res.-Space, 108, 1342–1351, 2003.

Smith, A. K.: Global Dynamics of the MLT, Surv. Geophys., 33, 1177–1230, 2012.

Smith, A. K.: Physics and chemistry of the mesopause region, J. Atmos. Sol.-Terr. Phy., 66, 839–857, 2004.

Smith, S. M., Baumgardner, J., Mertens, C. J., Russell, J. M., Mlynczak, M. G., and Mendillo, M.: Mesospheric OH temperatures: Simultaneous ground-based and SABER OH measurements over Millstone Hill, Adv. Space Res., 45, 239–246, 2010.

Telting, J.: http://www.not.iac.es/instruments/notcam/spectroscopy/, last access: 10 August 2016.

Tody, D.: IRAF in the Nineties, Astronomical Data Analysis Software and Systems II, A. S. P. Conference Series, San Francisco, USA, 52, 173, 1993.

von Savigny, C., McDade, I. C., Eichmann, K.-U., and Burrows, J. P.: On the dependence of the OH^* Meinel emission altitude on vibrational level: SCIAMACHY observations and model simulations, Atmos. Chem. Phys., 12, 8813–8828, https://doi.org/10.5194/acp-12-8813-2012, 2012.

von Zahn, U., Fricke, K. H., Gerndt, R., and Blix, T.: Mesospheric temperatures and the OH layer height as derived from ground-based lidar and OH^* spectrometry, J. Atmos. Terr. Phys., 49, 863–869, 1987.

Wrasse, C. M., Takahashi, H., and Gobbi, D.: Comparison of the OH (8-3) and (6-2) band rotational temperature of the mesospheric airglow emissions, Rev. Bras. Geofis., 22, 223–231, 2004.

Xu, J., Gao, H., Smith, A. K., and Zhu, Y.: Using TIMED/SABER nightglow observations to investigate hydroxyl emission mechanisms in the mesopause region, J. Geophys. Res.-Atmos., 117, 1–22, 2012.

Xu, J., Smith, A. K., and Brasseur, G. P.: The effects of gravity waves on distributions of chemically active constituents in the mesopause region, J. Geophys. Res.-Atmos., 105, 26593–26602, 2000.

Yee, J.-H., Crowley, G., Roble, R. G., Skinner, W. R., Burrage, M. D., and Hays, P. B.: Global simulations and observations of O(1S), O_2(1Sigma) and OH mesospheric nightglow emissions, J. Geophys. Res.-Space, 102, 19949–19968, 1997.

Paper 2

Franzen, C., Espy, P. J., Hibbins, R. E., & Djupvik, A. A. (2018). Observation of Quasiperiodic Structures in the Hydroxyl Airglow on Scales Below 100 m. *Journal of Geophysical Research: Atmospheres, 123*(19), 10,935-910,942. doi:10.1029/2018JD028732

Journal of Geophysical Research: Atmospheres

RESEARCH ARTICLE
10.1029/2018JD028732

Observation of Quasiperiodic Structures in the Hydroxyl Airglow on Scales Below 100 m

Christoph Franzen[1,2], **Patrick Joseph Espy**[1,2], **Robert Edward Hibbins**[1,2], **and Anlaug Amanda Djupvik**[3]

[1]Department of Physics, Norwegian University of Science and Technology (NTNU), Trondheim, Norway, [2]Birkeland Centre for Space Science, Bergen, Norway, [3]Nordic Optical Telescope, Santa Cruz De La Palma, Spain

Key Points:
- A 2.5-m telescope at midlatitudes is employed for high-resolution observations of the OH layer
- Quasi periodic structures on scales between 60 and 4.5 m were observed
- Observed structures follow a Kolmogorov type model of turbulence with a −5/3 power law

Correspondence to:
C. Franzen,
christoph.franzen@ntnu.no

Citation:
Franzen, C., Espy, P. J., Hibbins, R. E., & Djupvik, A. A. (2018). Observation of quasi-periodic structures in the hydroxyl airglow on scales below 100 m. *Journal of Geophysical Research: Atmospheres*, *123*. https://doi.org/10.1029/2018JD028732

Received 28 MAR 2018
Accepted 21 SEP 2018
Accepted article online 24 SEP 2018

Abstract Gravity waves are known to transport energy and momentum to the middle atmosphere. The breaking processes associated with divergence of fluxes of energy and momentum into the atmosphere occur on scales that cannot be resolved in models and therefore have to be parameterized. The question remains as to whether it is possible to use a turbulence model on scales below 100 m and what kind of turbulence model should that be. Here we use high spatial resolution observations of the OH nightglow located near 90-km altitude from the Nordic Optical Telescope to observe quasiperiodic structures down to horizontal scales of 4.5 m. These results indicate that a Kolmogorov type of energy cascade model of turbulence with a −5/3 power law appears to be satisfied down to these short, 4.5-m scales.

1. Introduction

1.1. Gravity Wave Breaking

Gravity waves propagating upward from the lower atmosphere transport energy and momentum into the upper atmosphere. As they propagate upward their amplitudes grow to conserve energy as the background density decreases with altitude. Ultimately, wave-induced temperature gradients exceed the adiabatic lapse rate (Holton, 1982; Lindzen, 1981). When this occurs, the waves begin breaking, dissipating energy and depositing momentum into the surrounding atmosphere (Staquet & Sommeria, 2002). There are also other breaking mechanisms that can lead to instabilities, including self-accelerating instabilities (Fritts et al., 2015), wave-induced shears, or wind-induced critical levels, where the intrinsic wave speed approaches that of the wind (Fritts & Alexander, 2003). These breaking processes generally take place in the mesosphere and lower thermosphere (MLT), where this wave momentum drives the mean flow away from radiative equilibrium and produces a pole-to-pole meridional circulation in the MLT (Holton, 1983).

The intensity of the terrestrial airglow layer, produced at night by chemiluminescent reactions associated with the recombination of atomic species that have been photodissociated during the day, is modulated by the temperature and density perturbations associated with these gravity waves as they pass through the layer. The hydroxyl (OH) airglow near 90 km (Meinel, 1950a, 1950b) is one of the more intense emissions, and observations of the OH airglow are often employed to measure gravity waves and breaking features in the MLT region (Diettrich et al., 2005; Fritts et al., 2017; Li et al., 2005). Responding to a wide range of vertical wavelengths (Liu & Swenson, 2003; Swenson & Gardner, 1998), measurements of the horizontal wavelength of gravity waves have been made with OH airglow imagers (Sedlak et al., 2016; Taylor et al., 2007). Studies such as these typically detected atmospheric gravity waves in the OH airglow layer on scales of the order ~1 to hundreds of kilometers. Other studies (Dewan et al., 1992; Fritts et al., 2017; Hecht et al., 1997) have observed turbulent and wave-breaking features in the OH layer on scales larger than a kilometer and with frequencies up to 0.01 Hz.

During the breaking process, the waves do not instantaneously deposit all their energy. Rather smaller and smaller structures are created with ever increasing wave numbers in the process (Becker & Schmitz, 2002). These smaller-scale structures, including secondary waves and turbulence, can have a phase direction different from that of the primary wave (Fritts et al., 2017) and carry less energy. Kolmogorov (1941a, 1941b) described this cascade-breaking process with a simple diffusion model, where the energy cascades as a −5/3 power law with the wave number of the wave like structure. While some measurements of the OH airglow have observed such a −5/3 power law for kilometer-scale waves (Dewan et al., 1992; Hecht et al., 2005),

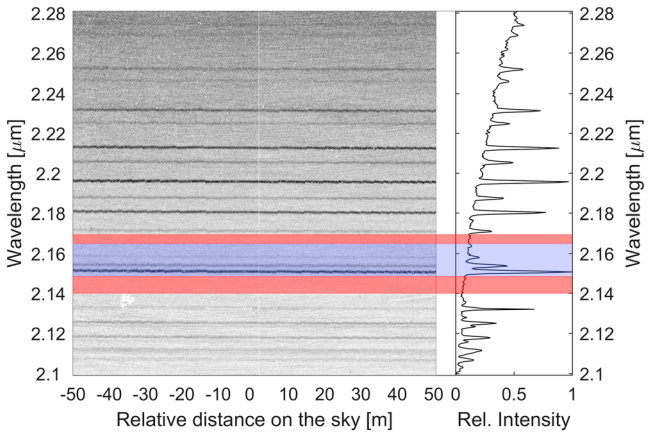

Figure 1. Example of one integration from May 2016. The integration time is 20 s. Only the (9,7) transition is shown with P, Q, and R branch from top to bottom. The left side shows the spatially resolved picture along the slit over 100 m of sky at the OH layers' mean altitude. The right side shows the accumulated spectrum over the whole slit. The blue area marks the Q branch, while the red areas mark pure background noise areas on both sides of the Q branch.

it is unclear whether this turbulence model can be assumed at the smallest, parameterized scales below 100 m to characterize this energy transfer.

In this paper we will present measurements on the OH airglow Q branch of the (9,7) transition at 2,100 nm to 2,250 nm. These measurements have been made using the NOTCam spectrograph mounted on the Nordic Optical Telescope (NOT) in La Palma. The high throughput of the system coupled with its high temporal resolution (~10 s) affords the opportunity to utilize the high spatial resolution along the slit (10 cm/pixel) to measure quasiperiodic structures (QPS) in the OH with horizontal wavelengths below 100 m. The energy cascade of these small-scale structures complements previous studies at larger scales and adds to a further understanding of the energy deposition of gravity waves in the MLT.

1.2. Instrumentation and Data

The measurements presented in this paper were taken with the NOT. The NOT is part of the Spanish Observatorio del Roque de los Muchachos, situated in La Palma, Canary Islands, Spain (17°53′ W, 28°45′N). The telescope has an f/2 primary mirror with a diameter of 2,560 mm (Djupvik & Andersen, 2010). The spectroscopic instrument used here is the NOT near-infrared Camera and spectrograph (NOTCam). The detector is a 1,024 × 1,024 pixel Rockwell Science Center HgCdTe "HAWAII" array. The slit size is 50 mm by 0.128 mm, with a field of view of 4 arc min by 0.6 arcsec. Taking the altitude of the OH layer to be 87 km (Baker & Stair, 1988), this projects to a spatial area of 100 by 0.25 m on the OH airglow. Therefore, effects across the slit width are neglected in this work. The filter used here is a K′ bandpass filter for wavelengths between 1,950 nm and 2,290 nm. Both the (9,7) and the (8,6) transitions can be found in this wavelength region. The resolving power used, $R = \lambda/\Delta\lambda \sim 2,100$, is sufficient to separate the R, Q, and P branches, as well as to resolve or partially resolve the individual rotational lines in each branch, as shown in Figure 1.

Data were obtained for two, approximately 1-hr-long observing periods on both 21 May 2016 and 20 June 2016 without automated star tracking. Instead, the telescope was pointed to the zenith in a staring mode and away from the galactic plane with the slit length orientated perpendicular to the apparent movement of the stars in the sky. That is, the slit was oriented on the north-south axis. In this orientation, stars pass through the 0.6 arcsec field of view of the slit width in 0.04 s, minimizing their effects on the background. For each hour of observation, spectra were recorded using an integration time of 20 s (21 May) or 10.8 s (20 June). After each integration there was a dead time of about 12 s during which time the detector was read out. Table 1 below summarizes the observations.

Figure 1 below is a typical example of a single 20-s integration recorded during May that shows only the (9,7) transition of OH and describes the techniques used to process the data. The basic data processing for telescope data of the OH is described in Franzen et al. (2017). Briefly, the effects of the known bad pixels on the detector and the curvature of the image due to focal plane orientation were corrected. Similarly, a dark image was used to remove detector background, and the relative spectral sensitivity was corrected using a 3200 K deuterium lamp as a flat field calibrator right before or after the observations.

Shown on the left side of the figure is the detector image with the horizontal axis showing distance along the slit length, mapped to the nominal 87-km altitude of the OH layer (Baker & Stair, 1988). The vertical axis is the spectral axis labeled in wavelength. The image grayscale is inverted, and the individual OH spectral lines in emission are therefore seen as the black horizontal lines in the image.

On the right side of Figure 1, the spectrum is integrated along the horizontal, slit-length axis to show the total intensity as a function of wavelength. The spectrum is presented in uncorrected relative intensity for simplicity.

Table 1
Technical Details of the Observations

Date of observation	21 May 2016	20 June 2016
Integration time (s)	20	10.8
Repetition time (s)	32	24
# of integrations	133	167
Total time (min)	71	67
Time (UT)	22:07–23:18	22:23–23:30

Note. Shown are the dates of the observation, the integration times, the total repetition time between each two integrations (integration time plus read-out time), the total number of integrations executed, and the total time of the whole observation, as well as the UT time of the observations.

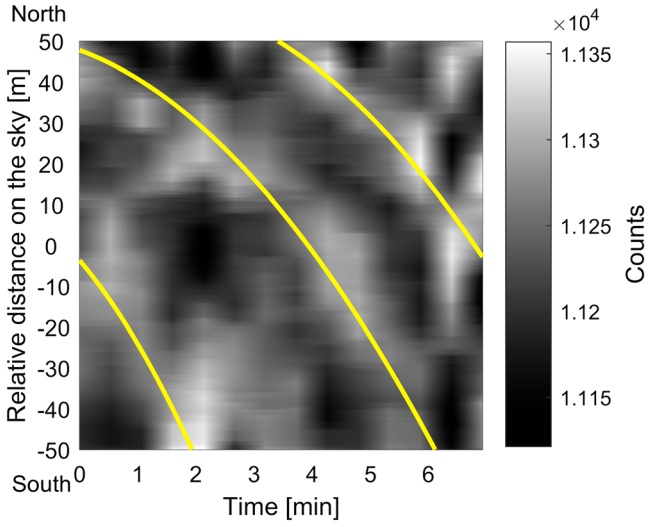

Figure 2. Example keogram of a quasiperiodic structures (QPS) event across 100 m of sky. The display lasted from minute 31 to minute 38 of the observation from 21 May 2016. The integration time per time step is 20 s. Three QPS crests are visible over the course of about 7 min, moving to the right of the picture. The QPS crests' positions are highlighted in yellow by a polynomial fit of second order through the maximum values along the three crests. The observed wavelength is around 30–40 m. The intensity color scale is in counts.

The blue area marks the Q branch in the center of the (9,7) transition. The two red areas on either side mark areas of background noise free of OH lines. The P branch can be seen at longer wavelengths, while the R branch is visible at shorter wavelengths.

2. Method

The spectrum on the right side of Figure 1 shows the sum over all 1,024 pixels along the slit of the telescope. However, each column of pixels from the left side of Figure 1 shows the spectrum for each 10-cm-wide position on the sky along the slit length. A variation across the observed 100 m of sky will therefore be visible as a change in the intensity of the spectrum between these columns.

There is an underlying background in the spectra presented in Figure 1 that is obvious in the integrated spectrum on the right. To remove this, the background level on either side of the Q branch is measured, and the background below the lines of the Q branch is approximated by linear interpolation and then subtracted. Then, the signal across the Q branch from 2,148.5 to 2,165 nm is integrated for each column to obtain the total intensity of this branch, independent of the rotational temperature, for each spatial element along the slit length. A 10-pixel median filter, which represents 1 m at the OH altitude, is applied to the integrated Q branch along the slit columns to increase the signal-to-noise ratio and avoid aliasing in the subsequent analysis.

This procedure is employed on each 10- or 20-s data sample, yielding the time evolution of the Q branch intensity at every spatial location along the slit. The temporal sequence is combined to form a keogram (Eather et al., 1976), an example of which is presented in Figure 2. The figure shows the intensity along the slit for each time along the horizontal axis with intensities shown by the color scale. Three bright lines of high intensities (highlighted in the figure by a simple polynomial fit of second order through the maximum values of each of the three crests) are visible, indicating three QPS crests moving to the south over the course of 7 minutes. The wavelength of the QPS shown is about 30–40 m, with small variations. If the orientation of the structure is at an angle φ relative to the slit direction, this wavelength would be longer by a factor 1/ cos φ than its true wavelength. A discussion of the implications of this projected wavelength compared to the real wavelength will be given later in the paper.

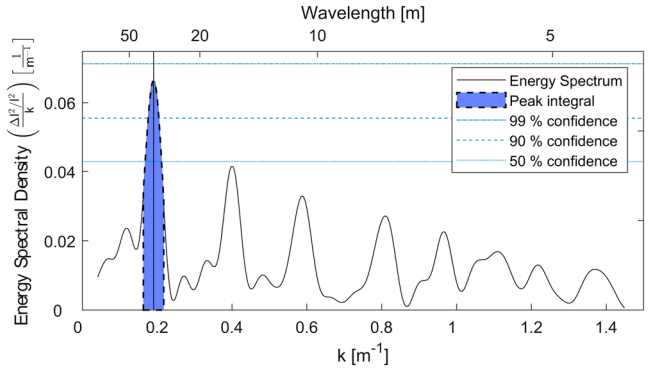

Figure 3. Lomb-Scargle periodogram of one time step from around the middle of the example event presented in Figure 2. The clear peak around the wave number 0.19 m^{-1} (corresponding to a 33-m horizontal wavelength) is marked by the black vertical line. The integral over the peak is shown in blue. Other, smaller peaks show events whose durations were less than one Brunt period and are therefore not counted as an event. The blue horizontal lines show the lines of 50%, 90%, and 99% confidence in dotted, dashed, and dash-dotted, respectively.

In order to quantitatively extract even weak structures and their temporal duration, we present a method based the work of Humberset et al. (2017). As detailed below, the method uses a Fourier-based technique to separate the spatial frequencies present and a correlation between the temporal samples to determine their duration. The example of QPS presented here in Figure 2 will serve as the example through the steps of the procedure.

We employ a Lomb-Scargle algorithm (Lomb, 1976; Scargle, 1982) along the slit length, which yields the energy spectral density per spatial-frequency interval at each temporal sample. As an example, a time step from the middle (at about 4.3 min into the keogram presented in Figure 2) is used as input data to the Lomb-Scargle algorithm. The resulting energy spectral density is shown in Figure 3. If random noise in the data has a probability, p_o, of creating a spectral estimate of amplitude. z_o, then the level of confidence, $(1 - p_o)$, with which one can eliminate the hypothesis that random noise in the data created a spectral amplitude z_o is given by

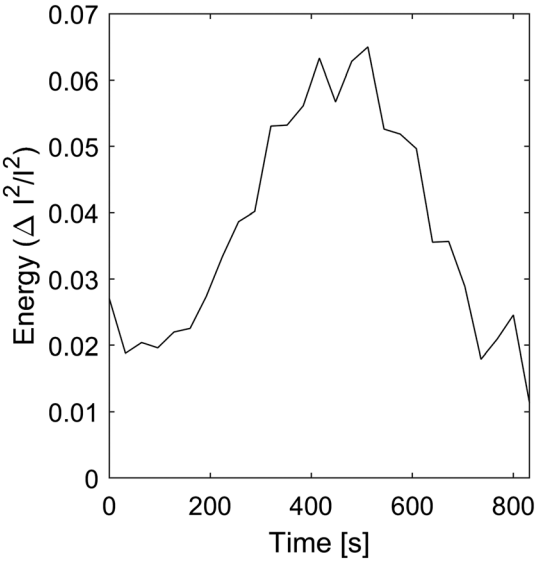

Figure 4. Temporal evolution of the energy of the QPS (spectral density integrated over the full width at half maximum wave number bin between 0.16 m^{-1} and 0.22 m^{-1}) for the data presented in Figure 2. This shows the fluctuation to be an isolated event, with a duration of approximately 600 s.

$$z_0 = -\ln\left[1-(1-p_0)^{\frac{1}{N}}\right],$$

where N is the number of data points (Scargle (1982). The blue horizontal lines in Figure 3 represent the spectral amplitudes where random noise can be excluded as the source with 50%, 90%, and 99% confidence, shown as dotted, dashed, and dash-dotted lines, respectively. The highest peak in the spectrum, significant above the 90% confidence level, appears at radial wave number $k = 2{\cdot}\pi/\lambda = 0.19$ m^{-1} (or 33 m wavelength). This corresponds to the approximate distance between QPS crests that can be seen in Figure 2. The relative energy in the peak is taken to be the integral over the peak's full width at half maximum, 0.06 m^{-1}, which is set by the total distance spanned by the slit length.

This integral over the peak is executed for the Lomb-Scargle periodogram of each individual time sample. Regions of significant (at the 50% confidence level) energy spectral density at wavelengths that are coherent over time indicate an event rather than random fluctuations. While a 50% confidence level on an individual spectrum is relatively low but tolerable (Vetterling et al., 1992), we require a peak to be above the 50% level over at least a full Brunt period. This means that the peak would occur at or above the 50% confidence level at least 10 times in a row, allowing one to say that at the 99.9% confidence level, random noise in the data is not responsible for this peak.

For example, for the data presented in Figures 2 and 3, the temporal evolution of the energy (the spectral density integrated over the full width at half maximum wave number bin between 0.16 m^{-1} and 0.22 m^{-1}) is shown in Figure 4. The data in the Figure have been smoothed with a 1.5-min running median filter, and the event is visible for a duration of about 600 s.

To determine which events show coherent behavior in time and to get a consistent, quantitative measure of the length of the event, we use the autocorrelation function of the temporal evolution of energy shown in Figure 4. An event with constant energy with abrupt starting and ending times would have a triangular lagged-autocorrelation function centered at zero lag with a maximum value of 1. The lag at which the autocorrelation passes 0.5 in the positive and negative directions represents the length of the event.

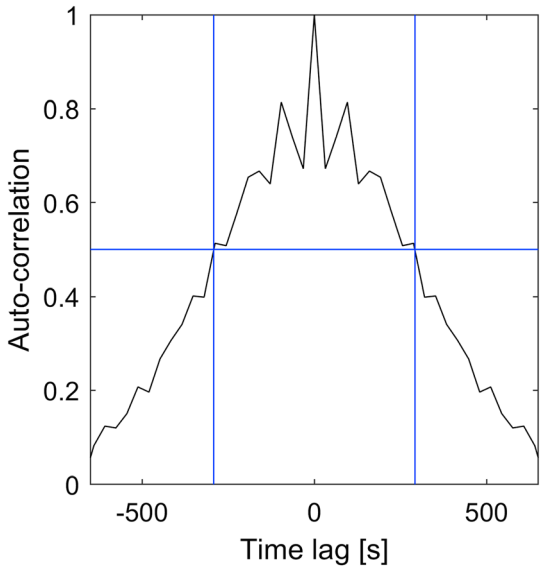

Figure 5. Lagged autocorrelation of the data presented in Figure 2 in the integrated spectral density bin between 0.16 m^{-1} and 0.22 m^{-1}. The point of 0.5 correlation is highlighted with blue lines for both positive and negative lags. The lag at these points is ±288 s, which yields an event length of 576 s. This is consistent with the qualitative evaluation from Figure 4.

Figure 5 shows the autocorrelation of the example data discussed above. The triangular structure is clearly visible and the points measured at a correlation greater than 0.5 yield an event length of 576 s, which agrees with the qualitative observation in Figure 4 of about 600 s. Events with a duration shorter than one Brunt period, which is roughly 300 s for the atmospheric conditions during the experiments presented here, are attributed to noise.

To treat the entire data set, a Lomb-Scargle periodogram is created for the spatial distribution along the slit length, as described above, for each temporal sample during the night. For each of these resulting periodograms, the wave numbers of peaks with significance ≥50% level, as well as their corresponding energies (the integral over the full width at half maximum) and time, are recorded. Taking each peak separately, the time sample when a significant peak first occurs is taken as the starting point, and the time series of energy versus time at that peak position is formed for all consecutive time samples, where the peak remains significant at ≥50% level. The resulting time series of energy is then autocorrelated as shown on the example in Figure 5. A peak whose energy autocorrelation

consistently remains above 0.5 for a duration longer than a Brunt period is taken to be a QPS. The process is repeated for all peaks found to be significant at ≥50% level.

While QPS may occur with durations shorter than a Brunt period, we have limited our analysis to events with duration of at least one period. This corresponds to about 300 s for the atmospheric conditions during our observations, and requires the peak in the power spectrum to be at the 50% significance level in at least 10 consecutive scans. The choice of 50% as the minimum criterion for significance in a single periodogram allows us to exclude random noise as the cause of the peak at an overall confidence level of 99.9%. However, this does not imply that QPS of duration shorter than one whole Brunt period may not occur.

3. Results and Discussion

We employ the method presented in the previous section on the observations from both nights. The first observation from 21 May yields 22 consistent QPS events. The second observation from 20 June yields 20 events. Together these 42 QPS events cover a time span of about 140 min. All the events span the wave number range from 0.11 m^{-1} (a 60 m wavelength) to 1.39 m^{-1} (4.5 m wavelength), which substantially expands the range of QPS features that have been observed in the OH airglow.

Figure 6 below gives an overview over the 42 QPS events found. Figure 6a presents the events for the observations from 21 May 2016, while Figure 6b shows the results for the observations from 20 June 2016. Each box represents one event, with the horizontal length showing the timespan over which the QPS could be observed. The QPS events range between 300 and 1,100-s length, with an average of 490 s. The vertical width of the box shows the full width at half maximum of the observed wave number peak from the Lomb-Scargle periodogram. The wavelengths corresponding to the wave numbers are indicated on the axis on the right-hand side. The darkness of the box indicates the relative energy of the event. A darker shade of gray represents a higher energy. It is apparent that events at smaller wave numbers have higher energy than those at larger wave numbers.

Figure 7 shows a log-log plot of the relative energy (in $\Delta I^2/I^2$) versus observed wave number for the events from the two nights of observations shown in Figure 6. The linear trend on the log-log plot indicates a power law relation between energy and wave number. The red line shows a power law fit that yields an exponent of -1.62 ± 0.08, with a correlation coefficient of -0.95. This value agrees to within one sigma with the $-5/3$ relation that would be expected from a Kolmogorov model of turbulent cascade (Kolmogorov, 1941a, 1941b). This suggests that the relationship holds for the QPS fluctuations found in the OH layer with wave numbers between 0.11 m^{-1} and 1.39 m^{-1} (wavelengths between 60 and 4.5 m). Previous workers (Cot, 2001; Dewan et al., 1992; Hecht et al., 1994) have found similar exponential relationships between QPS energy and wave number for QPS with kilometer scales. The results presented here suggest that the energy decay during breaking continues down to wave numbers as small as 1.39 m^{-1} (4.5 m wavelength), indicating that a Kolmogorov type model can be used to describe the turbulent cascade of energy in the MLT down to meter scales.

While the energy and the wave number show a clear correlation, the duration of the events is not correlated to either the energy or the wave number. That means that longer duration events show no tendency to have more or less energy than shorter ones, and that QPS events with higher wave numbers have no tendency to last longer or shorter than waves with smaller wave numbers.

The observations presented here, as with any measurement, have their own biases. For one, we observe only QPS with a well-defined wavelength structure and not random turbulent fluctuations. For another, we observe these structures in the horizontal, not the vertical. Finally, we have no altitude information as to where in the OH layer these structures may occur. Rocket observations near 90 km of the continuum of turbulent fluctuations in the vertical have reported the break to the dissipative region between 10 and 40 m (Hillert et al., 1994; Lübken, 1992; Lübken et al., 1994, 2002; Müllemann et al., 2002; Thrane et al., 1994). Although we observe individual structures with well-defined wavelengths at shorter scales, we would expect the break toward the dissipative region at smaller scales if the structures were occurring at the bottom side of the OH layer at lower altitudes (Lübken, 1992). Similarly, are we not aware of similar studies for horizontal observations, or for short-scale structures with a well-defined wavelength as presented in this paper. Observational biases in the two techniques, as well as the fact that we are not observing the same

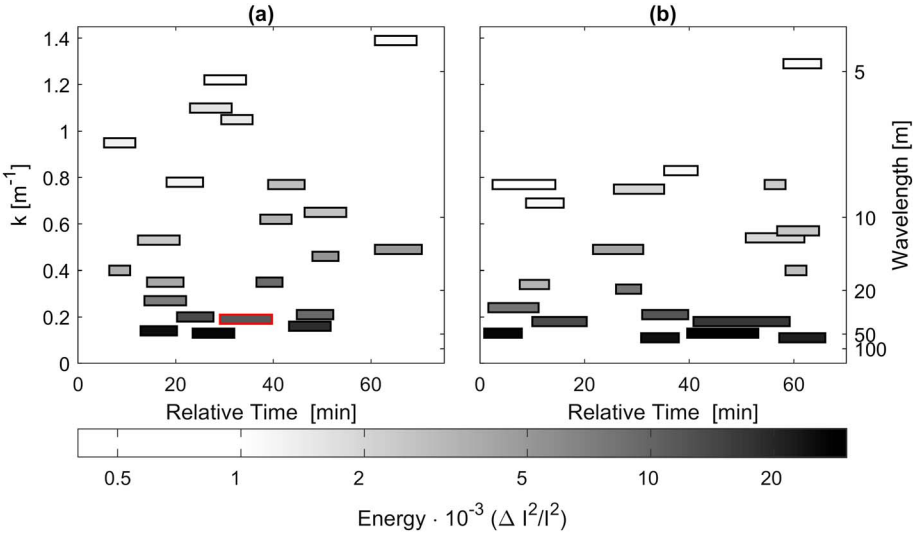

Figure 6. Overview over the 42 quasiperiodic structure (QPS) events detected at their observed wave numbers (wavelengths) and their durations in time. The wave number shown is that projected onto the slit direction. The darkness of each box indicates the energy of the QPS perturbation, with darker shades indicating higher energy. The highest wave number observed during the two nights is 1.39 m^{-1}, which corresponds to a wavelength of 4.5 m. (a) Observations from 21 May 2016. The QPS event from Figure 2 is highlighted in red. (b) Observation from 20 June 2016.

phenomena (random turbulence in the vertical vs. horizontal periodic structures) may account for this apparent discrepancy.

In order to examine whether detector effects could influence the results, we repeated the analysis procedure on the P branch of the OH (9,7) band. The P branch is spread over a wider range of wavelengths as can be seen in Figure 1. As a consequence the P branch is more vulnerable to any leftover detector effects. We again subtracted a linear interpolation of the background. Lines up to $N = 8$ used as higher rotational lines were cut off by the filter. The events presented in Figures 6 and 7 were found in the P branch as well, after employing the same reduction steps as for the Q branch. Small changes within the statistical noise limits were found in the length, the precise wave number, and the relative energy, and the slope of the energy cascade agreed with that found for the Q branch to within one sigma standard deviation.

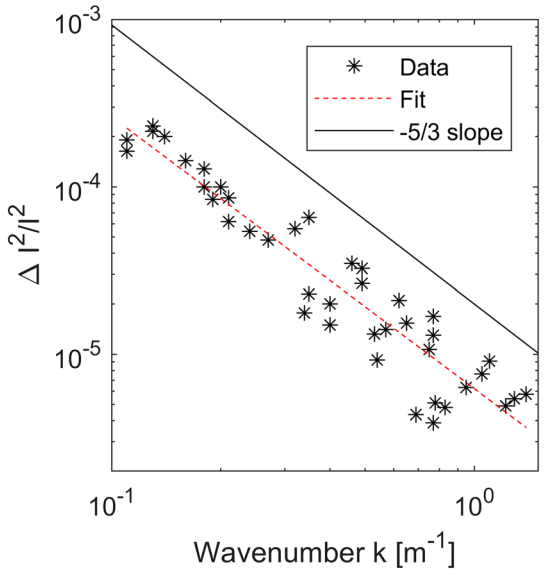

Figure 7. Logarithmic plot of the relative energy in $\Delta I^2/I^2$ versus the wave number of the 42 observed events (stars). A clear correlation of −0.95 is measured. The power-law fit (red, dashed line) yields an exponent of −1.62 ± 0.08. This suggests that quasiperiodic structures up to a wave number of 1.39 m^{-1} follow the dissipative process of the Kolmogorov cascade model during breaking (shown as a black solid line parallel to the data).

To further test that no stray detector signals caused variations along the slit length that would be interpreted as QPS events, the same procedure was repeated for areas between the OH lines where there was no airglow signal. Again, a background on either side was linearly interpolated over the *signal* region and the analysis carried out as described above. With no airglow signal present, no QPS event longer than the Brunt period could be detected. These two tests demonstrate that the results presented above are very small-scale, QPS in the OH airglow and not the result of random fluctuations or localized detector effects.

Finally, we note that the fact that we observe these QPS features implies that either wind speeds are small or the features are not locked to the wind. The latter would be true for turbulent features associated with gravity wave breaking that move with the phase of the parent wave rather than the background wind (Fritts et al., 2003). Thus, depending upon the ground propagation speed of the wave, small-scale structures could remain within the field of view of the telescope for times long enough to be observed. An extreme example would be a breaking mountain wave, where its associated instability structures would be relatively stationary to a ground-based observer.

A number of simulations were executed using synthetic data of QPS events with added white noise to verify that the procedure could retrieve wave numbers and energies correctly. This test was executed and recovered the input results for noise levels up to twice those found in the data.

To examine whether sampling the field in one direction distorted the energy spectrum, a number of QPS events with energy and wave number pairs following a Kolmogorov-like −5/3 power law were generated with random orientation angles, φ, relative to the slit direction. These were then projected onto the slit, lengthening the wavelengths by a factor of 1/ cos φ. The resulting data were fitted with a power law, as the data presented in Figure 7 above. The resulting exponent in the statistical mean over many simulations is -1.58 ± 0.08 which is within the standard deviation of the measurements presented here and the predicted value of −5/3 (−1.67) from the Kolmogorov law. We therefore infer that projecting the wave onto the slit direction does not change the result or our interpretation.

To demonstrate that the projection of the wave onto the slit does not artificially create a power law of −5/3, we generated QPS events with completely randomized energies and wave numbers lying in the range of observable energies and wave number of the instrument. We then projected these onto the slit direction and repeated the fit as presented in Figure 7. The resulting energy spectrum shows no correlation or significant relationship between energy and wave number. This indicates that the projection of the waves onto the slit direction cannot artificially create a Kolmogorov-like power law.

4. Conclusion

Three hundred spectra of the (9,7) OH vibrational transition were taken during two nights in May and June 2016 with the NOT in La Palma. The temperature-independent total intensity of the Q branch was calculated for each spectrum. Variations in OH airglow intensity along the slit of the camera showed QPS patterns. The wave numbers and energies of these QPS events were found employing a Lomb-Scargle periodogram. QPS features with wave numbers up to 1.39 m^{-1} could be observed. This wave number corresponds to a wavelength of about 4.5 m.

The consistency over time and the duration of the events were tested and calculated with an autocorrelation function test. The logarithm of the energies and corresponding wave numbers of the QPS events showed a very strong anticorrelation of −0.95. A least squares fit showed that the two quantities are connected via a power law with an exponent of -1.62 ± 0.08. This result lies within one sigma of the standard deviation with the predicted value of a Kolmogorov type model. This correspondence indicates that QPS down to scales of 4.5 m horizontal wavelength follow a Kolmogorov-type energy cascade during breaking and that this type of energy cascade model can be used to characterize scales down to 4.5 m in atmospheric gravity wave models.

These results were tested by using the intensity of the P branch instead of the Q branch, which yielded the same results within one sigma standard deviation. However, no QPS longer than at least one Brunt period could be found when employing the method presented here on a spectral area without OH airglow lines. This verifies that the QPS features observed were due to the OH airglow and not associated with position on the detector or stray detector signals.

Acknowledgments
This work was based on observations made with the Nordic Optical Telescope, operated by the Nordic Optical Telescope Scientific Association at the Observatorio del Roque de los Muchachos, La Palma, Spain of the Instituto de Astrofisica de Canarias. We thank the staff from the NOT for their help and support during a visit by C. F. in November 2016. This work was supported by the Research Council of Norway/CoE under contract 223252/F50. Archive data from the NOTCam can be accessed via http://www.not.iac.es/observing/forms/fitsarchive/ (Nordic Optical Telescope, 2017).

References

Baker, D. J., & Stair, J. A. T. (1988). Rocket measurements of the altitude distributions of the hydroxyl airglow. *Physica Scripta*, *37*(4), 611–622. https://doi.org/10.1088/0031-8949/37/4/021

Becker, E., & Schmitz, G. (2002). Energy deposition and turbulent dissipation owing to gravity waves in the mesosphere. *Journal of the Atmospheric Sciences*, *59*(1), 54–68. https://doi.org/10.1175/1520-0469(2002)059<0054:edatdo>2.0.co;2

Cot, C. (2001). Equatorial mesoscale wind and temperature fluctuations in the lower atmosphere. *Journal of Geophysical Research*, *106*(D2), 1523–1532. https://doi.org/10.1029/2000JD900597

Dewan, E. M., Pendleton, W., Grossbard, N., & Espy, P. (1992). Mesospheric OH airglow temperature fluctuations: A spectral analysis. *Geophysical Research Letters*, *19*(6), 597–600. https://doi.org/10.1029/92GL00391

Dietrich, J. C., Nott, G. J., Espy, P. J., Swenson, G. R., Chu, X., Taylor, M. J., et al. (2005). High frequency atmospheric gravity-wave properties using Fe-lidar and OH-imager observations. *Geophysical Research Letters*, *32*, L09801. https://doi.org/10.1029/2004GL021944

Djupvik, A. A., & Andersen, J. (2010). The Nordic Optical Telescope. In M. J. Diego, J. L. Goicoechea, I. J. González-Serrano, & J. Gorgas (Eds.), *Highlights of Spanish astrophysics V* (pp. 211–218). Berlin, Heidelberg: Springer.

Eather, R. H., Mende, S. B., & Judge, R. J. R. (1976). Plasma injection at synchronous orbit and spatial and temporal Auroral morphology. *Journal of Geophysical Research*, *81*(16), 2805–2824. https://doi.org/10.1029/JA081i016p02805

Franzen, C., Hibbins, R. E., Espy, P. J., & Djupvik, A. A. (2017). Optimizing hydroxyl airglow retrievals from long-slit astronomical spectroscopic observations. *Atmospheric Measurement Techniques*, *10*(8), 3093–3101. https://doi.org/10.5194/amt-10-3093-2017

Fritts, D. C., & Alexander, M. J. (2003). Gravity wave dynamics and effects in the middle atmosphere. *Reviews of Geophysics*, *41*(1), 1003. https://doi.org/10.1029/2001RG000106

Fritts, D. C., Bizon, C., Werne, J. A., & Meyer, C. K. (2003). Layering accompanying turbulence generation due to shear instability and gravity-wave breaking. *Journal of Geophysical Research*, *108*(D8), 8452. https://doi.org/10.1029/2002JD002406

Fritts, D. C., Laughman, B., Lund, T. S., & Snively, J. B. (2015). Self-acceleration and instability of gravity wave packets: 1. Effects of temporal localization. *Journal of Geophysical Research: Atmospheres*, *120*, 8783–8803. https://doi.org/10.1002/2015JD023363

Fritts, D. C., Wang, L., Baumgarten, G., Miller, A. D., Geller, M. A., Jones, G., et al. (2017). High-resolution observations and modeling of turbulence sources, structures, and intensities in the upper mesosphere. *Journal of Atmospheric and Solar-Terrestrial Physics*, *162*(Supplement C), 57–78. https://doi.org/10.1016/j.jastp.2016.11.006

Hecht, J. H., Liu, A. Z., Walterscheid, R. L., & Rudy, R. J. (2005). Maui mesosphere and lower thermosphere (Maui MALT) observations of the evolution of Kelvin-Helmholtz billows formed near 86 km altitude. *Journal of Geophysical Research*, *110*, D22S10. https://doi.org/10.1029/2003JD003908

Hecht, J. H., Walterscheid, R. L., Fritts, D. C., Isler, J. R., Senft, D. C., Gardner, C. S., et al. (1997). Wave breaking signatures in OH airglow and sodium densities and temperatures: 1. Airglow imaging, Na lidar, and MF radar observations. *Journal of Geophysical Research*, *102*(D6), 6655–6668. https://doi.org/10.1029/96JD02619

Hecht, J. H., Walterscheid, R. L., & Ross, M. N. (1994). First measurements of the two-dimensional horizontal wave number spectrum from CCD images of the nightglow. *Journal of Geophysical Research*, *99*(A6), 11,449–11,460. https://doi.org/10.1029/94JA00584

Hillert, W., Lübken, F. J., & Lehmacher, G. (1994). TOTAL: A rocket-borne instrument for high resolution measurements of neutral air turbulence during DYANA. *Journal of Atmospheric and Terrestrial Physics*, *56*(13-14), 1835–1852. https://doi.org/10.1016/0021-9169(94)90013-2

Holton, J. R. (1982). The role of gravity wave induced drag and diffusion in the momentum budget of the mesosphere. *Journal of the Atmospheric Sciences*, *39*(4), 791–799. https://doi.org/10.1175/1520-0469(1982)039<0791:trogwi>2.0.co;2

Holton, J. R. (1983). The influence of gravity wave breaking on the general circulation of the middle atmosphere. *Journal of the Atmospheric Sciences*, *40*(10), 2497–2507. https://doi.org/10.1175/1520-0469(1983)040<2497:tiogwb>2.0.co;2

Humberset, B. K., Gjerloev, J. W., Samara, M., & Michell, R. G. (2017). Scale size-dependent characteristics of the nightside aurora. *Journal of Geophysical Research: Space Physics*, *122*, 147–158. https://doi.org/10.1002/2016JA023695

Kolmogorov, A. N. (1941a). Local structure of turbulence in an incompressible fluid for very large Reynolds numbers. *Comptes rendus (Doklady) de l'Academie des Sciences de l'U.R.S.S.*, *31*, 301–305.

Kolmogorov, A. N. (1941b). On the degeneration of isotropic turbulence in an incompressible viscous fluid. *Comptes rendus (Doklady) de l'Academie des Sciences de l'U.R.S.S.*, *31*, 538–540.

Li, F., Liu, A. Z., Swenson, G. R., Hecht, J. H., & Robinson, W. A. (2005). Observations of gravity wave breakdown into ripples associated with dynamical instabilities. *Journal of Geophysical Research*, *110*, D09S11. https://doi.org/10.1029/2004JD004849

Lindzen, R. S. (1981). Turbulence and stress owing to gravity wave and tidal breakdown. *Journal of Geophysical Research*, *86*(C10), 9707–9714. https://doi.org/10.1029/JC086iC10p09707

Liu, A. Z., & Swenson, G. R. (2003). A modeling study of O_2 and OH airglow perturbations induced by atmospheric gravity waves. *Journal of Geophysical Research*, *108*(D4), 4151. https://doi.org/10.1029/2002JD002474

Lomb, N. R. (1976). Least-squares frequency analysis of unequally spaced data. *Astrophysics and Space Science*, *39*(2), 447–462. https://doi.org/10.1007/bf00648343

Lübken, F. J. (1992). On the extraction of turbulent parameters from atmospheric density fluctuations. *Journal of Geophysical Research*, *97*(D18), 20,385–20,395. https://doi.org/10.1029/92JD01916

Lübken, F. J., Hillert, W., Lehmacher, G., von Zahn, U., Blix, T. A., Thrane, E. V., et al. (1994). Morphology and sources of turbulence in the mesosphere during DYANA. *Journal of Atmospheric and Terrestrial Physics*, *56*(13-14), 1809–1833. https://doi.org/10.1016/0021-9169(94)90012-4

Lübken, F. J., Rapp, M., & Hoffmann, P. (2002). Neutral air turbulence and temperatures in the vicinity of polar mesosphere summer echoes. *Journal of Geophysical Research*, *107*(D15), 4273. https://doi.org/10.1029/2001JD000915

Meinel, A. B. (1950a). OH emission bands in the Spectrum of the night sky. I. *The Astrophysical Journal*, *111*, 555–564. https://doi.org/10.1086/145296

Meinel, A. B. (1950b). OH emission bands in the spectrum of the night sky. II. *The Astrophysical Journal*, *112*, 120–130. https://doi.org/10.1086/145321

Müllemann, A., Rapp, M., Lübken, F. J., & Hoffmann, P. (2002). In situ measurements of mesospheric turbulence during spring transition of the Arctic mesosphere. *Geophysical Research Letters*, *29*(10), 1477. https://doi.org/10.1029/2002GL014841

Scargle, J. D. (1982). Studies in astronomical time series analysis. II—Statistical aspects of spectral analysis of unevenly spaced data. *Astrophysical Journal*, *263*, 835–853. https://doi.org/10.1086/160554

Sedlak, R., Hannawald, P., Schmidt, C., Wust, S., & Bittner, M. (2016). High-resolution observations of small-scale gravity waves and turbulence features in the OH airglow layer. *Atmospheric Measurement Techniques*, *9*(12), 5955–5963. https://doi.org/10.5194/amt-9-5955-2016

Staquet, C., & Sommeria, J. (2002). Internal gravity waves: From instabilities to turbulence. *Annual Review of Fluid Mechanics*, *34*(1), 559–593. https://doi.org/10.1146/annurev.fluid.34.090601.130953

Swenson, G. R., & Gardner, C. S. (1998). Analytical models for the responses of the mesospheric OH* and Na layers to atmospheric gravity waves. *Journal of Geophysical Research*, *103*(D6), 6271–6294. https://doi.org/10.1029/97JD02985

Taylor, M. J., Pendleton, W. R. Jr., Pautet, P.-D., Zhao, Y., Olsen, C., Babu, H. K. S., et al. (2007). Recent progress in mesospheric gravity wave studies using nigthglow imaging system. *Revista Brasileira de Geofísica*, *25*, 49–58. https://doi.org/10.1590/S0102-261X2007000600007

Thrane, E. V., Blix, T. A., Hoppe, U. P., Lübken, F. J., Hillert, W., Lehmacher, G., et al. (1994). A study of small-scale waves and turbulence in the mesosphere using simultaneous in situ observations of neutral gas and plasma fluctuations. *Journal of Atmospheric and Terrestrial Physics*, *56*(13-14), 1797–1808. https://doi.org/10.1016/0021-9169(94)90011-6

Vetterling, W. T., Teukolsky, S. A., Flannery, B. P., & Press, W. H. (1992). *Numerical recipes in Fortran 77: The art of scientific computing*. New York: Cambridge University Press.

Paper 3

Franzen, C., Espy, P. J., & Hibbins, R. E. (2019). Modelled Effects of Temperature Gradients and Waves on the Hydroxyl Rotational Distribution in Ground-Based Airglow Measurements. *Submitted to Atmospheric Chemistry and Physics.*

Modelled Effects of Temperature Gradients and Waves on the Hydroxyl Rotational Distribution in Ground-Based Airglow Measurements

Christoph Franzen[1,2], Patrick Joseph Espy[1,2], Robert Edward Hibbins[1,2]

[1] Norwegian University of Science and Technology (NTNU), Trondheim, 7491, Norway

[2] Birkeland Centre for Space Science (BCSS), Norway

ABSTRACT

Spectroscopy of the hydroxyl (OH) airglow has been a commonly used way to remotely sense temperatures in the mesopause region for many decades. This technique relies on the OH rotational state populations to be thermalised through collisions with the surrounding gas into a Boltzmann distribution characterised by the local temperature. However, deviations of the rotational populations from a Boltzmann distribution characterised by a single temperature have been observed and attributed to an incomplete thermalisation of the OH from its initial, non-thermodynamic equilibrium distribution. Here we address an additional cause for the apparent amount of excess population in the higher rotational levels of the OH airglow brought about by integrating these OH emissions through vertical gradients in the atmospheric temperature. We find that up to 40 % of the apparent excess population, currently attributed to incomplete thermalisation, can be due to the vertical temperature gradients created by waves. Additionally, we find that the populations of the different upper vibrational levels are affected differently. These effects need to be taken into account in order to assess the true extent of non-thermodynamic equilibrium effects on the OH rotational populations.

INTRODUCTION

The hydroxyl (OH) airglow has been employed for many years for remote sensing of the Mesosphere and Lower Thermosphere (MLT) region (Meinel, 1950b, 1950a). The 8-km thick airglow layer is created at about 90 km altitude (Baker et al., 1988; Xu et al., 2012) by the highly exothermic reduction of ozone:

$$H + O_3 \rightarrow OH^* + O_2 \ (-76.9 \text{ kcal} \cdot \text{mole}^{-1}) \quad (1)$$

The excess heat of reaction, 76.9 kcal·mole^{-1} (~3.3 eV), produces the OH^* in excited vibrational quantum levels of v'=6-9 (e.g. Mlynczak et al. (1993)). Subsequent radiative cascading and collisional-deactivation produces OH^* in all vibrational levels ≤ 9. Radiative de-activation can occur between any two vibrational quantum levels, but transitions with $\Delta v = 2$ are preferred (Langhoff et al., 1986).

The excess energy of reaction (1) also creates rotational excitation within the OH^* molecule in addition to the vibrational excitation. The nascent rotational population for high rotational levels, J', shows a distribution characteristic of a temperature far above the local atmospheric temperature. Dodd et al. (1994) reported a nascent temperature of 760 K for $v' = 9$ and up to 2600 K for the $v' = 6$. Others report temperatures as high as 10^4 K (Khomich et al., 2008).

Low rotational levels with energy separations less than kT, typically exchanged during collisions, have been observed to have efficient energy transfer and are thermalised (Maylotte et al., 1972; Polanyi et al., 1972; Polanyi et al., 1975). Thus, these states are observed to be in local thermodynamic equilibrium (LTE) (Harrison et al., 1970; Harrison et al., 1971; Sivjee et al., 1972; Sivjee et al., 1987; Pendleton et al., 1993; Perminov et al., 2007). However, emission from the upper rotational levels, where the energy separation exceeds kT, indicates an excess, non-thermalized population in the these higher rotational levels (i.e. they are in non-local thermodynamic equilibrium or NLTE) (Pendleton et al., 1989; Pendleton et al., 1993; Dodd et al., 1994; Cosby et al., 2007; Noll et al., 2015). Work is currently underway to use observations of the excess populations in the high rotational levels of the OH airglow to determine state-to-state quenching coefficients and to understand the thermalisation process in OH (Kalogerakis et al., 2018).

Here we examine the effects of temperature gradients in the OH emission region on the resulting vertically integrated spectrum of the Meinel Δv=2 sequence. We assume that the OH is in LTE at every altitude, and vertically integrate the emission in each rotational line. We find that even if the OH is in strict LTE with the surrounding atmosphere, the temperature gradients through the OH emission region will create apparent excess emission in the higher OH rotational lines. These can be incorrectly interpreted as excess population due to NLTE effects, affecting the subsequent calculations of the thermalisation process. The deviations in the inferred populations from a single-temperature Boltzmann distribution are compared with observations that include both NLTE and temperature gradient effects. This comparison is made for realistic atmospheric temperature profiles that have been perturbed with realistic atmospheric gravity-waves in order to help quantify the true NLTE content needed to construct a quantitative picture of OH thermalisation.

Overview of the OH emission

Figure 1 shows an example of the OH airglow volume emission rate (VER) and a temperature profile, measured from the Sounding of the Atmosphere using Broadband Emission Radiometry (SABER) instrument aboard the NASA Thermosphere Ionosphere Mesosphere Energetics Dynamics (TIMED) satellite (Mlynczak, 1997; Russell et al., 1999). This specific measurement is a zonal mean and monthly average from July 2016 between the latitudes of 20 and 30 degrees north. The OH VER from the vibrational levels 8 and 9 is shown in red in the figure, while the black curve shows the temperature profile. It can be seen that the temperature is not constant through the OH layer. In this example the atmospheric temperature changes by over 10 K through the layer. This observed behaviour is similar to other observations, for example from French et al. (2010), who compared TIMED/SABER observations with ground-based observations.

Waves will exacerbate this effect by perturbing both the OH VER and changing the temperature gradient. Thus, the OH, even if thermalised at each altitude, will have different temperatures at each of those altitudes. Any instrument that integrates through the OH layer will therefore not see rotational line emission resulting from a single, average temperature, but from the whole span of temperatures present in the layer. That is, the emission from high rotational lines that occurs in the warm regions will be present

in the spectrum along with the predominantly low rotational level lines emitting from the colder regions.

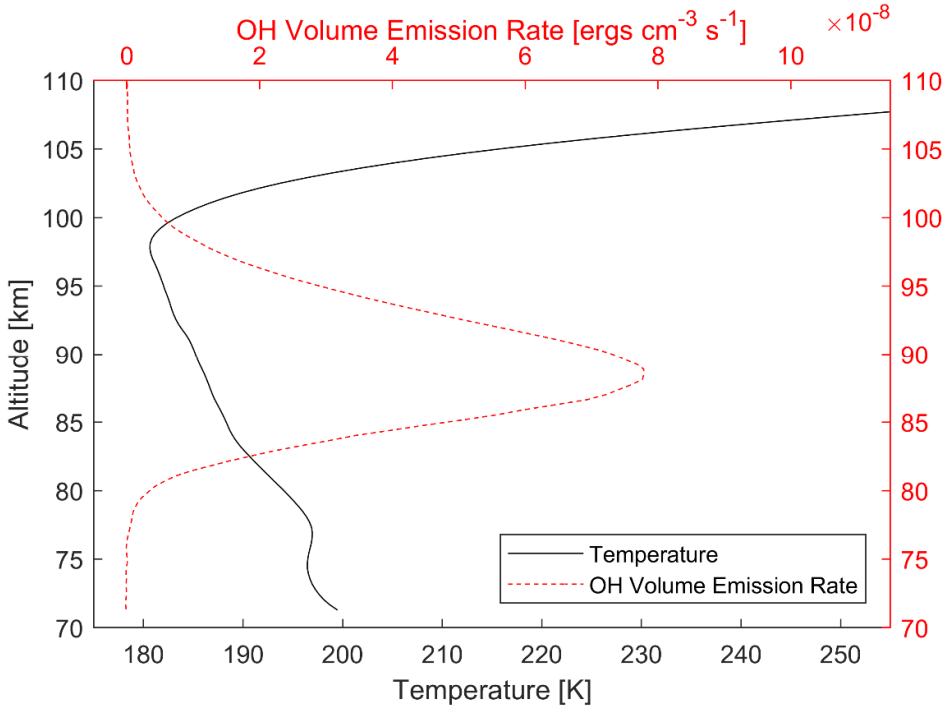

Figure 1: Example of a typical temperature profile (black) of the airglow layer and the VER (red -dashed) from the SABER satellite showing the variation of temperature through the emission region. This specific measurement is a zonal mean and monthly average from July 2016 between the latitudes of 20 and 30 degrees north for the Δv=2 bands from the 8 and 9 upper-state vibrational levels.

METHOD

We utilise a steady-state model of the OH VER, described below, to synthesise individual synthetic rotational spectra at 1 km intervals from 74 to 125 km, assuming that the OH is in LTE with the local temperature at each altitude. Each rotational line is integrated in altitude to give the net spectrum that would be observed by an instrument integrating through the layer. The distribution of emission in the rotational lines is then used to infer the population of the OH rotational levels, allowing us to quantify the portion of the inferred excess population in the upper levels that is due to the temperature gradients across the OH layer.

The OH model

The atmospheric background temperature and concentrations of N_2, O_2, H and O are taken from the empirical model of the US Naval Research Laboratory Mass Spectrometer and Incoherent Scatter radar (NRLMSISE-00) (Picone et al., 2002). The steady-state ozone concentration is then calculated from balancing the production and loss processes. The production mechanism is:

$$O + O_2 + M \rightarrow O_3 + M, \quad (2)$$

where M is a reaction mediator. The temperature dependent rate coefficients for these reactions are taken from the International Union for Pure and Applied Chemistry (IUPAC) Gas Kinetic Database (Atkinson et al., 2004). Loss processes include losses to O via

$$O + O_3 \rightarrow 2O_2, \quad (3)$$

using the reaction rate coefficient of Sander et al. (2003). The loss of O_3 to atomic hydrogen,

$$H + O_3 \rightarrow OH^* + O, \quad (4)$$

was also used to calculate the production rate of OH^* using the reaction rate coefficient (Sander et al., 2003). Due to the exothermicity of reaction 4, vibrational levels from v'=6 to 9 can be populated. The production of each vibrational level $OH^*(v')$ is calculated using the branching ratios from Sander et al. (2019). Collisional loss for each $OH^*(v')$ vibrational level was calculated for collisions with O, O_2 and CO_2 using the rate coefficients of Dodd et al. (1991), Knutsen et al. (1996), Dyer et al. (1997) and Chalamala et al. (1993), assuming quenching to the ground vibrational state, known as "sudden death" (McDade et al., 1987).

The total radiative loss from each vibrational level is given by $N_{v'}(z) / \tau_{v'}$, where $N_{v'}(z)$ is the concentration of the hydroxyl v' vibrational level and its lifetime, $\tau_{v'}$, is taken from Mies (1974). The total VER of any v' to v'' vibrational transition is then given by $V_{v'v''}(z) = \omega_{v'v''} \cdot N_{v'}(z) / \tau_{v'}$, where $\omega_{v'v''}$ is the vibrational branching ratio (Mies, 1974).

This radiative cascade into lower vibrational levels then acts as an additional production term for levels below v'=9. Balancing these production and loss terms at each height yields the steady-state concentration of each OH* vibrational level as a function of height, $N_{v'}(z)$. Such a model has been shown to fit observations, for example TIMED/SABER (Xu et al., 2012).

The wave model

As mentioned above, the background atmospheric temperature profile can be perturbed by waves. We therefore include wave-induced temperature perturbations in the model. Following Holton (1982), we limited the wave growth with altitude to maintain temperature gradients to below the dry adiabatic lapse rate. The background atmosphere mixing ratios from the NRLMSISE-00 model were also perturbed using the gravity wave polarisation relations from Vincent (1984). This perturbed background atmosphere and temperature profile were then used in the steady-state model for the OH to yield a new, wave-perturbed $N_{v'}(z)$ for the analysis.

Simulation of a ground-based measurement

The VER of a rotational transition for the *J'* to *J''* state from the upper state, *v'*, of the v' to v" vibrational band is given by:

$$V_{v'v''J'J''} = \frac{\omega_{v'v''}}{\tau_{v'}} \cdot N_{V'}(z) \cdot N_{J'} \cdot A_{J'J''}, \quad (5)$$

where $A_{J'J''}$ is the Einstein coefficient for the rotational transition and $N_{J'}$ is the population of the upper rotational level, *J'*. Assuming that collisions have thermalised the closely spaced rotational levels with the surrounding gas at temperature *T*, their population may be described using a Boltzmann distribution written as:

$$N_{v',J'} = N_{v'} 2(2J' + 1) \cdot exp\left(\frac{-E_{J'}}{k \cdot T(z)}\right) \quad (6)$$

Where $N_{v'}$ is the total population of the *v'* vibrational level from the model, $E_{J'}$ is the energy of the *J'* rotational level, and the factor *2(2J'+1)* is the degeneracy of that level (including Λ-doubling) (Herzberg, 1950).

Using the rotational transition probabilities of Rothman et al. (2013), the rotational line VERs are calculated within a single *v'* to *v"* transition assuming that the OH is in LTE with the surrounding gas at each altitude and therefore follows a Boltzmann distribution of population characterised by the local temperature. The VER of each rotational line is integrated through the layer from 74 km through to 125 km to give the intensity of the line, $I_{J'J''}$. This results in a net spectrum of low rotational lines that have been emitted from the cooler regions along with high rotational lines that were emitted from the warm regions, each weighted by the VER of the vibrational transition at each altitude, $N_{v'}(z) \cdot \omega_{v'v''} / \tau_{v'}$.

As an example, the OH model was used to create a synthetic spectrum of the (7,4) rotational-vibrational band, assuming LTE at every altitude level, for conditions for mid-July for a mid-latitude region. Specifically, the data presented are for Boulder, Colorado (40.0° N; 105.6° W) to make a direct comparison with the findings from Pendleton et al. (1993). The background temperature profile (black line) and the (7,4) VER variation with altitude (red line) are shown in Figure 2 (a). These are perturbed by the wave with an amplitude of 30 K at 90 km altitude, and a vertical wavelength of 30 km, shown in blue-dashed. The wave has the form

$$A_w(z) \cdot \cos\left(\frac{2\pi z}{\lambda_w} + \varphi_w\right), \qquad (7)$$

Where $A_w(z)$ is a function of altitude so as not to exceed the dry adiabatic lapse rate, and φ_w for this example is defined as zero at an altitude of 74 km, which is the lower edge of the model. The resulting distribution of rotational line intensities as a function wavelength for two altitudes is shown in Figure 2 (b) and (c). The net spectrum as observed by a ground-based instrument is analysed, as detailed below, to examine the influence of this high-rotational level tail on the fitted temperature.

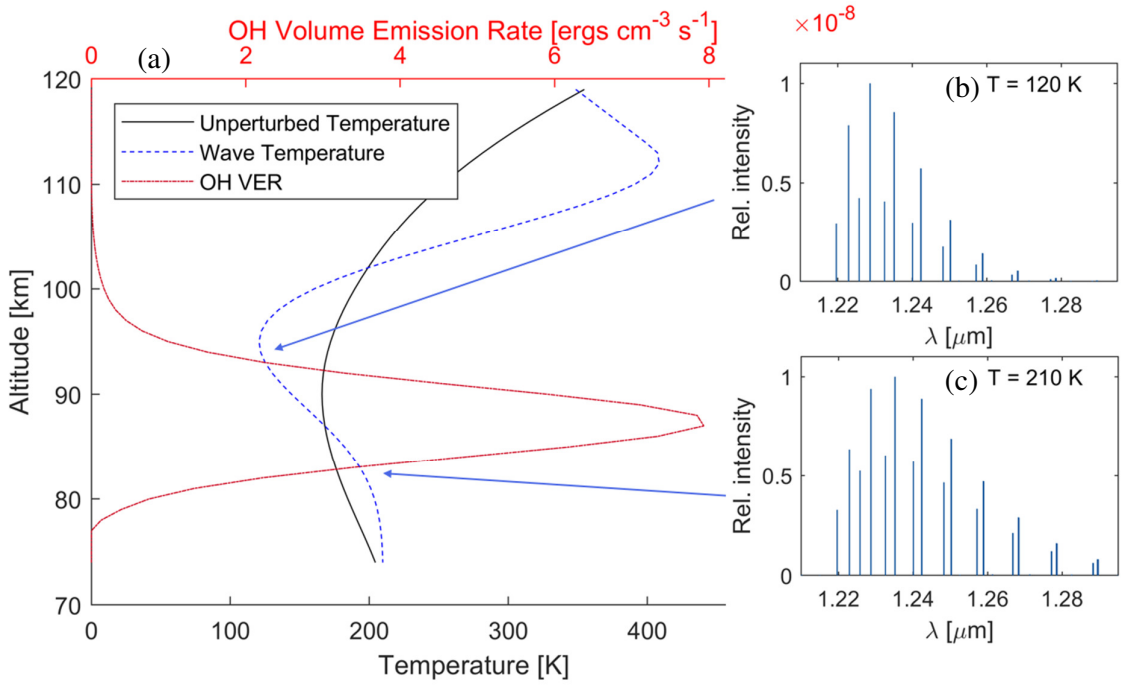

Figure 2: (a) Illustration of the change in the OH airglow spectrum with altitude due to the temperature profile. The red line shows a modelled VER profile of the OH in ergs cm^{-3} s^{1}. The black line shows the background temperature profile retrieved from the NRLMSISE-00 model. The blue dashed line shows the same temperature profile but perturbed by a wave with an amplitude of 30 K at 90 km altitude and a vertical wavelength of 30 km. The insets (b) and (c) on the right show OH spectra of the (7,4) transition at different altitudes for the wave case. The temperature variation causes a higher relative VER in the lower rotational lines at 95 km, but in the higher rotational lines at 80 km.

Temperature fitting

After integration through the layer, the relative population of the *J'* state relative to the lowest rotational energy level, E_0, is now given in terms of the line intensity by:

$$\frac{I_{J'J''}}{2(2J'+1)\cdot A_{J'J''}} = N_{V'} \cdot exp\left(\frac{-(E_{J'}-E_0)}{kT}\right) \quad (8)$$

Where $N_{v'}$ is the integral of the vibrational band VER $N_{v'}(z) \cdot \omega_{v'v''} / \tau_{v'}$ over altitude, and T is the effective rotational temperature of the altitude-integrated spectrum. From this, the observed line intensities from rotational levels of known quantum number, energy, and

transition probability may be used to define the relative total population and temperature using:

$$\ln\left(\frac{I_{J'J''}}{2(2J'+1)\cdot A_{J'J''}}\right) = \ln(N_{V'}) - \frac{1}{T}\left[\frac{\left(E_{J'}-E_0\right)}{k}\right] \tag{9}$$

Figure 3 shows the result in terms of Equation (9), of integrating each rotational line in the (7,4) Meinel band for the atmospheric perturbation of a wave with an amplitude of 30 K at 90 km altitude and 30 km vertical wavelength. This is the same wave as shown in Figure 2. Following Pendleton et al. (1993), fitting a temperature to the lowest three rotational levels of the OH spectrum yields the dashed red curve shown in Figure 3. It may be seen that the lowest three rotational levels are well characterized by a single, Boltzmann rotational temperature, $T_{1,3} = 155.8 \pm 0.8$ K, as has been observed in nightglow spectra (Baker et al., 1985; Espy et al., 1995; Noll et al., 2015; Franzen et al., 2017). However, there is excess emission in the higher rotational lines which could be interpreted as populations exceeding that expected from a thermalised Boltzmann distribution. This apparent excess population occurs even though the OH distribution was constrained to be a Boltzmann distribution with a single temperature at each altitude.

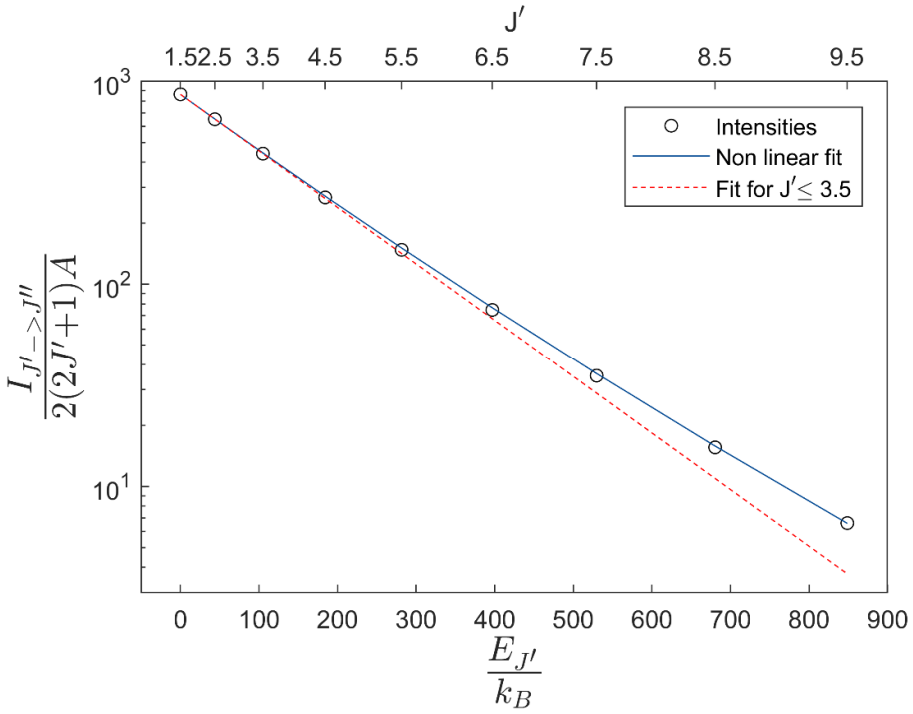

Figure 3: Population of P-branch lines of the (7,4) Meinel band as calculated with an atmospheric background profile containing the wave shown in Figure 2. The energies given on the x-axis are relative to the lowest rotational energy. An exponential fit to the lowest three rotational levels (red dashed line) underestimates the populations at higher levels. A non-linear fit as presented in Equation (10) can fit the intensities of rotational levels as high as $J' = 9.5$, while reproducing the same temperature as the fit to the lowest three levels.

A non-linear formulation can be used in order to characterise this excess population. This non-linear fit is of the form:

$$\ln\left(\frac{I_{J'J''}}{2(2J'+1)\cdot A_{J'J''}}\right) = \ln(N_{V'}) - \frac{1}{T}\left[\frac{\left(E_{J'}-E_0\right)}{k}\right] + \frac{\beta}{T^2}\left[\frac{\left(E_{J'}-E_0\right)}{k}\right]^2 \quad (10)$$

Here β is a non-linearity parameter, which is a free parameter in the non-linear fit. This non-linear fit is also presented in Figure 3 as a solid blue line, showing that the intensity in rotational lines as high as $J' = 9.5$ is now fitted. The retrieved temperature $T_{NL} = 154.9 \pm 0.1$ K, is the same as $T_{1,3}$ within the fitting uncertainties.

Expansion to arbitrary waves

So far, we have considered only a single wave with one given amplitude, wavelength and phase as an example. Different wave amplitudes A_w will, of course, change the populations seen in Figure 3. In the limiting case, where $A_w = 0$, the original background temperature profile is retrieved. Different wavelengths λ_w will also change the shape of the atmospheric temperature profile. Short λ_w waves can change the temperature toward both warmer and colder temperatures within the OH layer. Thus, their effect can be small when integrated over the whole layer. Longer λ_w waves, especially with λ_w on the order of, or longer than, the thickness of the OH layer, can introduce a temperature change that only warms one end of the layer and cools the opposite end. When such gradients reinforce the background temperature change with altitude, they can change the total integral over the OH layer substantially, as seen in Figure 3. Lastly, the wave phase φ_w can change the influence of the wave on the total integral of the OH layer. The same wave

would have the opposite temperature perturbation if φ_w was shifted by half a wavelength. In this case, the wave would work against the natural temperature gradient of the background atmosphere without a wave, resulting in a smaller effect than that shown in Figure 3.

All three wave parameters - A_w, λ_w and φ_w - should therefore be considered when modelling different waves to examine their influence on the total integrated OH spectrum. In this research, the three parameters were adjusted in equidistant steps. The amplitude A_w was varied between 0 K and 40 K at an altitude of 90 km, spanning a range of previously observed semi-diurnal tide amplitudes (Hagan et al., 1999; She et al., 2002; Shepherd et al., 2004; Zhang et al., 2006; Oberheide et al., 2011). The vertical wavelength λ_w was varied between 2 km and 80 km, spanning the range of gravity waves, tides and planetary waves (Davis et al., 2013). The phase φ_w was varied between 0 and 2π.

RESULTS AND DISCUSSION

Figure 3 shows that a large atmospheric temperature gradient can produce higher populations in the higher *J'* rotational lines than would be expected from a strict LTE fit with only one effective temperature. We now want to quantify how large this apparent excess population can become and compare it to the study by Pendleton et al. (1993). An ensemble of waves was simulated as described above. The apparent excess population and the non-linearity parameter, β, were calculated for each wave-perturbed temperature background profile.

Figure 4 shows two different wave scenarios for the (7,4) transition. The red plot (with the axis on the left-hand side) shows a no-wave scenario, where the atmospheric background temperature profile from the NLRMSISE-00 model is used. The apparent excess population is the ratio between the calculated intensity of a rotational line integrated in altitude, and the intensity of that line predicted by a Boltzmann distribution fitted to the distribution of integrated rotational line intensities using a single, effective temperature. It is clear that the first three lines with $J' \leq 3.5$ can be characterised by a single, effective Boltzmann temperature. However, all higher lines show populations in excess of that expected from a single effective temperature. The effective overpopulation

approaches approximately 12.5% for J' = 9.5, even though the OH molecule is thermalised with the local temperature at every altitude.

The blue bars (with the plot on the right side) show a scenario with a wave perturbing the atmosphere. This specific wave has an amplitude $A_w = 30$ K at 90 km altitude, $\lambda_w = 30$ km and $\varphi_w = 4.9\ rad$. This would be a large amplitude gravity wave, but still within the range of atmospheric tidal observations. Although different J' levels are affected differently, the general shape is similar to that observed with the no-wave scenario. However, the magnitude of the effect is much greater. The first three lines show the populations expected in a single temperature LTE case, while higher J' levels yield increasingly higher apparent excess populations. For the highest line considered in this paper with J' = 9.5, the apparent excess population is twice that expected for a Boltzmann distribution with a single effective temperature, despite the OH being in LTE at every altitude.

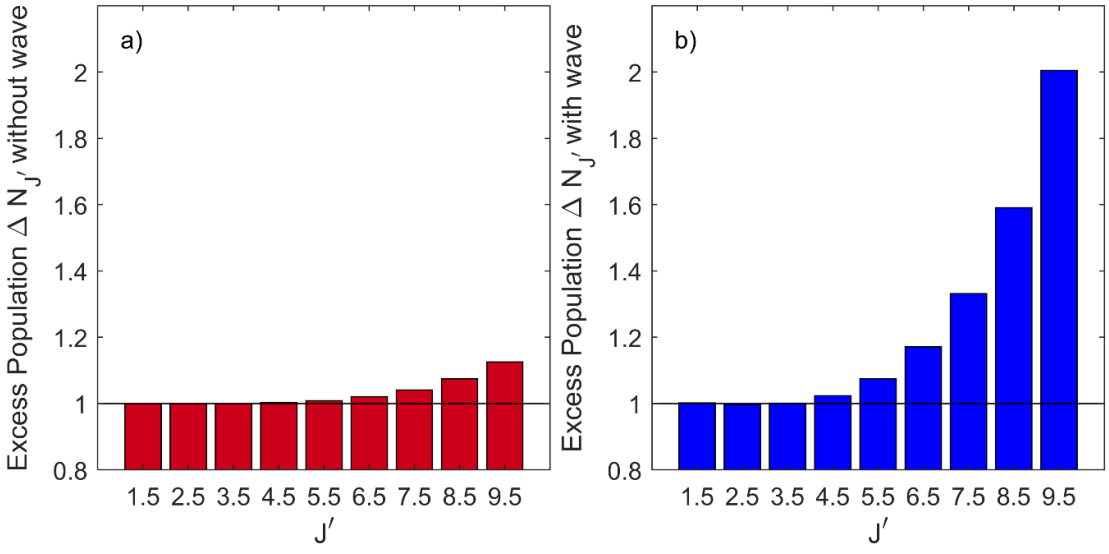

Figure 4: The calculated apparent excess population of the OH (7,4) P(J') lines. Red on the left is calculated with the climatological temperature gradient shown from NRLMSISE-00 above Boulder, Colorado (40.0° N; 105.6° W) in mid-July. Blue on the right is calculated with a wave of $A_w = 30$ K at 90 km, $\lambda_w = 30$ km and a phase that yields the maximum effect, $\varphi_w = 4.9$ rad.

These results can be compared to the findings from Pendleton et al. (1993) in their figure 16, for the (7,4) transition above Boulder, Colorado during mid-summer, the same season and transition as presented here. Although the measurement from Pendleton et al. (1993) included NLTE effects, the overall shape of the distribution is similar to the LTE simulations presented here. When comparing these results, note that Pendleton et al. (1993) use the lower-state quantum number N, which corresponds to our $J' + ½$. The first three rotational levels reproduce the same population as an atmosphere in LTE characterised by a single temperature, and above that, there is excess population. The difference between the absolute numbers we observe and those of Pendleton et al. (1993) indicates the portion of the NLTE that might be due to the temperature gradient effects observed here. For example, Pendleton et al. (1993) reported an apparent excess population of around a factor of 2 for the $P_1(N=7)$ (i.e. $J'=6.5$) line. However, for the two cases presented here in Figure 4, there is less apparent excess population. While the no-wave scenario yields an apparent excess population of 1.02, a background profile with a wave yields 1.17 times the population. These numbers mean that up to about 17 % of the effect Pendleton et al. (1993) observed could be due to wave activity and not NLTE effects. Thus, the effect of the atmospheric temperature background has to be considered in addition to NLTE effects whenever the populations inferred from integrated airglow observations of high J' lines are to be used in kinetic thermalisation models.

This calculation of the apparent excess population can now be repeated for waves of different amplitudes, wavelengths and phases. Figure 5 shows the non-linearity in terms of the β-value of the temperature fit (from Equation (10)) and the corresponding apparent excess population of the sixth rotational line with $J' = 6.5$ ($N = 7$), the highest line reported by Pendleton et al. (1993) in their NLTE study of the OH. The figure shows the (7,4) transition, which is the same transition Pendleton et al. (1993) used. In Figure 5 a) the non-linearity of the temperature fit increases with both wave strength and vertical wavelength, approaching 2% of the linear temperature variation (see Equation 10). Figure 5 b) shows the phase that yields the highest apparent excess population for a given wave amplitude and wavelength. There are small but observable effects in the limiting case of no waves (background atmosphere, see Figure 4 a)), and the apparent excess population increases for longer wavelengths and stronger waves similarly to the non-linearity of the

fit. Extreme waves with 40 K amplitude at an altitude of 90 km can cause up to 30 % apparent excess populations in the J'=6.5 line.

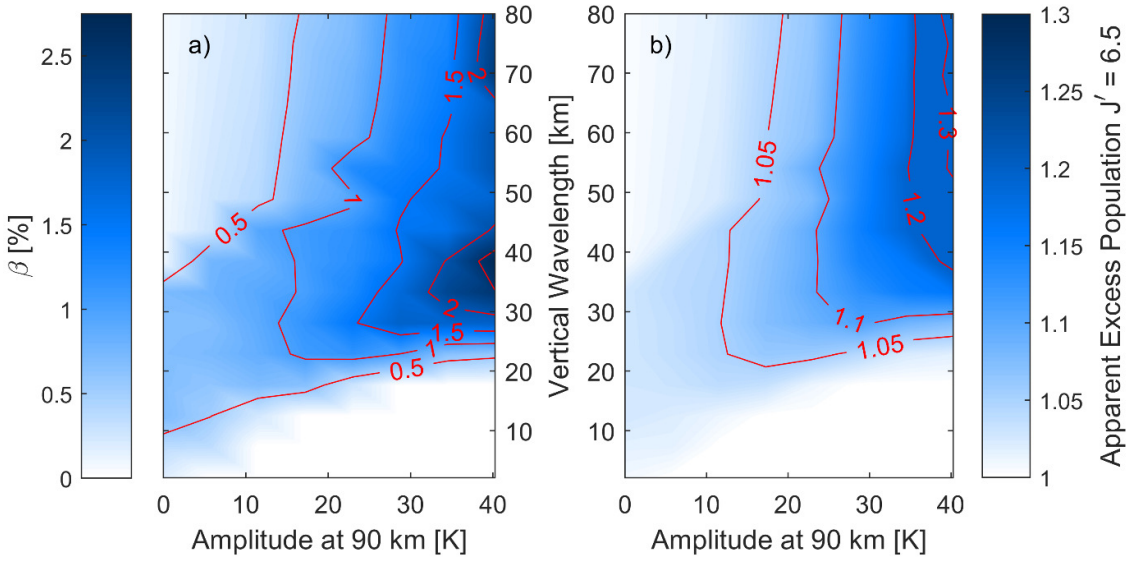

Figure 5: a) The β-value from the non-linear fit (Equation (10)), and b), the apparent excess population of the J' = 6.5 (N = 7) of the (7,4) Meinel transition for the ensemble wave spectrum. The values are shown as a function of the wavelength, λ_w, and the amplitude, A_w. Each value represents the phase φ_w where the apparent excess population was largest. Extreme waves (tides) can show a non-linearity of about 2% corresponding to an apparent excess population of 30%.

While Figure 5 shows the (7,4) transition, Figure 6 shows the same analysis for the commonly observed (3,1) transition. Both the β-value and the apparent excess population look qualitatively similar to the (7,4) band, but the effect of waves on the (3,1) transition is about 30 % stronger. That means that the non-linearity exceeds 2.5 % and the apparent excess population of the J' = 6.5 level is up to 40 % for the largest waves shown here.

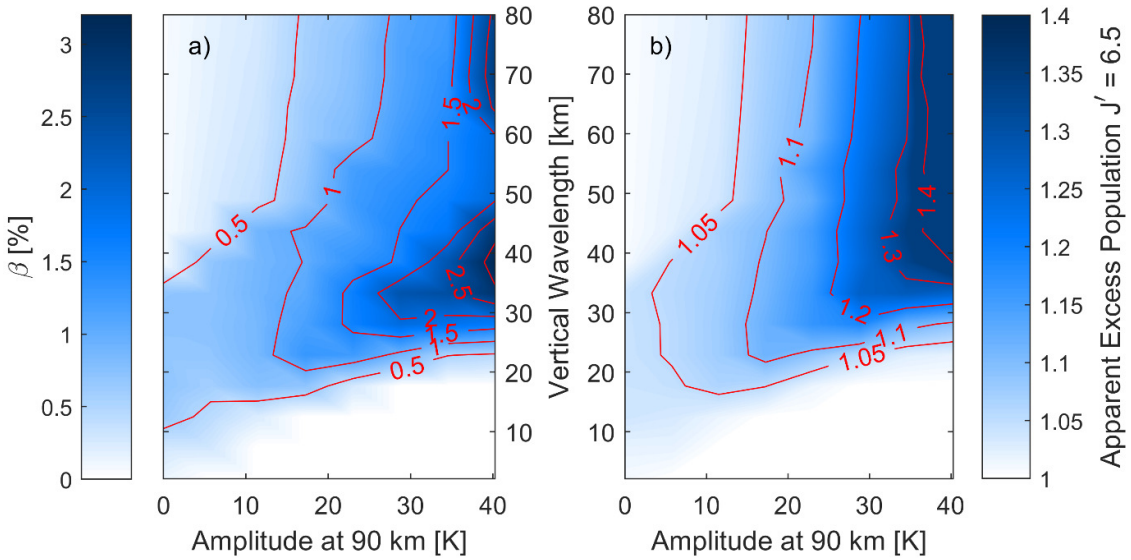

Figure 6: As Figure 5, but this time for the (3,1) transition. Both the β-value from the non-linear fit in a) and the apparent excess population of the J' = 6.5 upper level in b) show a stronger effect than seen for the (7,4) transition in Figure 5.

Tests showed that the difference in the apparent excess population between the (3,1) and (7,4) bands is unlikely to be due to the altitude separation of the different vibrational levels in the OH airglow layer (von Savigny et al., 2012). Repeating the analysis and weighting the v'=3 and 7 levels with the same VER profile yields essentially the same result; as did performing the analysis in an unperturbed isothermal background temperature profile. Instead it is due to the compressed rotational energy structure of the higher vibrational levels that lie closer to the dissociation limit. A given J' level in a low vibrational state will have more rotational energy than one in a high vibrational state. So for a given temperature, higher rotational levels will be thermally populated in the higher vibrational levels. These thermally populated higher rotational levels then make the perturbing effects of waves relatively less important.

Figure 7 illustrates the dependency of the amount of apparent excess population on the different vibrational upper levels at different altitudes. For consistency, the apparent excess population of the J' = 6.5 upper level is again shown. All data points are for the

wave presented above as an example, with an amplitude of 30 K at 90 km altitude and a vertical wavelength of 30 km.

The smallest upper vibrational level of v' = 2 shows an apparent excess population of about 28 %, while the highest upper vibrational level of v' = 9 only shows an apparent excess population of about 8 %.

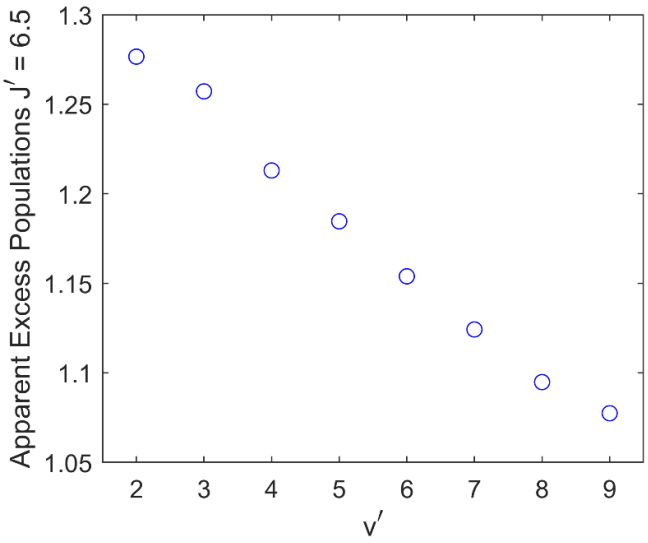

Figure 7: The apparent excess population of the J' = 6.5 upper level for a wave with wavelength 30 km and an amplitude of 30 K at 90 km altitude as a function of vibrational upper level. The effect of the waves, creating the apparent excess population decreases with rising vibrational quantum number v'.

CONCLUSIONS

Spectroscopic observations of the OH airglow have been commonly used to measure temperatures in the MLT. The OH radiates over an extended, Chapman-like layer that extends over several kilometres, over which the temperature is changing. Strong waves perturbing the MLT can make this change in temperature within the OH layer substantial. The simulations executed here show that these temperature profiles can change the populations of the different rotational lines in a given Meinel (v',v'') band. Even though the simulations have the OH in LTE at every altitude, the integrated intensities of the higher rotational lines indicate an apparent excess population that could be misinterpreted

as contributing to the NLTE effects previously reported (Pendleton et al., 1993; Cosby et al., 2007; Noll et al., 2015).

We have shown in this work that the influence of a wave that has an amplitude of 30 K at an altitude of 90 km can explain between 12 % and 30 % of the effects previously ascribed to NLTE by Pendleton et al. (1993). Smaller waves can also have an impact of up to 10 %, and their impact can not be ignored. Other transitions with lower vibrational quantum numbers show even higher apparent excess populations caused by this temperature-variation effect. We conclude that it is necessary to consider the temperature profile in order to infer the rotational distribution of the OH from ground-based airglow observations.

ACKNOWLEDGEMENTS

This work was supported by the Research Council of Norway/CoE under contract 223252/F50. We thank Halvor Borge, who undertook some preliminary studies on this research during his Master thesis at NTNU in the spring semester 2018. We also thank Kate Faloon for her work on the chemical model.

REFERENCES

Atkinson, R., Baulch, D. L., Cox, R. A., Crowley, J. N., Hampson, R. F., Hynes, R. G., . . . Troe, J. (2004). Evaluated Kinetic and Photochemical Data for Atmospheric Chemistry: Volume I - Gas Phase Reactions of Ox, Hox, Nox and Sox Species. *Atmos. Chem. Phys., 4*(6), 1461-1738. doi:10.5194/acp-4-1461-2004

Baker, D. J., & Stair, J. A. T. (1988). Rocket Measurements of the Altitude Distributions of the Hydroxyl Airglow. *Phys Scripta, 37*(4), 611-622.

Baker, D. J., Steed, A. J., Ware, G. A., Offermann, D., Lange, G., & Lauche, H. (1985). Ground-Based Atmospheric Infrared and Visible Emission Measurements. *Journal of Atmospheric and Terrestrial Physics, 47*(1), 133-145. doi:https://doi.org/10.1016/0021-9169(85)90129-1

Chalamala, B. R., & Copeland, R. A. (1993). Collision Dynamics of OH(X 2π, V=9). *The Journal of Chemical Physics, 99*(8), 5807-5811. doi:doi:http://dx.doi.org/10.1063/1.465932

Cosby, P. C., & Slanger, T. G. (2007). OH Spectroscopy and Chemistry Investigated with Astronomical Sky Spectra. *Canadian Journal of Physics, 85*(2), 77-99. doi:10.1139/p06-088

Davis, R. N., Du, J., Smith, A. K., Ward, W. E., & Mitchell, N. J. (2013). The Diurnal and Semidiurnal Tides over Ascension Island (8 S, 14 W) and Their Interaction with the Stratospheric Quasi-Biennial Oscillation: Studies with Meteor Radar, Ecmam and Waccm. *Atmos. Chem. Phys., 13*(18), 9543-9564. doi:10.5194/acp-13-9543-2013

Dodd, J. A., Lipson, S. J., & Blumberg, W. A. M. (1991). Formation and Vibrational Relaxation of OH (X 2πi,V) by O2 and Co2. *The Journal of Chemical Physics, 95*(8), 5752-5762. doi:10.1063/1.461597

Dodd, J. A., Lipson, S. J., Lowell, J. R., Armstrong, P. S., Blumberg, W. A. M., Nadile, R. M., . . . Green, B. D. (1994). Analysis of Hydroxyl Earthlimb Airglow Emissions: Kinetic Model for State-to-State Dynamics of OH (Y,N). *Journal of Geophysical Research: Atmospheres, 99*(D2), 3559-3585. doi:doi:10.1029/93JD03338

Dyer, M. J., Knutsen, K., & Copeland, R. A. (1997). Energy Transfer in the Ground State of OH: Measurements of OH(Y=8,10,11) Removal. *The Journal of Chemical Physics, 107*(19), 7809-7815. doi:10.1063/1.475094

Espy, P. J., & Hammond, M. R. (1995). Atmospheric Transmission Coefficients for Hydroxyl Rotational Lines Used in Rotational Temperature Determinations. *J Quant Spectrosc Ra, 54*(5), 879-889. doi:http://dx.doi.org/10.1016/0022-4073(95)00109-X

Franzen, C., Hibbins, R. E., Espy, P. J., & Djupvik, A. A. (2017). Optimizing Hydroxyl Airglow Retrievals from Long-Slit Astronomical Spectroscopic Observations. *Atmospheric Measurement Techniques, 10*(8), 3093-3101. doi:10.5194/amt-10-3093-2017

French, W. J. R., & Mulligan, F. J. (2010). Stability of Temperatures from Timed/Saber V1.07 (2002–2009) and Aura/Mls V2.2 (2004–2009) Compared with OH(6-2) Temperatures Observed at Davis Station, Antarctica. *Atmos. Chem. Phys., 10*(23), 11439-11446. doi:10.5194/acp-10-11439-2010

Hagan, M. E., Burrage, M. D., Forbes, J. M., Hackney, J., Randel, W. J., & Zhang, X. (1999). Gswm-98: Results for Migrating Solar Tides. *Journal of Geophysical Research: Space Physics, 104*(A4), 6813-6827. doi:10.1029/1998ja900125

Harrison, A. W., Evans, W. F. J., & Llewellyn, E. J. (1971). Study of the (4–1) and (5–2) Hydroxyl Bands in the Night Airglow. *Canadian Journal of Physics, 49*(19), 2509-2517. doi:10.1139/p71-297

Harrison, A. W., Llewellyn, E. J., & Nicholls, D. C. (1970). Night Airglow Hydroxyl Rotational Temperatures. *Canadian Journal of Physics, 48*(15), 1766-1768. doi:10.1139/p70-224

Herzberg, G. (1950). *Molecular Spectra and Molecular Strucutre. I. Spectra of the Diatomic Molecule*. New York: D. Van Nostrand Company, Inc.

Holton, J. R. (1982). The Role of Gravity Wave Induced Drag and Diffusion in the Momentum Budget of the Mesosphere. *Journal of the Atmospheric Sciences, 39*(4), 791-799. doi:10.1175/1520-0469(1982)039<0791:trogwi>2.0.co;2

Kalogerakis, K. S., Matsiev, D., Cosby, P. C., Dodd, J. A., Falcinelli, S., Hedin, J., . . . Thiebaud, J. E. (2018). New Insights for Mesospheric OH: Multi-Quantum Vibrational Relaxation as a Driver for Non-Local Thermodynamic Equilibrium. *Ann. Geophys., 36*(1), 13-24. doi:10.5194/angeo-36-13-2018

Khomich, V. Y., Semenov, A. I., & Shefov, N. N. (2008). *Airglow as an Indicator of Upper Atmospheric Structure and Dynamics*. Berlin, Germany: Springer.

Knutsen, K., Dyer, M., & Copeland, R. (1996). *Collisional Removal of OH (X 2π,Nu =7) by O2, N2, Co2, and N2o* (Vol. 104).

Langhoff, S. R., Werner, H. J., & Rosmus, P. (1986). Theoretical Transition Probabilities for the OH Meinel System. *Journal of Molecular Spectroscopy, 118*(2), 507-529. doi:https://doi.org/10.1016/0022-2852(86)90186-4

Maylotte, D. H., Polanyi, J. C., & Woodall, K. B. (1972). Energy Distribution among Reaction Products. Iv. X+Hy (X ≡ Cl, Br; Y ≡ Br, I), Cl+Di. *The Journal of Chemical Physics, 57*(4), 1547-1560. doi:10.1063/1.1678436

McDade, I. C., & Llewellyn, E. J. (1987). Kinetic Parameters Related to Sources and Sinks of Vibrationally Excited OH in the Nightglow. *Journal of Geophysical Research: Space Physics, 92*(A7), 7643-7650. doi:10.1029/JA092iA07p07643

Meinel, A. B. (1950a). OH Emission Bands in the Spectrum of the Night Sky. I. *Astrophys J, 111*, 555-564.

Meinel, A. B. (1950b). OH Emission Bands in the Spectrum of the Night Sky. Ii. *Astrophys J, 112*, 120-130.

Mies, F. H. (1974). Calculated Vibrational Transition Probabilities of OH(X2π). *Journal of Molecular Spectroscopy, 53*(2), 150-188. doi:https://doi.org/10.1016/0022-2852(74)90125-8

Mlynczak, M. G. (1997). Energetics of the Mesosphere and Lower Thermosphere and the Saber Experiment. *Advances in Space Research, 20*(6), 1177-1183. doi:https://doi.org/10.1016/S0273-1177(97)00769-2

Mlynczak, M. G., & Solomon, S. (1993). A Detailed Evaluation of the Heating Efficiency in the Middle Atmosphere. *Journal of Geophysical Research: Atmospheres, 98*(D6), 10517-10541.

Noll, S., Kausch, W., Kimeswenger, S., Unterguggenberger, S., & Jones, A. M. (2015). OH Populations and Temperatures from Simultaneous Spectroscopic Observations of 25 Bands. *Atmos. Chem. Phys., 15*(7), 3647-3669.

Oberheide, J., Forbes, J. M., Zhang, X., & Bruinsma, S. L. (2011). Climatology of Upward Propagating Diurnal and Semidiurnal Tides in the Thermosphere. *Journal of Geophysical Research: Space Physics, 116*(A11). doi:10.1029/2011ja016784

Pendleton, W. R., Espy, P. J., Baker, D., Steed, A., Fetrow, M., & Henriksen, K. (1989). Observation of OH Meinel (7,4) P(N″=13) Transitions in the Night Airglow. *Journal of Geophysical Research: Space Physics, 94*(A1), 505-510. doi:doi:10.1029/JA094iA01p00505

Pendleton, W. R., Espy, P. J., & Hammond, M. R. (1993). Evidence for Non-Local-Thermodynamic-Equilibrium Rotation in the OH Nightglow. *Journal of Geophysical Research: Space Physics, 98*(A7), 11567-11579. doi:10.1029/93JA00740

Perminov, V. I., Semenov, A. I., & Shefov, N. N. (2007). On Rotational Temperature of the Hydroxyl Emission. *Geomagn Aeron+, 47*(6), 756-763. doi:10.1134/s0016793207060084

Picone, J. M., Hedin, A. E., Drob, D. P., & Aikin, A. C. (2002). Nrlmsise-00 Empirical Model of the Atmosphere: Statistical Comparisons and Scientific Issues. *J Geophys Res-Space, 107(A12)*, 1468. doi:10.1029/2002JA009430

Polanyi, J. C., & Sloan, J. J. (1975, 1975-01-01). *Detailed Rate Constants for the Reactions H + O3 --> OH(Nu',J') + O2 and H + No2 --> OH(Nu'',J') + No.* Paper presented at the Symposium on chemical kinetics data for the upper and lower atmosphere, United States.

Polanyi, J. C., & Woodall, K. B. (1972). Energy Distribution among Reaction Products. Vi. F+H2, D2. *The Journal of Chemical Physics, 57*(4), 1574-1586. doi:10.1063/1.1678438

Rothman, L. S., Gordon, I. E., Babikov, Y., Barbe, A., Chris Benner, D., Bernath, P. F., . . . Wagner, G. (2013). The Hitran2012 Molecular Spectroscopic Database. *J Quant Spectrosc Ra, 130*, 4-50.

Russell, J. M., Mlynczak, M. G., Gordley, L. L., Tansock, J., & Esplin, R. (1999). An Overview of the Saber Experiment and Preliminary Calibration Results. In A. M. Larar (Ed.), *Optical Spectroscopic Techniques and Instrumentation for Atmospheric and Space Research Iii* (Vol. 3756, pp. 277-288). Bellingham: Spie-Int Soc Optical Engineering.

Sander, S. P., Friedl, R. R., DeMore, W. B., Ravishankara, A. R., & Kolb, C. E. (2019). *Chemical Kinetics and Photochemical Data for Use in Stratospheric Modeling Supplement to Evaluation 12: Update of Key Reactions*.

Sander, S. P., Friedl, R. R., Golden, D. M., Kurylo, M., Huie, R., Orkin, V., . . . Finlayson-Pitts, B. (2003). *Chemical Kinetics and Photochemical Data for Use in Atmosheric Studies; Jpl Publication 02-25*.

She, C. Y., Chen, S., Williams, B. P., Hu, Z., Krueger, D. A., & Hagan, M. E. (2002). Tides in the Mesopause Region over Fort Collins, Colorado (41°N, 105°W) Based on Lidar Temperature Observations Covering Full Diurnal Cycles. *Journal of Geophysical Research: Atmospheres, 107*(D18), ACL 4-1-ACL 4-12. doi:10.1029/2001jd001189

Shepherd, M., & Fricke-Begemann, C. (2004). Study of the Tidal Variations in Mesospheric Temperature at Low and Mid Latitudes from Windii and Potassium Lidar Observations. *Annales Geophysicae, 22*(5), 1513-1528.

Sivjee, G. G., Dick, K. A., & Feldman, P. D. (1972). Temporal Variations in Night-Time Hydroxyl Rotational Temperature. *Planetary and Space Science, 20*(2), 261-269. doi:https://doi.org/10.1016/0032-0633(72)90107-9

Sivjee, G. G., & Hamwey, R. M. (1987). Temperature and Chemistry of the Polar Mesopause OH. *J Geophys Res-Space, 92*(A5), 4663-4672. doi:10.1029/JA092iA05p04663

Vincent, R. A. (1984). Gravity-Wave Motions in the Mesosphere. *Journal of Atmospheric and Terrestrial Physics, 46*(2), 119-128. doi:https://doi.org/10.1016/0021-9169(84)90137-5

von Savigny, C., McDade, I. C., Eichmann, K. U., & Burrows, J. P. (2012). On the Dependence of the OH* Meinel Emission Altitude on Vibrational Level: Sciamachy Observations and Model Simulations. *Atmospheric Chemistry and Physics, 12*(18), 8813-8828.

Xu, J., Gao, H., Smith, A. K., & Zhu, Y. (2012). Using Timed/Saber Nightglow Observations to Investigate Hydroxyl Emission Mechanisms in the Mesopause Region. *J Geophys Res-Atmos, 117*(D2), 1-22. doi:10.1029/2011JD016342

Zhang, X., Forbes, J. M., Hagan, M. E., Russell III, J. M., Palo, S. E., Mertens, C. J., & Mlynczak, M. G. (2006). Monthly Tidal Temperatures 20–120 Km from Timed/Saber. *Journal of Geophysical Research: Space Physics, 111*(A10). doi:10.1029/2005ja011504

Paper 4

Franzen, C., Espy, P. J., Hofmann, N., Hibbins, R. E., & Djupvik, A. A. (2019). Measurement of Q-branch transition probabilities for several hydroxyl Meinel bands. *To be submitted to Journal of Quantitative Spectroscopy & Radiative Transfer.*

Measurement of Q-branch transition probabilities for several hydroxyl Meinel bands

Christoph Franzen[1,2], Patrick Joseph Espy[1,2], Niklas Hofmann[3], Robert Edward Hibbins[1,2], Anlaug Amanda Djupvik[4]

[1] Norwegian University of Science and Technology (NTNU), Trondheim, 7491, Norway.
[2] Birkeland Centre for Space Science (BCSS), Norway.
[3] Universität Regensburg, Regensburg, 93053, Germany
[4] Nordic Optical Telescope, E-38700 Santa Cruz De La Palma, Spain

ABSTRACT

Spectroscopic measurements of the hydroxyl (OH) airglow emissions are often used to infer neutral temperatures near the mesopause. Correct Einstein coefficients for the various transitions in the OH airglow are needed to calculate accurate temperatures. However, studies from French et al. (2000) and Pendleton et al. (2002) showed experimentally and theoretically that the most commonly used Einstein spontaneous emission transition probabilities for the Q-branch of the (6,2) Meinel transition are overestimated. Extending their work to several $\Delta v = 2$ and 3 transitions from $v' = 3$ to 9, we have determined Einstein coefficients for the first four Q-branch rotational lines. These have been derived from high resolution, high signal to noise spectroscopic observations of the OH airglow in the night sky from the Nordic Optical Telescope. The Q-branch Einstein coefficients calculated from the spectra show that tabulated values currently in the HITRAN database (Rothman et al., 2013) overestimate many of the Q-branch transition probabilities. Our results indicate that the aforementioned findings of Pendleton et al. (2002) and French et al. (2000) for the OH Meinel (6,2) transition also occur for the $\Delta v = 2$ and 3 transitions presented here.

1 INTRODUCTION

The reduction of ozone creates hydroxyl (OH) in the upper mesosphere via:

$$H + O_3 \rightarrow OH^* + O_2 \quad (1)$$

This chemical reaction is highly exothermic and creates the OH in excited vibrational and rotational states. Radiative relaxation of the OH results in the bright near-infrared radiation, which is known as OH nightglow or airglow. The OH emission occurs over an approximately 8 km thick layer (Baker et al., 1988) and spectroscopic observations of the nightglow have been used to infer the atmospheric conditions at the peak of the layer altitude near 87 km (e.g. Pendleton et al., 1989; Sivjee, 1992; Bittner et al., 2000; Espy et al., 2002; Taylor et al., 2007; Wüst et al., 2017; Franzen et al., 2018).

If the OH rotational states are fully thermalised with the surrounding atmosphere into a Boltzmann distribution, then the distribution of intensities in the rotational structure will yield a rotational temperature equal to the atmospheric temperature at this altitude. It is possible to calculate the rotational temperature of the OH whenever at least two spectral lines coming from different upper rotational levels, J', are observed. However, the calculation of a rotational temperature from spectral line intensities requires the precise knowledge of the Einstein spontaneous emission coefficients, $A_{v'',v',J'',J'}$. There have been several calculations of these Einstein coefficients in the past (Mies, 1974; Langhoff et al., 1986; Turnbull et al., 1989; Pickett et al., 1998), and those calculated by Pickett et al. (1998) have been tabulated in the HITRAN database (Rothman et al., 2013).

High-resolution observations over a limited spectral range, such as those using Fabry-Perot interferometers, utilise the compressed rotational structure of the Q-branch to determine rotational structure (Wiens et al., 1997; Innis et al., 2001). Such high-spectral resolution observations can compare kinetic and rotational temperatures in order to determine the extent of the OH rotational state thermalisation (Cosby et al., 2007; Noll et al., 2015). Pendleton et al. (2002) utilised measurements from French et al. (2000) to show that the Einstein coefficients from the (6,2) Meinel transition with $\Delta J = 0$ (Q-branch) are significantly lower than theoretically predicted. Pendleton et al. (2002) explained this disparity as due to perturbations by excited electronic states causing the ground state electronic angular momentum to de-couple from the inter-nuclear axis. This causes mixing of the two ground-state levels whose electronic angular momentum along the inter-nuclear axis is given by $\Omega = 1/2$ and 3/2, subsequently affecting the transition

probabilities of primarily the Q-branch. However, this angular momentum uncoupling does not appreciably affect the P- and R-branch Einstein coefficients, where tabulated values agree with those observed (French et al., 2000).

This angular-momentum uncoupling was verified for the (6,2) band, but has not been tested experimentally for transitions from other vibrational levels. Here we present measurements of the Q-branch Einstein coefficients relative to the P-branch for seven vibrational transitions; (3,1), (4,2), (5,3), (6,4), (7,4), (8,5) and (9,7) using two different methods. We show that many of the measured Einstein coefficients are significantly lower than those tabulated in HITRAN (Rothman et al., 2013), indicating that the angular momentum uncoupling is a general feature that varies with vibrational level.

2 INSTRUMENTATION AND DATA SET

The data presented in this paper were obtained with the Nordic Optical Telescope (NOT). The NOT is located in La Palma, the Canary Islands (17°53' W, 28°45' N). It is equipped with a 2560 mm primary mirror (Djupvik et al., 2010). Spectroscopic observations in the near-infrared are taken with the Nordic Optical Telescope near-infrared Camera and spectrograph (NOTCam) instrument. Data presented here are recorded with a slit size of 50 mm x 0.128 mm, which gives a field of view of 4 arc minutes by 0.6 arc seconds. The resolving power of $R = \lambda / \Delta\lambda \sim 2100$ is high enough to separate the main OH airglow rotational lines in observed spectra.

NOTCam spectroscopy uses an echelle grism and the spectral orders are separated with broad band filters. Most frequently the filters J, H, and K are used to isolate the wavelength regions 1.165-1.328 μm, 1.484 - 1.780 μm, and 2.083 - 2.363 μm, respectively. The J-band filter spans two OH Meinel transitions, the (7,4) and (8,5). The H-band filter contains four transitions, namely the (3,1), (4,2), (5,3) and the (6,4) transition. Lastly, while the K-band filter spans two transitions, the (8,6) and the (9,7), the filter does not include the (8,6) Q-branch and only the (9,7) is used for this study.

The airglow data have been extracted from the terrestrial background of astronomical observations of point sources that span the years from 2007 to 2017. Data were selected with preference for long integration times in order to achieve the highest quality.

Observations of astronomical targets are typically obtained as a set of shorter integrations. These sequences have been treated as a single observation with an integration time equal to the sum of integration times of the individual spectra. These sum of integration times spanned between 240 seconds and 4800 seconds. The total integration time of all observations considered in this research is 4.1 hours for the J- and the H-band each and 9.6 hours for the K-band. Any spectra perturbed by other light sources or otherwise contaminated were not used.

3 METHOD

Data preparation

Unless otherwise stated, the data reduction used here typically follows that developed and described in Franzen et al. (2017). The NOTCam spectra of astronomical point sources were chosen as described above. First, dead and hot pixels, i.e. pixels with an over sensitive measured current, were removed according to established pixel masks (the masks can be found on the NOT web page http://www.not.iac.es). A dark-current was subtracted and a good relative intensity calibration was obtained with the help of a flat-field image from a 3200 K Halogen lamp. The spectra of any astronomical object, e.g. stars, were masked out. Since point-source astronomical objects only extend over a few spatial pixels (typically less than 60), these regions were masked leaving the spectrum of the extended-source atmosphere in the background. Warping effects along the slit from the telescope optics were accounted for and the final OH spectrum was integrated along the slit dimension, to yield a conventional spectrum. The spectral calibration was done with the theoretical OH line positions from the HITRAN database. These steps were executed for each individual image and the resulting spectra towards the same target were finally summed up to yield one, high signal-to-noise spectrum of the OH airglow. Initial OH rotational temperatures were estimated with a simple fit of the P-branch lines. Spectra yielding a temperature outside a range between 120 K and 250 K, and therefore clearly exceeding the range normally found near the subtropical mesopause (Leblanc et al., 1998), were not used. Such temperatures would indicate exceptional atmospheric conditions that may result in unreliable retrievals of the Q-branch coefficients.

The result is a spectrum of the OH airglow with only a slowly changing background. This background consists of remnants of the signal-dependent read-out mechanisms. Since it is signal dependent, it is not part of the dark image. To assess this background, we identified areas between the individual OH lines and assumed any signal here to be due to the background. A polynomial fit of fourth order was made to only these areas free from OH emission to estimate the contribution of the background under the emission lines in that branch. This background was then subtracted to construct a background-free spectrum.

Figure 1 a) shows an example of this background subtraction for the P-branch of the (3,1) transition. The total spectrum is shown as the solid black line. The areas between the lines that are free of OH emission are marked with blue shading, and the fit through these areas is presented as a red, dashed line. Figure 1 b) then shows the spectrum with the background subtracted. This background subtraction method is used for each of the bands examined. To check that all wavelength dependent calibration effects are accounted for, ratios of the intensities of P- and R-branch lines from the same upper state were compared with the ratio of their corresponding Einstein coefficients from the HITRAN database. This confirmed that no wavelength-dependent calibration issues were left in the spectra.

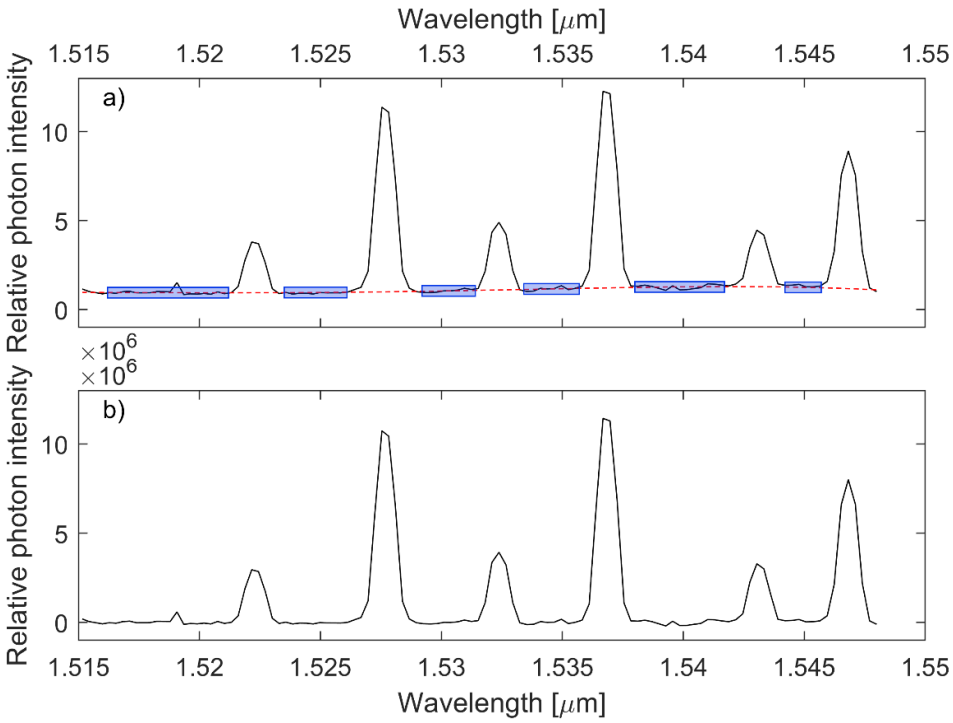

Figure 1: Example of the background fit and subtraction on the P-branch of the (3,1) transition. a): Fit of the background. The clean areas between the lines are marked in blue and the fit of a fourth order polynomial to these areas is shown as a red and dashed line. b): The same spectrum with the background subtracted.

Direct line ratio method

The intensity of each rotational line from a give upper vibrational level, *v'*, is given by:

$$I_{v',v'',J',J''} = N_{v'} 2(2J'+1) e^{E_{v',J'}/kT} A_{v',v'',J',J''} \tag{2}$$

Here, $N_{v'}$ is the relative population of the upper-level *v'*, *T* is the rotational temperature, and *A* is the Einstein coefficient in question. The energy of the upper state $E_{v',J'}$ is taken from the HITRAN database and *k* is the Boltzmann constant. In a given vibrational transition, the ratio of two lines from the same upper rotational level, but with different lower rotational levels, *J''*, then collapses to the ratio of the two Einstein coefficients:

$$\frac{I_{v',v'',J',J_1''}}{I_{v',v'',J',J_2''}} = \frac{A_{v',v'',J',J_1''}}{A_{v',v'',J',J_2''}} \tag{3}$$

For example, given the intensities of the $Q_1(1)$ and $P_1(2)$ lines, which originate in the same upper level, one can calculate the ratio of the transition probabilities in terms of the observed intensities as:

$$\frac{A_{P_1(2)}}{A_{Q_1(1)}} = \frac{I_{P_1(2)}}{I_{Q_1(1)}}. \tag{4}$$

This is the method used in French et al. (2000). In this manner, one can calculate the Einstein coefficients of the Q-branch lines relative to those in the P-branch, which do not suffer from *L*-uncoupling (Pendleton et al., 2002). For transitions, where the P-branch is not available, for example the (6,4) transition, the R-branch can be used. However, since the R-branch does not have a line from the lowest upper-state rotational level, the $Q_1(1)$ line Einstein coefficient cannot be calculated this way. Since the R-branch lines are less intense than the P-branch lines, the (6,4) transition coefficients typically have larger uncertainties.

To obtain the intensities of all lines, Gaussian functions that characterise the instrumental line-shape (Franzen et al., 2017) are centred at the HITRAN positions of the rotational lines and are fitted to the spectrum using a least-squares method. In the case of overlaps between several lines, all lines were fitted at the same time. Figure 2 shows an example of such an overlap in the Q-branch of the (3,1) transition. The lines of the Q_1-subbranch (red) and the Q_2-subbranch (blue) overlap in parts. Tests with synthetic data showed that the overlapping lines are separated enough to reliably fit both lines independently and to retrieve the correct intensities from both.

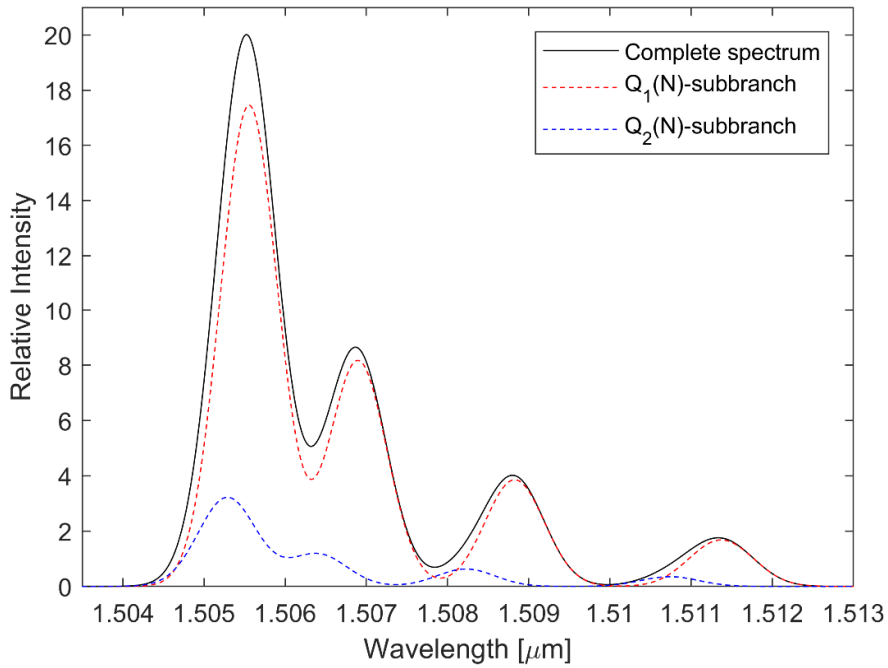

Figure 2: Example of the decomposition of the Q-branch. All lines are synthetic data. Black shows the total spectrum of the Q-branch of the (3,1) transition with a typical temperature of 200 K and line widths for the instrument. The dashed red line shows the contribution from the Q_1(N) lines. The dashed blue line shows the contribution from the Q_2(N) sub-branch.

Whole spectral fit method

In addition, we utilised a second method to measure the Einstein coefficients, where no corresponding line in the R- or P-branch is available, for example in cases where they lie outside the optical filter range. The technique is to obtain a relative population of the upper *v'* vibrational quantum level and the rotational temperature from the P-branch of each transition according to equation (2). Since the P-branch transition probabilities have been shown to be reliable (French et al., 2000), we can use HITRAN Einstein coefficients to fit the P-branch relative population and temperature for each upper vibrational level.

The Einstein transition probabilities are then used as free parameters to fit the Q-branch lines to the same population and rotational temperature. The result will then be Q-branch

transition probabilities relative to the P-branch coefficients tabulated in HITRAN. For cases where several lines overlapped, as seen in Figure 2, the Einstein coefficients for all these overlapping lines were used as free fitting parameters and so this method also yields Einstein coefficients for the Q_2-subbranch lines. These coefficients were found to correspond with the Einstein coefficients tabulated in HITRAN within one or two standard deviations but with a relatively large standard deviation compared to their absolute value (>10%) These values for the Q_2-subbranch are therefore not discussed further in this paper.

4 RESULTS AND DISCUSSION

The two methods described above have been used to measure the Einstein coefficients. The direct line ratio method yielded transition probabilities for most of the Q_1-branch lines, which are shown in Table 1 as the upper value in each cell. The cases, where no Einstein coefficient could be calculated, are marked as (-). The whole spectral fit resulted in transition probabilities of the first four Q_1- branch lines for all seven Meinel transitions. This method can therefore be used to calculate Einstein coefficients for the missing values. The results for this method are shown in Table 1 (lower value in each cell). All numbers are Einstein spontaneous emission transition probabilities and have the units of s^{-1}. The respective values from the HITRAN (HIT) database are shown for comparison.

Figure 3 compares the measured Einstein coefficients derived from both methods, where available. The ratios of the Einstein coefficients measured here to the values listed in HITRAN are presented. The dashed line at the value one is included for clarity. The seven transitions measured in this paper are separated in the vertical direction. The blue crosses are the results from the whole-spectral fit, while the red circles are the results from the direct line ratios. All error bars shown represent twice the standard error of the measurements. The horizontal shift between the blue crosses and red circles for the same upper vibrational level *J'* are merely for visibility.

Line:	$Q_1(1)$		$Q_1(2)$		$Q_1(3)$		$Q_1(4)$	
Transition	Measured	HIT	Measured	HIT	Measured	HIT	Measured	HIT
(3,1)	13.80±0.06 13.57±0.06	15.70	5.68±0.07 5.83±0.05	6.39	2.30±0.05 2.45±0.06	3.35	1.32±0.18 1.27±0.07	2.01
(4,2)	25.20±0.13 24.83±0.09	27.71	10.65±0.09 10.71±0.05	11.30	5.59±0.13 5.54±0.07	5.94	3.71±0.15 3.80±0.13	3.57
(5,3)	34.66±0.15 34.44±0.20	40.29	14.89±0.18 15.20±0.10	16.46	8.30±0.24 8.51±0.06	8.67	4.36±0.10 4.41±0.06	5.22
(6,4)	(-) 46.35±1.32	51.88	19.58±0.59 19.63±0.59	21.25	7.45±0.51 7.58±0.49	11.21	4.03±0.79 4.01±0.75	6.75
(7,4)	14.10±0.05 13.71±0.07	15.72	6.16±0.13 6.34±0.15	6.46	2.97±0.14 2.98±0.12	3.42	1.19±0.16 1.25±0.19	2.07
(8,5)	20.00±0.36 19.11±0.27	22.78	7.89±0.20 8.28±0.16	9.38	(-) 4.16±0.16	4.98	(-) 1.09±0.07	3.02
(9,7)	56.93±0.47 56.03±0.36	63.16	27.12±0.26 27.35±0.30	26.01	11.72±0.18 11.55±0.13	13.75	4.55±0.24 4.83±0.25	8.30

Table 1: Einstein transition probabilities for the spontaneous emission of the first four Q-branch lines of the vibrational transitions. Each value is given for the direct line ratio method (upper value) and the whole spectral fit method (lower value). Values which could not be calculated are marked as (-). The measured values are given with their respective error of one standard deviation and the HITRAN (HIT) value for comparison. All numbers are in units of s^{-1}.

Figure 3 shows that whenever both methods for Einstein coefficient retrieval were possible, the resulting values agree within their errors. We are therefore confident in the whole spectral fit method as much as in the direct line ratio method (as employed by French et al. (2000)). The direct line ratio method could not retrieve Einstein coefficients for the Q(1) line of the (6,4) transition, because the whole P-branch is outside the filter range. The R-branch was used here instead. In addition the (8,5) transition lacks the Q(3) and Q(4) line due to the filter cut off. The values presented above are the ones retrieved using the direct line ratio with the lowest two P-branch lines.

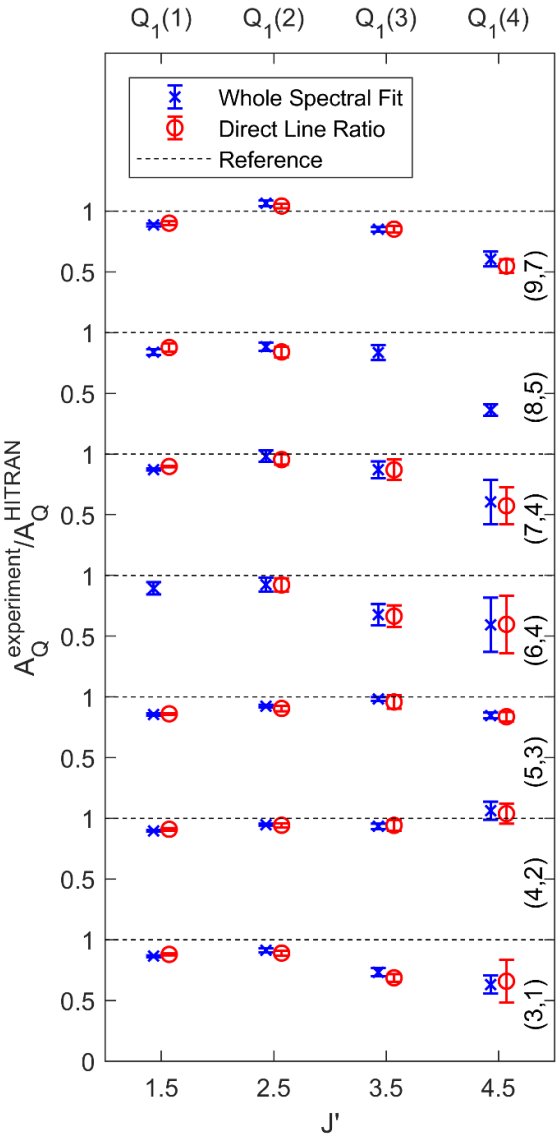

Figure 3: Einstein coefficients measured, relative to those reported in the HITRAN database. The first four Q-branch lines of the seven Meinel transitions are shown. The red circles are those determined using the direct line ratio method while the blue crosses represent those determined from the whole-spectral fit method. The errorbars represent twice the standard error of the fit.

Most of the values shown in Figure 3 show smaller transition probabilities than listed in HITRAN. This is especially the case for the (3,1), (6,4), (7,4), (8,5), and (9,7) transitions

which show smaller values than HITRAN with tendencies to even smaller values with higher *J'*. Most of these values are significantly different from the HITRAN values by at least twice the standard error. The two other transitions, the (4,2) and the (5,3) seem to lie closer to the HITRAN values than the others.

To test the validity of the method employed here, we created synthetic data using tabulated Einstein coefficients and subjected them to the same retrieval process. The coefficients were varied between 50% and 150% of the HITRAN values, and artificial Gaussian noise up to double the noise observed in the data was added. We found that the Einstein coefficients determined from this synthetic data were in good agreement with the chosen values in the synthetic dataset. Also, addition of a simple linear or quadratic background did not skew the calculated values significantly in any direction.

We also investigated whether the change in Einstein coefficients could be caused by some external mechanisms, rather than an internal quantum mechanical coupling as discussed by Pendleton et al. (2002). We therefore undertook an extensive correlation study with the available data. We calculated correlation coefficients between the measured Einstein coefficients and: the temperature of the MLT region; the air mass through which the OH was observed; the integration time of the observation; the day of the year of the observation and the time in the night of the observation. None of these parameters showed any significant correlation with the Einstein coefficients. This absence of correlation supports the assertion that the Einstein coefficients presented here differ from the theoretical values.

French et al. (2000) studied the ratio of the line intensities from the Q- and the P-branches of the (6,2) transition. This transition is beyond the spectroscopic range of the NOTCam instrument, but data on the (6,4) transition are available. These two transitions are especially comparable since they originate from the same vibrational upper level. The ratio of the Einstein coefficients derived from the P and Q branch lines in each of the two transition are shown in Figure 4 for comparison with their corresponding HITRAN values. The measurements from French et al. (2000) and the HITRAN values for the (6,2) transition are shown in black. Similarly, the measurements from this study and their comparative values from HITRAN from the (6,4) transition are shown in red. For all lines,

the ratios between the P-branch Einstein coefficients and the Q-branch Einstein coefficients are shown, as in Pendleton et al. (2002). While the absolute values of the two transitions are different, the relative difference between the measurements and the HITRAN values of the two transitions is similar. We therefore conclude that the *L*-uncoupling invoked to explain the difference in Einstein coefficients for the (6,2) transition may also be the cause of the differences in the (6,4) transition reported here.

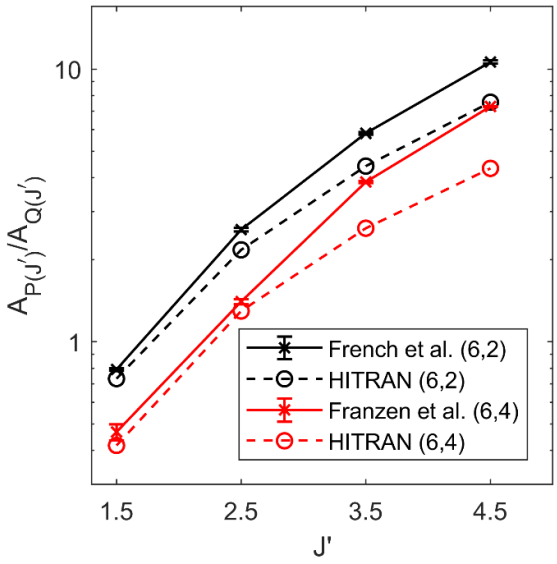

Figure 4: In black: ratio of the Einstein coefficients derived from the P-and Q-branch lines French et al. (2000) of the (6,2) transition (crosses) and the HITRAN values for the (6,2) transition (circles, dashed). In red: the same measurements from this study of the (6,4) transition (crosses) and from HITRAN for the same transition (circles, dashed). While the absolute values change between the two different transitions, the difference between HITRAN and the measurements is similar for both studies.

5 CONCLUSION

By evaluating a total of 17.8 hours of astronomical background NIR spectroscopic observations of the OH airglow obtained by the Nordic Optical Telescope NOTCam instrument, we have calculated Einstein coefficients of the Q_1-branches of seven Meinel transitions (3,1), (4,2), (5,3), (6,4), (7,4), (8,5) and (9,7). The routines used to extract the coefficients were extensively tested and verified with synthetic data. Most of the measured Einstein coefficients are significantly lower than the theoretical values used for

example in the HITRAN database. The J' = 1.5 lines are on average by 13±2 % lower than the HITRAN values, whereas the measured values for J' = 2.5 lines were generally closer to the HITRAN values than for other measured J'. The J' = 4.5 deviations were the most variable with the (8,5) transition 64 % lower than the HITRAN value, while the measured value from the (4,2) transition was found to agree with the HITRAN value to within observational errors.

Many of the Einstein coefficients differ from the theoretical values by at least twice the standard error of the measurements. The measured Einstein coefficients are found to be inherently different from the theoretical values, and are not influenced by observation conditions since they were found to show no correlation with any observation parameters. Hence, we present this updated set of measured Q-branch Einstein coefficients.

ACKNOWLEDGEMENTS

This work was based on observations made with the Nordic Optical Telescope, operated by the Nordic Optical Telescope Scientific Association at the Observatorio del Roque de los Muchachos, La Palma, Spain of the Instituto de Astrofisica de Canarias. It was supported by the Research Council of Norway/CoE under contract 223252/F50.

Archive data from the NOTCam can be accessed via http://www.not.iac.es/observing/forms/fitsarchive/ (Nordic Optical Telescope, 2019).

BIBLIOGRAPHY

Baker, D. J., & Stair, J. A. T. (1988). Rocket Measurements of the Altitude Distributions of the Hydroxyl Airglow. *Phys Scripta, 37*(4), 611-622.

Bittner, M., Offermann, D., & Graef, H. H. (2000). Mesopause Temperature Variability above a Midlatitude Station in Europe. *Journal of Geophysical Research: Atmospheres, 105*(D2), 2045-2058. doi:doi:10.1029/1999JD900307

Cosby, P. C., & Slanger, T. G. (2007). OH Spectroscopy and Chemistry Investigated with Astronomical Sky Spectra. *Canadian Journal of Physics, 85*(2), 77-99. doi:10.1139/p06-088

Djupvik, A. A., & Andersen, J. (2010). The Nordic Optical Telescope. In M. J. Diego, J. L. Goicoechea, I. J. González-Serrano, & J. Gorgas (Eds.), *Highlights of Spanish Astrophysics V* (pp. 211-218): Springer Berlin Heidelberg.

Espy, P. J., & Stegman, J. (2002). Trends and Variability of Mesospheric Temperature at High-Latitudes. *Phys Chem Earth, 27*(6-8), 543-553.

Franzen, C., Espy, P. J., Hibbins, R. E., & Djupvik, A. A. (2018). Observation of Quasiperiodic Structures in the Hydroxyl Airglow on Scales Below 100 M. *Journal of Geophysical Research: Atmospheres, 123*(19), 10,935-910,942. doi:10.1029/2018JD028732

Franzen, C., Hibbins, R. E., Espy, P. J., & Djupvik, A. A. (2017). Optimizing Hydroxyl Airglow Retrievals from Long-Slit Astronomical Spectroscopic Observations. *Atmospheric Measurement Techniques, 10*(8), 3093-3101. doi:10.5194/amt-10-3093-2017

French, W. J. R., Burns, G. B., Finlayson, K., Greet, P. A., Lowe, R. P., & Williams, P. F. B. (2000). Hydroxyl (6/2) Airglow Emission Intensity Ratios for Rotational Temperature Determination. *Annales Geophysicae, 18*(10), 1293-1303. doi:10.1007/s00585-000-1293-2

Innis, J. L., Phillips, F. A., Burns, G. B., Greet, P. A., French, W. J. R., & Dyson, P. L. (2001). Mesospheric Temperatures from Observations of the Hydroxyl (6–2) Emission above Davis, Antarctica: A Comparison of Rotational and Doppler Measurements. *Ann. Geophys., 19*(3), 359-365. doi:10.5194/angeo-19-359-2001

Langhoff, S. R., Werner, H. J., & Rosmus, P. (1986). Theoretical Transition Probabilities for the OH Meinel System. *Journal of Molecular Spectroscopy, 118*(2), 507-529. doi:https://doi.org/10.1016/0022-2852(86)90186-4

Leblanc, T., Stuart McDermid, I., Keckhut, P., Hauchecorne, A., She, C.-Y., & Krueger, D. (1998). *Temperature Climatology of the Middle Atmosphere from Long-Term Lidar Measurements at Middle and Low Latitudes* (Vol. 1031).

Mies, F. H. (1974). Calculated Vibrational Transition Probabilities of OH(X2π). *Journal of Molecular Spectroscopy, 53*(2), 150-188. doi:https://doi.org/10.1016/0022-2852(74)90125-8

Noll, S., Kausch, W., Kimeswenger, S., Unterguggenberger, S., & Jones, A. M. (2015). OH Populations and Temperatures from Simultaneous Spectroscopic Observations of 25 Bands. *Atmos. Chem. Phys., 15*(7), 3647-3669.

Pendleton, W. R., Espy, P. J., Baker, D., Steed, A., Fetrow, M., & Henriksen, K. (1989). Observation of OH Meinel (7,4) P(N″=13) Transitions in the Night Airglow. *Journal of Geophysical Research: Space Physics, 94*(A1), 505-510. doi:doi:10.1029/JA094iA01p00505

Pendleton, W. R., & Taylor, M. J. (2002). The Impact of L-Uncoupling on Einstein Coefficients for the OH Meinel (6,2) Band: Implications for Q-Branch Rotational Temperatures. *Journal of Atmospheric and Solar-Terrestrial Physics, 64*(8), 971-983. doi:https://doi.org/10.1016/S1364-6826(02)00051-2

Pickett, H. M., Poynter, R. L., Cohen, E. A., Delitsky, M. L., Pearson, J. C., & Müller, H. S. P. (1998). Submillimeter, Millimeter, and Microwave Spectral Line Catalog. *Journal of Quantitative Spectroscopy and Radiative Transfer, 60*(5), 883-890. doi:https://doi.org/10.1016/S0022-4073(98)00091-0

Rothman, L. S., Gordon, I. E., Babikov, Y., Barbe, A., Chris Benner, D., Bernath, P. F., . . . Wagner, G. (2013). The Hitran2012 Molecular Spectroscopic Database. *J Quant Spectrosc Ra, 130*, 4-50.

Sivjee, G. G. (1992). Airglow Hydroxyl Emissions. *Planetary and Space Science, 40*(2-3), 235 - 242.

Taylor, M. J., Pendleton Jr, W. R., Pautet, P.-D., Zhao, Y., Olsen, C., Babu, H. K. S., . . . Takahashi, H. (2007). Recent Progress in Mesospheric Gravity Wave Studies Using Nightglow Imaging System. *Revista Brasileira de Geofísica, 25*, 49-58.

Turnbull, D. N., & Lowe, R. P. (1989). New Hydroxyl Transition Probabilities and Their Importance in Airglow Studies. *Planetary and Space Science, 37*(6), 723-738. doi:https://doi.org/10.1016/0032-0633(89)90042-1

Wiens, R. H., Moise, A., Brown, S., Sargoytchev, S., Peterson, R. N., Shepherd, G. G., . . . Rodrigo, R. (1997). Sati: A Spectral Airglow Temperature Imager. *Advances in Space Research, 19*(4), 677-680. doi:https://doi.org/10.1016/S0273-1177(97)00162-2

Wüst, S., Bittner, M., Yee, J. H., Mlynczak, M. G., & Russell Iii, J. M. (2017). Variability of the Brunt–Väisälä Frequency at the OH* Layer Height. *Atmospheric Measurement Techniques, 10*(12), 4895-4903. doi:10.5194/amt-10-4895-2017